

Quantitative Analysis of Perivascular Antibody Distribution in Solid Tumors

By John J. Rhoden

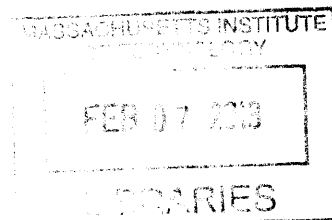
B.S. Chemical and Biomolecular Engineering
North Carolina State University, 2007

Submitted to the Department of Chemical Engineering in Partial Fulfillment of the
Requirements for the Degree of

DOCTOR OF PHILOSOPHY
In Chemical Engineering

At the

Massachusetts Institute of Technology
September 2012



© 2012 Massachusetts Institute of Technology
All rights reserved

Signature of author _____

John J. Rhoden
Department of Chemical Engineering
September 2012

Certified by _____

K. Dane Wittrup
C.P. Dubbs Professor of Chemical Engineering and Biological Engineering
Thesis Advisor

Accepted by _____

Patrick S. Doyle
Professor of Chemical Engineering
Chairman, Committee for Graduate Students

Quantitative Analysis of Perivascular Antibody Distribution in Solid Tumors

By John Joseph Rhoden

Submitted to the Department of Chemical Engineering on September 4, 2012 in Partial Fulfillment of the Requirements for the Degree of Doctor of Philosophy in Chemical Engineering

ABSTRACT

Monoclonal antibodies and proteins derived from them are an emerging class of anticancer therapeutics that have shown efficacy in a range of blood and solid tumors. Antibodies targeting solid tumors face considerable transport barriers *in vivo*, including blood clearance, extravasation, diffusion within the tumor interstitium, binding to antigen, endocytosis, and degradation. The unique pathology of the blood supply to solid tumors only serves to exacerbate these problems.

A consequence of poor delivery of antibodies to solid tumors is a characteristic perivascular distribution of antibodies around tumor blood vessels. Often, antibodies bind only cells within a few cell layers of blood vessels, leaving large areas of tumor cells farther from perfused vessels completely untargeted. This phenomenon has been observed in multiple studies involving different antibodies, antigens, and tumor types, both in animal models and in clinical settings. In this thesis, the perivascular localization of antibodies is explored as a function of quantitative parameters of the antibody and associated antigen. A novel experimental system to quantitatively determine bound antibody levels, antigen levels, and blood vessel localization on a microscopic scale throughout entire tumor cross sections has been developed. This system has been used to quantitatively measure antibody and antigen distribution in tumor tissue under a variety of conditions. Effects of varying antibody dose, antibody affinity, and tumor type and site have been explored and quantitated using this model.

To guide experimental design, we have developed a simplified mathematical model of the tumor vasculature. This model offers insights into the effects of antigen and antibody parameters, including dose, affinity, antigen density, and endocytosis rates, which are measurable *in vivo* and affect antibody penetration into tumor tissue. A simple scaling analysis further allows the quantitative determination of the minimum antibody dose required to saturate a tumor given the antigen turnover rate and density. Together, the mathematical model and quantitative experimental analysis allow conclusions to be made regarding antibody design and antigen selection for improved tumor penetration of therapeutic antibodies.

Thesis Supervisor: Dr. K. Dane Wittrup

Title: C.P. Dubbs Professor of Chemical Engineering and Biological Engineering

Acknowledgements

This was made possible by the assistance and contributions of many others. Most notably, my advisor, Dane Wittrup, has been an extraordinary mentor and has helped to guide this work through many twists and turns. His technical insights and contributions were important, and his broader knowledge about science and personal and career development even more so. Dane has a great ability to guide his students, while retaining the patience to allow the students to develop and follow their own interests and become capable independent researchers.

My other committee members, Sangeeta Bhatia and Bill Deen, have provided valuable comments and have shown a great deal of patience and support as my project developed over time. Their criticisms, comments, and feedback helped to focus my efforts and pointed out topics that could be well addressed by my work. I appreciate that both of them took the time out of busy schedules to provide guidance regarding my thesis project.

The Wittrup lab has been a great place to grow and develop as a scientist. My predecessors in the lab laid the foundation for my graduate work, and virtually everyone I have come into contact with in the lab has contributed to this work. Greg Thurber, Ben Hackel, Steve Sazinsky, Kelly Orcutt, Eileen Higham, Margie Ackerman, Jamie Spangler, David Liu, Chris Pirie, Annie Gai, and Jordi Mata-Fink helped me to get started in the lab and laid the foundations for my work. More recent students Xiaosai Yao, Tiffany Chen, Nicole Yang, Cary Opel, Pete Bak, Byron Kwan, Michael Santos, Alice Tzeng, Jim van Deventer, Alessandro Angelini, Katie Maass, and Eric Zhu shaped the culture of the lab and were all a pleasure to discuss science and collaborate with.

I have had the opportunity during my time in the Wittrup lab to work with several extraordinary undergraduate students. Maryelise Cieslewicz, Yap Jun-Liang, and Lauren Garcia-Spite were all a pleasure to work with, made substantial contributions scientifically, and taught me valuable lessons about mentoring and leadership. I wish to single out Lauren, who worked with me for over two years, as a hard worker who not only made my life as a researcher much easier, but also through her conversation and sense of humor made my time in the lab much more enjoyable.

Lastly, I would like to thank my friends and family for their support during my time in graduate school. Their perspective and guidance were invaluable during the sometimes long and isolating process of graduate studies. Most importantly, my wife Julia has been alongside me since the beginning and has been supportive of strange work hours and the ups and downs of research. My parents have always supported my ambitions and it is because of their work and sacrifices throughout my life that I am in this position today.

**Dedicated to my grandparents Tom and Betty Gann
who through their words and actions have taught me invaluable lessons
about the things that are truly important in life**

Contents

1. INTRODUCTION	7
1.1 Background.....	7
1.2 Antibody treatment of cancer.....	8
1.3 In vivo tumor targeting	10
1.4 Tunable targeting parameters	16
1.5 Thesis overview	20
1.6 References.....	21
2. ANTIBODY DOSE VS. TUMOR PENETRATION.....	28
2.1 Introduction.....	28
2.2 Materials and methods	29
2.3 Mathematical modeling.....	31
2.4 Results	33
2.5 Discussion.....	38
2.6 References.....	44
3. ANTIBODY AFFINITY VS. PENETRATION AND ACCUMULATION	47
3.1 Introduction.....	47
3.2 Materials and methods	49
3.3 Results	52
3.4 Discussion.....	60
3.5 References.....	65
4. ANTIBODY DOSING STRATEGIES TO IMPROVE TUMOR PENETRATION	67
4.1 Introduction.....	67
4.2 Materials and methods	69
4.3 Results	72
4.4 Discussion.....	82
4.5 References.....	86
5. ORTHOTOPIC AND ECTOPIC XENOGRAFT TUMORS	88
5.1 Introduction.....	88
5.2 Materials and methods	90
5.3 Results	92
5.4 Discussion	99
5.5 References.....	103

6. DEVELOPMENT OF AN AUTOCHTHONOUS CEA-EXPRESSING MOUSE MODEL.....	105
6.1 Introduction.....	105
6.2 Materials and methods	109
6.3 Results	114
6.4 Discussion.....	124
6.5 References.....	129
Appendix A: Tumor penetration model and parameters	133
Appendix B: DNA sequence of lentiviral vectors and protein constructs	137

1. INTRODUCTION

1.1 Background

Cancer encompasses a diverse set of diseases which are characterized by the unconstrained growth of cells within the host's body¹. Worldwide, cancer is a leading cause of mortality, killing in excess of 7.6 million people each year². In the United States, cancer is diagnosed in over 1.6 million patients each year, killing nearly 600,000 annually or approximately one in four deaths^{3,4}. Despite decades of research and significant progress understanding the origins and pathology of cancer, it remains a difficult disease to treat, in large part because the cancer cells arise from the tissue of the host.

Traditional treatments for cancer make up the bulk of modern clinical treatments, and can be divided into three categories: surgery, radiation, and chemotherapy. Surgery involves the invasive excision of the tumor, and when successful is often curative. However, it requires that the location of the tumor be known and accessible to surgical intervention. Surgery is also ineffective against metastatic disease or tumors too small to be detected by current medical imaging techniques⁵. Likewise, radiation is often able to shrink or even ablate tumors, but requires that the location of the tumor be accurately known. Radiation also causes damage to healthy tissue in and nearby the path of the radiation. In contrast, chemotherapeutics are cytotoxic drugs which are typically administered systemically and target rapidly dividing cells, of which tumor cells are only a subtype. As a result, chemotherapy may be effective against tumors of varying sizes and locations in the body, including micrometastases and other tumors too small to be detected. However, the drugs exert a nonspecific effect and affect all rapidly dividing cells of the body, causing substantial side effects and damage to healthy tissue.

New cancer treatments that retain the benefit of systemic administration while improving tumor-specific targeting are under development and some have recently advanced to clinical use. These treatments are generally targeted to molecules which are selectively expressed, upregulated, or mutated specifically in cancer cells. This thesis is focused on a particular class of molecules, antibodies, which target and bind cancer cell antigens. Antibodies can exert

antitumor effects in a number of ways by binding antigen, including by altering receptor function (e.g. ligand blocking or receptor downregulation), activating the host immune system, or by selectively delivering a cytotoxic drug directly and selectively to the tumors cells⁶. They have been successfully developed as drugs in the context of many different cancer types, from blood cancers to solid tumors of several different organs, and represent an important and growing field of research and drug development.

1.2 Antibody treatment of cancer

Antibodies are an important part of the adaptive immune system. They are able to recognize an enormous array of foreign pathogens with a high degree of specificity. The most prevalent subtype of antibody, immunoglobulin G (IgG), is the focus of most research into therapeutic antibodies and will be the focus of this thesis. It is a 150 kDa protein that consists of two identical binding domains joined to a constant domain that has functions including recruitment of immune responses and extension of antibody serum half life⁷⁻⁹.

Antibodies can be engineered to attain or enhance certain properties, such as specificity to a certain target antigen, binding affinity to that antigen, and to some extent recruitment of immune effector functions and serum stability and persistence^{8,10-12}. These properties have made them popular scaffolds for drug discovery and development, and there are currently twelve antibodies or antibody-drug conjugates which are approved for clinical use in the United States or Europe.⁶ There are dozens of antibodies which are in various stages of clinical trials for oncology indications, and hundreds more for other diseases¹³.

Another appeal of antibodies as therapeutics is the diverse mechanisms by which they can exert anti-tumor effects. Antibodies can engage the immune system through activation of complement, through antibody directed cellular cytotoxicity (ADCC), by blocking access of ligand to cell surface receptors, or by otherwise modulating cellular signaling^{6,14}. By virtue of their highly specific targeting, antibodies have also found use as carriers for cytotoxic agents to deliver them specifically to tumors. These agents include toxins, which are conjugated to the

antibody and delivered intracellularly to targeted cells, as well as radionuclides which emit damaging radiation to cells in the vicinity of targeted tissue¹⁵⁻¹⁸. Finally, a significant focus of research and preclinical drug development lies in using nanoparticles as anticancer agents, and these are often targeted to tumors by conjugating antibodies or antibody fragments to the nanoparticles^{19,20}.

Unlike traditional methods of cancer treatment, antibodies can be administered systemically and be highly targeted to tumor cells. Because of this unique combination of traits, they were called “magic bullets” by Paul Ehrlich nearly a century ago²¹. However, realization of the potential of antibodies as therapeutics has been slow, and recently some of the barriers to the realization of the potential of antibodies as cancer therapeutics have become apparent.

At approximately 150 kDa in size, antibodies are orders of magnitude larger than most chemotherapeutics (Figure 1.1). Because of their size and complexity, antibodies can be “engineered” for desirable properties such as stability, binding affinity and specificity, and immune effector functions^{8,10,12}. However, their large size also has deleterious effects on antibody diffusivity and vascular permeability, potentially limiting their access to extravascular targets²²⁻²⁶. There is some empirical evidence of this in the form of the FDA-approved antibody therapeutics in the clinic. In 2009, 5 of the 9 approved anticancer antibodies were against blood cancers, despite these making up just 10-15% of all cancer diagnoses. This observation is significant because blood cancers are much easier targets for intravenously delivered therapeutics such as antibodies than are solid tumors. Active areas of research in antibody engineering as well as antigen selection and antibody pharmacokinetics are seeking methods to improve the delivery of antibodies to solid tumors.

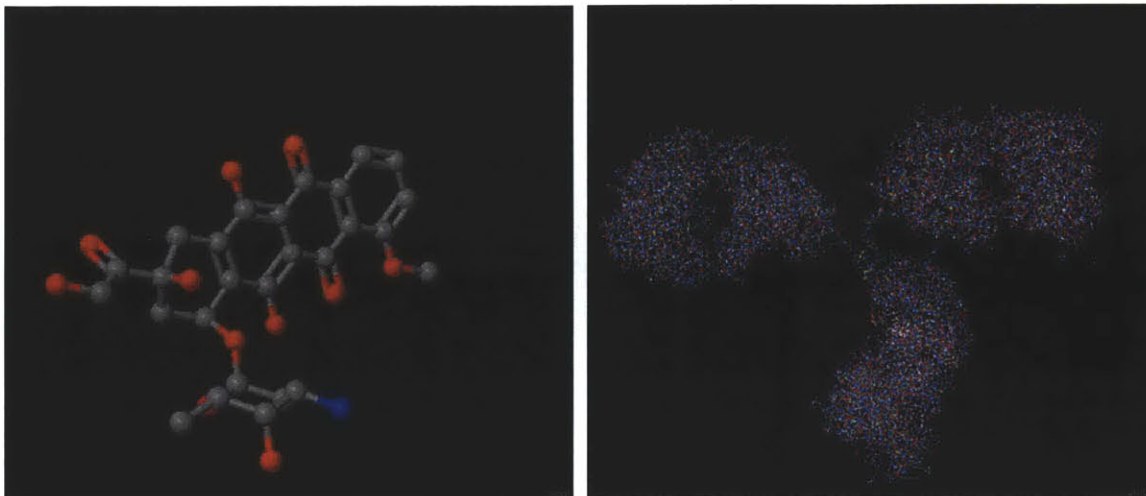


Figure 1.1. Comparison of size of a representative small molecule chemotherapeutic (doxorubicin, at left) with monoclonal antibodies (murine IgG2a, at right)²⁷. For comparison, the molecular mass of doxorubicin is about 544 Da, whereas antibodies measure approximately 150,000 Da. This difference in size and complexity creates dramatically different properties between the two classes of molecules. These differences in turn dictate behavior of these molecules *in vivo*, including their administration, plasma clearance behavior and rate, vascular permeability, diffusivity, binding properties, and routes and rates of metabolism.

1.3 In vivo tumor targeting

All antibody therapeutics which are currently in clinical use are administered intravenously, giving them access to the systemic circulation and also exposing them to numerous routes of clearance and barriers to efficient delivery to the tumor tissue. Often, the result of administration of antibody therapeutics is that only a small fraction, generally only a fraction of a percent of the injected dose per gram of tumor tissue, reaches the tumor tissue²⁸⁻³⁰. There are many factors which contribute to the poor delivery of antibodies to tumor tissue, including properties of the antibody itself as well as the pathological nature of blood flow in the tumor space.

The delivery of macromolecules to solid tumors can be separated into two distinct parts based upon length scales. First and best described in the literature is the bulk accumulation of the drug administered. From this perspective, the greatest accumulation of the therapeutic in the organ of interest, in this case the tumor, and the lowest accumulation in other organs is

typically desired. Bulk accumulation can be measured preclinically with a high degree of accuracy using necropsy to obtain a quantitative biodistribution at a certain time point^{31,32}. It can also be measured preclinically as well as in the clinic using noninvasive imaging technologies such as microCT, magnetic resonance imaging (MRI), positron emission tomography (PET), and in some cases fluorescence^{5,33-38}. These methods can be useful for exploring the time course of tissue accumulation.

Bulk accumulation is also amenable to pharmacokinetic modeling. Using *in vitro* measurements of molecular properties, such as stability, size, and binding affinity, and *in vivo* measurements of parameters such as plasma clearance rate and biodistribution, the distribution and in some cases efficacy of therapeutics can be mathematically modeled to give predictions that can be applied to preclinical studies and even scaled to clinical studies^{28,39-41}. Many of these models are compartmental in nature, and treat organs or organ systems as compartments between which drugs can be exchanged at rates which are typically fit to experimental data. As a consequence, both pharmacokinetic models and experimental analyses such as *in vivo* imaging and necropsy are limited in that they hold that organs, including the tumor, can be assumed to be well mixed compartments. While they may be useful for measuring and predicting the accumulation of antibodies in tissues, they fail to consider how the antibodies distribute within the tissue and simply assume that antibodies distribute in a homogeneous fashion.

However, the assumption that antibodies distribute homogeneously within tumor tissue has been shown to be false. When tumors are examined at a microscopic scale, it becomes clear that antibodies and other binding macromolecules such as targeted nanoparticles distribute in a perivascular fashion^{22,42-47}. Tumor cells which are within a few cell layers of perfused vessels are often well targeted, but viable tumor cells which are located slightly farther away from these vessels are often poorly targeted or completely untargeted (Figure 1.2). This phenomenon has been observed preclinically in a range of cases, including different tumor cell lines, antigens, and antibodies. Perivascular localization of antibody therapeutics has also been observed in the case of some antibodies which are currently FDA approved, including Herceptin, Cetuximab, and Panitumumab^{43,48,49}. There is also evidence that poor tumor penetration is observed in the clinic, although the evidence is less compelling⁵⁰. For

therapeutics which must reach cells to be effective, such as those which block ligand binding or must be internalized to be effective, these untargeted regions represent a real problem. For other therapeutic modalities which can act from a distance, such as radioimmunotherapeutics or immunotherapies which recruit immune cells to the site of disease, the problem of poor tissue penetration may not be so significant.

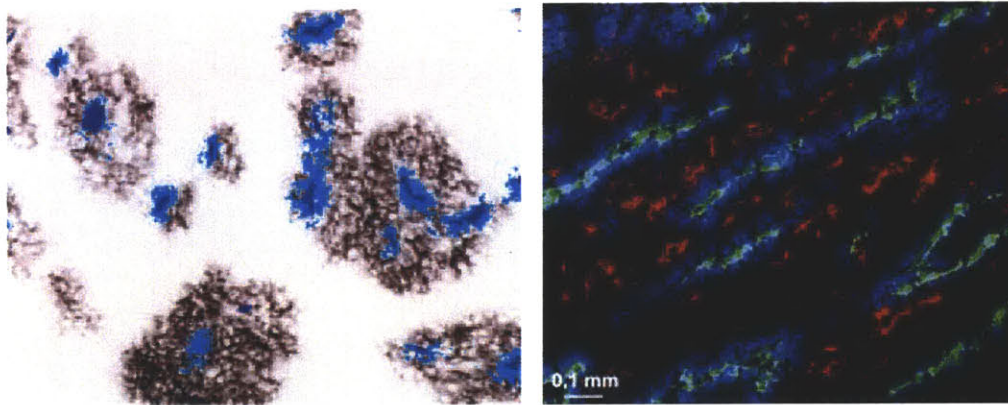


Figure 1.2. Examples of poor penetration of antibodies into solid tumors. At left, trastuzumab (Herceptin), clinically approved monoclonal antibody, penetrates poorly into a xenograft cancer model⁴⁸. Light blue denotes blood vessels, dark blue represents a perfusion marker, and dark brown represents trastuzumab. At right, an anti-CEA antibody exhibits heterogeneous distribution in a xenograft model of cancer. Green represents blood vessels, blue anti-CEA antibody, and red areas of hypoxia²⁴.

Antibody delivery to and distribution within solid tumors is hindered by a number of factors. Although antibodies typically have extremely long half lives relative to other similarly-sized molecules due to neonatal Fc receptor (FcRn) recycling, they are nonetheless large molecules which are larger than the pores typically found in blood vessels^{51,52}. Tumors, however, possess a pathological network of blood vessels. The process of neoangiogenesis does not occur under normal conditions in adults, but dysregulation in cancer leads to the secretion of growth factors including vascular endothelial growth factor (VEGF), a potent stimulant of neoangiogenesis⁵³. Tumors which grow over a size of approximately one millimeter must recruit a new blood supply to grow further, and begin overexpression of VEGF to recruit a vasculature⁵⁴. The newly formed blood vessels do not form in an orderly manner—instead, they form convoluted, unpredictable networks with many shunts, dead ends, and loops^{25,55–57}. They are also much

more leaky than normal blood vessels, a phenomenon which has substantial implications for drug delivery to solid tumors^{53,58}. The result of the irregular nature of the blood vessels that form in the tumor is that many blood vessels that form do not perform their functions efficiently, and in many cases are nonfunctional. This creates irregular perfusion in the tumor and areas with poor or no delivery of blood⁵⁸⁻⁶⁰.

As a consequence of their enhanced leakiness and larger pore sizes than normal blood vessels, tumor vessels allow fluids and macromolecules to extravasate much more readily than healthy vessels^{61,62}. Most solid tumors do not drain extravasated fluid well because they generally lack a functional lymphatic system^{63,64}. As a result, the interstitial fluid pressure (IFP) in the tumor is typically quite high, and often nearly matches the pressure in the tumor blood vessels^{61,65}. This lack of a substantial pressure gradient diminishes the convective flow of blood and macromolecules in the blood to a level that it can generally be neglected relative to diffusive transport^{22,66-68}. For large molecules, such as antibodies and nanoparticles, which diffuse slowly because of their large sizes, the lack of convective transport substantially impedes the transport of these molecules into the tumor space.

Antibodies which do extravasate and diffuse into the tumor space then face another barrier to efficient, homogeneous distribution in the form of binding to antigen^{46,47,69}. Once bound to cell surface antigen, antibodies are subject to the trafficking of the antigen. Often, antigens and bound antibodies are endocytosed and degraded, or sometimes recycled to the cell surface. Most antibodies for therapeutic applications are chosen or engineered to have a high affinity, often with dissociation half times on the order of hours or more. Since constitutive membrane turnover occurs with a half time of approximately 12 hours, this means that antibodies often bind only one antigen, and that they are endocytosed and degraded at the site of that antigen⁷⁰.

The effects of antigen-mediated antibody catabolism have been well documented experimentally. Using well controlled *in vitro* experiments, the rates of diffusion, binding, endocytosis, and degradation can be compared to determine how each affects tissue penetration^{71,72}. Applying a scaling analysis analogous to the Thiele modulus used in chemical

engineering analyses of chemical kinetics, it is possible to make a quantitative prediction of the distance penetrated into a three dimensional tumor spheroid as a function of antibody and antigen properties. This scaling analysis was shown to be highly predictive of penetration time and distance in this experimental system⁷³. It was extended in other work to allow penetration into spheroids to be predicted by easily measured antibody and antigen parameters:

$$R = \sqrt{\frac{D[\text{Ab}]_{\text{surface}}}{k_e([\text{Ag}]_{\text{tumor}} / \varepsilon)}}$$

Where R is the radius penetrated, D is antibody diffusivity, $[\text{Ab}]_{\text{surface}}$ is the antibody concentration at the spheroid surface (bulk concentration), k_e is the endocytosis rate, $[\text{Ag}]_{\text{tumor}}$ is the antigen concentration in the spheroid, and ε is the void fraction in the spheroid. This simple expression was tested varying $[\text{Ab}]_{\text{surface}}$, changing $[\text{Ag}]_{\text{tumor}}$ through the use of different cell lines, and by altering k_e through changing incubation temperature. In all cases, the quantitative predictions of the scaling analysis were able to capture the fundamental behavior of the process, and were generally quantitatively precise within approximately a factor of two^{72,73}.

These models illustrate the power of mathematical models, even simple scaling analyses, to capture salient features and make quantitative predictions in complex biological systems. The next step in the development of these models is to extend them to the *in vivo* environment, which tends to be more complex, more heterogeneous, and more difficult to study experimentally, particularly in a quantitative fashion. In a tumor, the antibody is delivered by the vasculature, and must extravasate into the tissue from the vascular compartment. It is reasonable to ask whether this extravasation step represents a major barrier to antibody delivery or whether it may be negligible relative to the other barriers, such as plasma clearance and antibody binding and catabolism.

To address this question, previous research has compared the rate of antibody extravasation to the rate of diffusion through the tumor interstitium²³. Mathematically, this rate is analogous to the Biot number in engineering and can be expressed as:

$$\text{Biot} = \frac{\text{Extravasation rate}}{\text{Diffusion rate}} = \frac{2PR_{cap}}{D}$$

Using typical values for a molecule of the size of antibody, permeability ($P = 3 \times 10^{-3} \mu\text{m/s}$), capillary radius ($R_{cap} = 10 \mu\text{m}$), and diffusivity ($D = 14 \mu\text{m}^2/\text{s}$), one finds that Biot is approximately 0.004 for an antibody²³. The Biot number is therefore much less than one, which implies that the diffusion rate is much faster than the extravasation rate. Therefore, extravasation of antibody is a rate limiting process and must be considered in any relevant experimental or modeling system.

A similar analysis was conducted to further examine the potential limiting rates of antibody delivery to solid tumors²³. Two dimensionless parameters were analyzed to determine the limiting rates under conditions typical of antibodies *in vivo*. These parameters were ratios of rates of antibody transport. The first such ratio was termed the clearance modulus and represented mathematically as:

$$\Gamma = \frac{\text{Plasma clearance rate}}{\text{Tumor penetration rate}} = \frac{R^2 ([Ag]/\varepsilon)}{D(AUC_{surf})}$$

In the above expression, AUC_{surf} refers to the antibody concentration area under the curve (AUC) at the surface of the blood vessel. For the clearance modulus, a value less than one implies that the tumor is penetrated much more rapidly than the drug is cleared from the plasma. Conversely, a value greater than one implies that the drug is cleared from the plasma before it is able to fully penetrate the tumor. In the case of antibodies, the clearance modulus is generally much less than one. This is the case largely because antibodies have very long serum half-lives, on the order of weeks in humans, due to neonatal Fc rescue and recycling⁷. For other therapeutic proteins which have shorter half-lives, the clearance modulus often indicates that plasma clearance may limit tumor penetration. However, for antibodies, plasma clearance is generally not a limiting factor.

The second dimensionless parameter developed to examine tumor transport was termed the Thiele modulus after the analogous engineering parameter utilized in the study of chemical catalysis. The Thiele modulus compares the rate of extravasation and diffusion into the tumor to the rate of antigen-mediated catabolism within the tumor. It can be expressed mathematically as:

$$\phi^2 = \frac{\text{Extravasation and diffusion time}}{\text{Catabolism time}} = \frac{k_e R_{Krogh}^2 \left(\frac{[Ag]}{\epsilon} \right)}{D \left(\frac{2PR_{cap} [Ab]_{plasma}}{D} + K_d \right)}$$

The terms in this expression will be discussed in detail in section 1.4. Values of the Thiele modulus less than one imply that the rate of extravasation and diffusion is faster than the rate of catabolism, and the tumor will be saturated. Values greater than one indicate that catabolism outweighs extravasation and diffusion, and that the catabolic sink will prevent antibody from fully penetrating the tumor. The Thiele modulus is often on the order of unity, and so can give valuable information about whether a tumor will be penetrated. In addition, this simple mathematical expression can be used to give quantitative information about which parameters may be limiting tumor penetration.

1.4 Tunable targeting parameters

The dimensional analysis of the Thiele modulus is a valuable quantitative predictor of tumor penetration. Similar analyses have proven useful and quantitatively accurate in *in vitro* studies, and the Thiele modulus represents an extension to considerations of *in vivo* tumor penetration, namely the inclusion of the extravasation and diffusion steps. Importantly, the parameters that make up the Thiele modulus are parameters which can be experimentally measured, and in many cases are well published in the literature. A discussion of the various parameters and how they might be altered with the goal of enhancing *in vivo* tumor penetration follows below.

Endocytosis rate (k_e)—Rate at which tumor antigen is endocytosed. When antibody-bound antigen is endocytosed, antigen-mediated clearance and degradation of the antibody can be substantial^{40,46,73–75}. Antigen endocytosis rates can vary over several orders of magnitude, from antigen half lives on the order of minutes to constitutive membrane turnover on the order of 12-15 hours. Targeting antigens with slower endocytosis rates can improve tissue penetration by limiting antigen-mediated antibody catabolism. Some antibody therapeutics, such as immunotoxins, must be internalized to effectively deliver their cytotoxic payload. For these therapeutics, faster endocytosis rates may be advantageous, and this must be balanced against the transport limitations caused by high levels of antigen-mediated internalization and degradation.

Krogh cylinder radius (R_{Krogh}) – The Krogh cylinder radius is the radius of the idealized cylinder of tissue surrounding a blood vessel. It was proposed as a model for oxygen and nutrient delivery to muscle tissue, where capillary beds are orderly and vessels are typically parallel and evenly spaced⁷⁶. The Krogh cylinder radius determines the volume of tissue which surrounds a vessel and must be supplied with oxygen and nutrients, or in the case of tumor tissue targeted by therapeutic antibodies. Larger radii imply less dense vascularization, and increase the distance that antibodies must penetrate the tissue to achieve saturation.

Antigen density ($[Ag]$) –Antigen density, or antigen concentration, is a function of the cell density and the number of antigens per cell. In most tumors, cell density is similar, and so the number of antigens per cell is the main factor determining the antigen density. Most therapeutic antibodies target antigens which are upregulated in cancer and so often highly expressed. However, it should be noted that antigen expression can vary significantly, often over orders of magnitude, even within the same tumor type. There is even evidence that tumors can alter their antigen expression in response to therapy⁷⁷. In general, high antigen expression creates more “targets” for antibodies to bind, and so can impede tissue penetration. The number or fraction of antigens which are desired to be bound is also different for different mechanisms of action. For example, ligand-blocking antibodies must occupy as many antigens

as possible, while immunotoxins may be cytotoxic at levels that bind only a small fraction of the antigen available.

Void fraction (ϵ) –The void fraction is the fraction of the tumor that is accessible to the antibody. It is a function of the size of the molecule⁷⁸. Smaller molecules have a higher void fraction, as they can fit into smaller pores and fluid spaces. Macromolecules such as antibodies, antibody fragments, and nanoparticles have a much lower void fraction, which serves to increase the apparent antigen concentration.

Diffusivity (D) – Molecular diffusivity of the molecule. The diffusivity determines how quickly a molecule moves through a fluid space, such as the tumor interstitium. It is a function of molecular radius, with diffusivity decreasing with increasing molecular radius. It has been shown that for molecules around the size of antibodies and in the affinity range of most therapeutic antibodies, the rate of diffusion is small compared to the rate of binding, and antibodies typically bind free antigen within the first layer of cells that they encounter²².

Permeability (P) –Vascular permeability of the tumor capillary. The permeability of tumor blood vessels is typically much greater than that of normal blood vessels^{26,53,79}. Permeability is also a function of molecular size, and larger molecules can have dramatically lower permeability than smaller molecules⁷⁸. Vascular permeability can be measured *in vivo* using techniques such as dynamic contrast enhanced magnetic resonance imaging (DCE-MRI). The permeability of tumor blood vessels is a parameter which can be altered by pharmacological means. Some researchers have argued that some therapeutics such as Avastin, an anti-VEGF antibody, are efficacious in part because they decrease tumor vascular permeability to a range more characteristic of healthy vessels and “normalize” tumor vessels^{64,80–82}. These vessels would have permeabilities near the range of healthy vessels, leading to a restoration of a pressure different between the vessel lumen and the interstitium and inducing convective flow of blood components into the tumor⁶⁴. Other researchers have argued that tumor vessels should be made more permeable, through the use of pharmacological agents such as vascular disrupting agents or by use of localized hyperthermia^{83–86}. The increased permeability is thought to facilitate the diffusion of macromolecules through the blood vessels, resulting in greater tumor

delivery. Recent research has supported both arguments, and there is mounting evidence to suggest that changes to vascular permeability can be transient and that therapeutic “windows” of altered vascular permeability may be present but do not exist for long time periods^{32,53,87,88}.

Capillary radius (R_{cap}) –Radius of the capillary at the center of the Krogh cylinder. The capillary radius determines the surface area of the vessel, which in turn determines the rate at which antibody can extravasate. Larger vessels present larger surface areas, and so enable a greater extravasation rate. Animal models and clinical data have shown that tumor vessels are highly irregular, often poorly formed, and suffer from poor perfusion and variations of blood flow rates both spatially and temporally. These pathologies of the vasculature contribute to the heterogeneous nature of the tumor microenvironment.

Antibody dose ($[Ab]_{plasma}$) –The dose of the antibody administered. Antibodies are administered intravenously, giving them immediate access to the systemic circulation. Antibody doses are typically limited by the nonspecific toxicity of the antibodies. Some antibody-based therapeutics, such as immunotoxins, are particularly toxic and often must be dosed at only a fraction of the dose at which the naked antibody can be safely administered^{17,89}. Higher antibody doses increase tissue penetration in multicellular spheroid models as well as in xenograft tumor models. Evidence is sparse and somewhat mixed regarding how well tumor tissue is penetrated at doses typically administered in clinical settings^{28,90}.

Antibody affinity (K_d) –The binding affinity of the antibody to its target antigen. The antibody affinity is a property that can be engineered. Therapeutic antibodies are typically high affinity, which for the purposes of tumor targeting often means that the characteristic time for unbinding is quite long relative to the other relevant rates, such as diffusion, binding, and degradation, and so in many cases the antibody can be considered irreversibly bound. At lower affinities, antibodies will unbind more rapidly. At very low affinities, antibodies will bind only very briefly before unbinding. In this extreme, the tissue penetration is expected to be excellent, but the fraction of antibody bound will be very low. The antibody affinity is a parameter that can be tuned to provide the desired balance between homogeneous tissue distribution and degree of antigen binding.

1.5 Thesis overview

In this thesis, we aim to study the distribution of antibodies in solid tumors. We seek to explore the properties of the antibody and the antigen that determine how antibodies distribute in the tumor, and to predict behavior using mathematical modeling. In Chapter 2, we develop an experimental toolbox that allows the quantitative determination of antibody and antigen distribution in solid tumor xenograft sections. We then apply this toolbox and mathematical modeling to determine the effect of antibody dose and antigen endocytosis rate on the distribution of the antibody within the tumor. In Chapter 3, we explore the effects of antibody affinity on the distribution of the antibody and the accumulation of the antibody in the tumor. Chapter 4 is a study of several different antibody dosing schedules to determine their effects on tumor control and attempt to correlate efficacy to antibody distribution and penetration into tumor tissue. Chapter 5 examines the effect of xenograft tumor location in a mouse model, comparing two cell lines in orthotopic and ectopic locations to determine whether tumor location influences properties of antibody delivery and distribution. Lastly, Chapter 6 details the development of a novel autochthonous mouse model of cancer. This model is engineered to knock out the p53 tumor suppressor and constitutively activate the K-Ras oncogene, leading to development of a cancer which mimics human cancer in its genesis and pathology. This model is altered by the addition of a virally delivered antigen which allows the study of antibody therapy in an autochthonous, immunocompetent mouse model of cancer.

1.6 References

1. Hanahan, D. & Weinberg, R. A. The Hallmarks of Cancer. *Cell* **100**, 57–70 (2000).
2. Ferlay J *et al.* Cancer Incidence and Mortality Worldwide: IARC CancerBase No. 10 [Internet]. *GLOBOCAN 2008 v1.2* at <<http://globocan.iarc.fr>>
3. Jemal, A. *et al.* Cancer Statistics, 2008. *CA: A Cancer Journal for Clinicians* **58**, 71–96 (2008).
4. American Cancer Society *Cancer Facts and Figures 2012*. (2012).
5. Weissleder, R. & Pittet, M. J. Imaging in the era of molecular oncology. *Nature* **452**, 580–589 (2008).
6. Scott, A. M., Wolchok, J. D. & Old, L. J. Antibody therapy of cancer. *Nature Reviews Cancer* **12**, 278 (2012).
7. Roopenian, D. C. & Akilesh, S. FcRn: the neonatal Fc receptor comes of age. *Nature Reviews Immunology* **7**, 715–725 (2007).
8. Robert A. Beckman, Louis M. Weiner & Hugh M. Davis Antibody Constructs in Cancer Therapy: Protein Engineering Strategies to Improve Exposure in Solid Tumors. *Cancer* **109**, 170–179 (2006).
9. Weiner, L. M. Building better magic bullets |[[mdash]] improving unconjugated monoclonal antibody therapy for cancer. *Nature Reviews Cancer* **7**, 701–706 (2007).
10. Eric T. Boder & Wei Jiang Engineering antibodies for cancer therapy. *Annual Review of Chemical and Biomolecular Engineering* **2**, 1–23 (2011).
11. Graff, C. P., Chester, K., Begent, R. & Wittrup, K. D. Directed evolution of an anti-carcinoembryonic antigen scFv with a 4-day monovalent dissociation half-time at 37 C. *Protein Engineering, Design & Selection* **17**, 293–304 (2004).
12. Presta, L. G. Engineering of therapeutic antibodies to minimize immunogenicity and optimize function. *Advanced Drug Delivery Reviews* **58**, 640–656 (2006).
13. PhRMA *Medicines in Development: Cancer*. (2012).
14. Adams, G. P. & Weiner, L. M. Monoclonal antibody therapy of cancer. *Nature Biotechnology* **23**, 1147–1159 (2005).
15. Sato, N. *et al.* Intratumoral Distribution of Radiolabeled Antibody and Radioimmunotherapy in Experimental Liver Metastases Model of Nude Mouse. *J Nucl Med* **40**, 685–692 (1999).

16. Elgqvist, J. *et al.* Therapeutic efficacy and tumor dose estimations in radioimmunotherapy of intraperitoneally growing OVCAR-3 cells in nude mice with 211-At-labeled monoclonal antibody MX35. *Journal of Nuclear Medicine* **46**, 1907–1915 (2005).
17. Senter, P. D. Potent antibody drug conjugates for cancer therapy. *Current Opinion in Chemical Biology* **13**, 235–244 (2009).
18. Lambert, J. M. Drug-conjugated monoclonal antibodies for the treatment of cancer. *Current Opinion in Pharmacology* **5**, 543–549 (2005).
19. Agemy, L. *et al.* Targeted nanoparticle enhanced proapoptotic peptide as potential therapy for glioblastoma. *Proceedings of the National Academy of Sciences* (2011).doi:10.1073/pnas.1114518108
20. Kirpotin, D. B. *et al.* Antibody targeting of long-circulating lipidic nanoparticles does not increase tumor localization but does increase internalization in animal models. *Cancer Research* **66**, 6732–6740 (2006).
21. Strebhardt, K. & Ullrich, A. Paul Ehrlich's magic bullet concept: 100 years of progress. *Nature Reviews Cancer* **8**, 473–480 (2008).
22. Thurber, G. M., Schmidt, M. & Wittrup, K. D. Antibody tumor penetration: Transport opposed by systemic and antigen-mediated clearance. *Advanced Drug Delivery Reviews* (2008).
23. Thurber, G. M., Zajic, S. C. & Wittrup, K. D. Theoretic Criteria for Antibody Penetration into Solid Tumors and Micrometastases. *Journal of Nuclear Medicine* **48**, 995–999 (2007).
24. Emir, E. E. *et al.* Predicting response to radioimmunotherapy from the tumor microenvironment of colorectal carcinomas. *Cancer Research* **67**, 11896–11905 (2007).
25. Baish, J. W. *et al.* Role of tumor vascular architecture in nutrient and drug delivery: An invasion percolation-based network model. *Microvascular Research* **51**, 327–346 (1996).
26. Gerlowski, L. E. & Jain, R. K. Microvascular permeability of normal and neoplastic tissues. *Microvascular Research* **31**, 288–305 (1986).
27. Harris, L. J., Larson, S. B., Hasel, K. W. & McPherson, A. Refined structure of an intact IgG2a monoclonal antibody. *Biochemistry* **36**, 1581–1597 (1997).
28. Scott, A. M. *et al.* A Phase I Trial of Humanized Monoclonal Antibody A33 in Patients with Colorectal Carcinoma: Biodistribution, Pharmacokinetics, and Quantitative Tumor Uptake. *Clin Cancer Res* **11**, 4810–4817 (2005).
29. Scott, A. M. *et al.* Specific Targeting, Biodistribution, and Lack of Immunogenicity of Chimeric Anti-GD3 Monoclonal Antibody KM871 in Patients With Metastatic Melanoma: Results of a Phase I Trial. *JCO* **19**, 3976–3987 (2001).

30. Schneider, D. W. *et al.* In vivo biodistribution, PET imaging, and tumor accumulation of 86Y- and 111In-Antimindin/RG-1, engineered antibody fragments in LNCaP tumor-bearing nude mice. *Journal of Nuclear Medicine* **50**, 435–443 (2009).
31. Orcutt, K. D., Rhoden, J. J., Ruiz-Yi, B., Frangioni, J. V. & Wittrup, K. D. Effect of Small Molecule Binding Affinity on Tumor Uptake In Vivo. *Mol Cancer Ther* (2012).doi:10.1158/1535-7163.MCT-11-0764
32. Pastuskovas, C. V. *et al.* Effects of anti-VEGF on pharmacokinetics, biodistribution and tumor penetration of trastuzumab in a preclinical breast cancer model. *Molecular Cancer Therapeutics* (2012).doi:10.1158/1535-7163.MCT-11-0742-T
33. David G. Kirsch *et al.* Imaging primary lung cancers in mice to study radiation biology. *International Journal of Radiation Oncology, Biology, Physics* **76**, 973–977 (2010).
34. Sosnovik, D. E. & Weissleder, R. Emerging concepts in molecular MRI. *Current Opinion in Biotechnology* **18**, 4–10 (2007).
35. Frangioni, J. V. In vivo near-infrared fluorescence imaging. *Current Opinion in Chemical Biology* **7**, 626–634 (2003).
36. Lyons, S. K. Advances in imaging mouse tumour models in vivo. *Journal of Pathology* **205**, 194–205 (2005).
37. Koo, V., Hamilton, P. W. & Williamson, K. Non-invasive in vivo imaging in small animal research. *Cellular Oncology* **28**, 127–139 (2006).
38. Weissleder, R. Scaling down imaging: Molecular mapping of cancer in mice. *Nature Reviews Cancer* **2**, 1–8 (2002).
39. Emmenegger, U. *et al.* Pharmacodynamic and pharmacokinetic study of chronic low-dose metronomic cyclophosphamide therapy in mice. *Molecular Cancer Therapeutics* **6**, 2280–2289 (2007).
40. Urva, S. R., Yang, V. C. & Balthasar, J. P. Physiologically based pharmacokinetic model for T84.66: A monoclonal anti-CEA antibody. *Journal of Pharmaceutical Sciences* **99**, 1582–1600 (2009).
41. Baxter, L. T., Zhu, H., Mackensen, D. G., Butler, W. F. & Jain, R. K. Biodistribution of Monoclonal Antibodies: Scale-up from Mouse to Human Using a Physiologically Based Pharmacokinetic Model. *Cancer Res* **55**, 4611–4622 (1995).
42. Rhoden, J. J. & Wittrup, K. D. Dose dependence of intratumoral perivascular distribution of monoclonal antibodies. *Journal of Pharmaceutical Sciences* **101**, 860–867 (2012).
43. Freeman, D. J. *et al.* Tumor penetration and epidermal growth factor receptor saturation by panitumumab correlate with antitumor activity in a preclinical model of human cancer. *Molecular Cancer* **11**, 47 (2012).

44. Minchinton, A. I. & Tannock, I. F. Drug penetration in solid tumours. *Nature Reviews Cancer* **6**, 583–592 (2006).
45. Adams, G. P. *et al.* High affinity restricts the localization and tumor penetration of single-chain Fv antibody molecules. *Cancer Research* **61**, 4750–4755 (2001).
46. Rudnick, S. I. *et al.* Influence of Affinity and Antigen Internalization on the Uptake and Penetration of Anti-HER2 Antibodies in Solid Tumors. *Cancer Research* **71**, 2250–2259 (2011).
47. Fujimori, K., Covell, D., Fletcher, J. & Weinstein, J. A Modeling Analysis of Monoclonal Antibody Percolation Through Tumors - a Binding-Site Barrier. *J. Nucl. Med.* **31**, 1191–1198 (1990).
48. Baker, J. H. E. *et al.* Direct visualization of heterogeneous extravascular distribution of trastuzumab in human epidermal growth factor receptor type 2 overexpressing xenografts. *Clinical Cancer Research* **14**, 2171–2179 (2008).
49. Carol M Lee & Ian F Tannock The distribution of the therapeutic monoclonal antibodies cetuximab and trastuzumab within solid tumors. *BMC Cancer* **10**, (2010).
50. Oosterwijk, E. *et al.* Antibody localization in human renal-cell carcinoma: A phase I study of monoclonal antibody G250. *Journal of Clinical Oncology* **11**, 738–750 (1993).
51. Deen, W. M. Hindered transport of large molecules in liquid-filled pores. *AIChE Journal* **33**, 1409–1425 (1987).
52. Lawrence J. Nugent & Rakesh K. Jain Pore and fiber-matrix models for diffusive transport in normal and neoplastic tissues. *Microvasc Res* **28**, 270–274 (1984).
53. Weis, S. M. & Cheresh, D. A. Pathophysiological consequences of VEGF-induced vascular permeability. *Nature* **437**, 497–504 (2005).
54. Folkman, J. How Is Blood Vessel Growth Regulated in Normal and Neoplastic Tissue?—G. H. A. Clowes Memorial Award Lecture. *Cancer Res* **46**, 467–473 (1986).
55. Folarin, A. A., Konerding, M. A., Timonen, J., Nagl, S. & Pedley, R. B. Three-dimensional analysis of tumour vascular corrosion casts using stereoimaging and micro-computed tomography. *Microvascular Research* **80**, 89–98 (2010).
56. Pedley, R. B. *et al.* Synergy between vascular targeting agents and antibody-directed therapy. *International Journal of Radiation Oncology, Biology, Physics* **54**, 1524–1531 (2002).
57. Ribatti, D., Nico, B., Crivellato, E. & Vacca, A. The structure of the vascular network of tumors. *Cancer Letters* **248**, 18–23 (2007).
58. Sun, C., Jain, R. K. & Munn, L. L. Non-uniform plasma leakage affects local hematocrit and blood flow: Implications for inflammation and tumor perfusion. *Annals of Biomedical Engineering* **35**, 2121–2129 (2007).

59. Martinive, P. *et al.* Reversal of temporal and spatial heterogeneities in tumor perfusion identifies the tumor vascular tone as a tunable variable to improve drug delivery. *Molecular Cancer Therapeutics* **5**, 1620–1627 (2006).
60. Kan, Z. *et al.* Function CT for quantifying tumor perfusion in antiangiogenic therapy in a rat model.
61. Baxter, L. T. & Jain, R. K. Transport of Fluid and Macromolecules in Tumors I: Role of Interstitial Pressure and Convection. *Microvascular Research* **37**, 77–104 (1989).
62. El-Kareh, A. W. & Secomb, T. W. Effect of increasing vascular hydraulic conductivity on delivery of macromolecular drugs to tumor cells. *International Journal of Radiation Oncology*Biography*Physics* **32**, 1419–1423 (1995).
63. Hagendoorn, J. *et al.* Onset of abnormal blood and lymphatic vessel function and interstitial hypertension in early stages of carcinogenesis. *Cancer Research* **66**, 3360–3364 (2006).
64. Jain, R. K., Tong, R. T. & Munn, L. L. Effect of vascular normalization by antiangiogenic therapy on interstitial hypertension, peritumor edema, and lymphatic metastasis: Insights from a mathematical model. *Cancer Research* **67**, 2729–2735 (2007).
65. Heldin, C.-H., Rubin, K., Pietras, K. & Östman, A. High interstitial fluid pressure—an obstacle in cancer therapy. *Nature Reviews Cancer* **4**, 806–813 (2004).
66. Milosevic, M. F., Fyles, A. W. & Hill, R. P. The relationship between elevated interstitial fluid pressure and blood flow in tumors: A bioengineering analysis. *International Journal of Radiation Oncology*Biography*Physics* **43**, 1111–1123 (1999).
67. Wu, J. *et al.* Coupled modeling of blood perfusion in intravascular, interstitial spaces in tumor microvasculature. *Journal of Biomechanics* **41**, 996–1004 (2008).
68. Chary, S. R. & Jain, R. K. Direct measurement of interstitial convection and diffusion of albumin in normal and neoplastic tissues by fluorescence photobleaching. *Proceedings of the National Academy of Science* **86**, 5385–5389 (1989).
69. Laurence T. Baxter & Rakesh K. Jain Transport of fluid and macromolecules in tumors: 3. Role of binding and metabolism. *Microvascular Research* **41**, 5–23
70. Kyriakos, R. J. *et al.* The Fate of Antibodies Bound to the Surface of Tumor Cells in Vitro. *Cancer Res* **52**, 835–842 (1992).
71. Hicks, K. O. *et al.* Use of three-dimensional tissue cultures to model extravascular transport and predict in vivo activity of hypoxia-targeted anticancer drugs. *Journal of the National Cancer Institute* **98**, 1118–1128 (2006).

72. Greg M. Thurber & K. Dane Wittrup Quantitative Spatiotemporal Analysis of Antibody Fragment Diffusion and Endocytic Consumption in Tumor Spheroids. *Cancer Res* **68**, 3334–3341 (2008).
73. Ackerman, M. E., Pawlowski, D. & Wittrup, K. D. Effect of antigen turnover rate and expression level on antibody penetration into tumor spheroids. *Molecular Cancer Therapeutics* **7**, 2233–2240 (2008).
74. Velden, V. van der *et al.* High CD33-antigen loads in peripheral blood limit the efficacy of gemtuzumab ozogamicin (Mylotarg) treatment in acute myeloid leukemia patients. *Leukemia* **18**, 983–988 (2004).
75. Zuckier, L. S. *et al.* Influence of affinity and antigen density on antibody localization in a modifiable tumor targeting model. *Cancer Research* **60**, 7008–2013 (2000).
76. Krogh, A. The number and distribution of capillaries in muscles with calculations of the oxygen pressure head necessary for supplying the tissue. *J Physiol* **52**, 409–415 (1919).
77. Tredan, O., Galmarini, C. M., Patel, K. & Tannock, I. F. Drug resistance and the solid tumor microenvironment. *Journal of the National Cancer Institute* **99**, 1441–1454 (2007).
78. Michael M. Schmidt & K. Dane Wittrup A modeling analysis of the effects of molecular size and binding affinity on tumor targeting. *Mol Cancer Ther* **8**, 2861–2871 (2009).
79. Maeda, H., Wu, J., Sawa, T., Matsumura, Y. & Hori, K. Tumor vascular permeability and the EPR effect in macromolecular therapeutics: a review. *Journal of Controlled Release* **65**, 271–284 (2000).
80. Chauhan, V. P. *et al.* Normalization of tumour blood vessels improves the delivery of nanomedicines in a size-dependent manner. *Nature Nanotechnology* (2012).doi:10.1038/nnano.2012.45
81. Tong, R. T. *et al.* Vascular normalization by vascular endothelial growth factor receptor 2 blockade induces a pressure gradient across the vasculature and improves drug penetration in tumors. *Cancer Research* **64**, 3731–3737 (2004).
82. Ferrara, N., Hillan, K. J., Gerber, H.-P. & Novotny, W. Discovery and development of bevacizumab, an anti-VEGF antibody for treating cancer. *Nature Reviews Drug Discovery* **3**, 391–400 (2004).
83. Skliarenko, J. V. *et al.* Effects of the vascular disrupting agent ZD6126 on interstitial fluid pressure and cell survival in tumors. *Cancer Research* **66**, 2074–2080
84. Leach, M. O. *et al.* The assessment of antiangiogenic and antivascular therapies in early-stage clinical trials using magnetic resonance imaging: issues and recommendations. *British Journal of Cancer* **92**, 1599–1610 (2005).

85. Hauck, M. L., Dewhirst, M. W., Bigner, D. D. & Zalutsky, M. R. Local hyperthermia improves uptake of a chimeric monoclonal antibody in a subcutaneous xenograft model. *Clinical Cancer Research* **3**, 63–70 (1997).
86. Kong, G., Braun, R. D. & Dewhirst, M. W. Characterization of the effect of hyperthermia on nanoparticle extravasation from tumor vasculature. *Cancer Research* **61**, 3027–3032 (2001).
87. Dafni, H., Landsman, L., Schechter, B., Kohen, F. & Neeman, M. MRI and fluorescence microscopy of the acute vascular response to VEGF165: vasodilation, hyper-permeability and lymphatic uptake, followed by rapid inactivation of the growth factor. *NMR in Biomedicine* **15**, 120–131 (2002).
88. Winkler, F. *et al.* Kinetics of vascular normalization by VEGFR2 blockade governs tumor response to radiation: Role of oxygenation, angiopoietin-1, and matrix metalloproteinases. *Cancer Cell* **6**, 553–563 (2004).
89. Krop, I. E. *et al.* Phase I Study of Trastuzumab-DM1, an HER2 Antibody-Drug Conjugate, Given Every 3 Weeks to Patients With HER2-Positive Metastatic Breast Cancer. *JCO* **28**, 2698–2704 (2010).
90. Blakey, D. C. Factors Impacting the Tumor Localization and Distribution of Antibody-Based Therapeutics in Oncology. *Development of Antibody-Based Therapeutics* 241–253 (2012).at <<http://www.springerlink.com/content/n7j2l65125106385/abstract/>>

2. ANTIBODY DOSE VS. TUMOR PENETRATION

2.1 Introduction

Antibodies represent a significant and rapidly growing proportion of oncology therapeutics¹. While many have found success in a range of cancers, particularly hematologic malignancies, there remain substantial barriers to the effective use of antibodies to treat solid tumors. Solid tumors present a number of barriers to tumor targeting and penetration, including blood clearance, extravasation, diffusion through the interstitial space, binding to antigen, endocytosis, and degradation^{2,3}. Many of these barriers are further exacerbated by the disordered physiology of solid tumors which results in highly permeable and irregular vasculature and high interstitial fluid pressure⁴⁻⁶. For decades, researchers have noted that penetration into solid tumor tissue is often limited for drugs ranging in size and mechanism of action from chemotherapeutics to antibodies and nanoparticles^{3,4,7-11}. Limited penetration has been linked to reduced therapeutic efficacy, even in cases in which bulk tumor uptake is high enough to exert an anti-tumor effect with a well distributed therapeutic^{12,13}. Recently, it was shown that the FDA-approved monoclonal antibodies cetuximab, trastuzumab, and panitumumab penetrate poorly into tumors in animal xenograft models¹³⁻¹⁵.

Quantitative *in vitro* studies of antibody delivery to and distribution within tumor spheroids have yielded insights into the roles that antibody affinity and antigen internalization play in this process^{16,17}. *In vivo*, for a range of antibodies, antigens, and cell lines, extravasation from tumor blood vessels has been shown to display a characteristic perivascular distribution in which tumor cells within a few cell layers of perfused vessels are often saturated with antibody, but more distal regions show little to no evidence of therapeutic targeting^{7,8,12,14,15}. Common bulk measures of tumor uptake such as percent injected dose per gram fail to differentiate the heterogeneity of tumor targeting at the microscopic scale.

Here, we present an *in vivo* study of monoclonal antibody and antigen distribution around tumor blood vessels as a function of antibody dose covering two orders of magnitude. A computer-aided method of analyzing entire tumor cross sections in a quantitative and unbiased

manner is utilized to generate data. These results are consistent with a Krogh cylinder model and scaling analysis which predict the antibody dose necessary to saturate a tumor for a given antigen cell surface expression level and metabolic half-life. Although these modeling analyses are dramatic oversimplifications of the tumor microenvironment, they are nonetheless successful in quantitatively predicting the distribution of extravasated antibody averaged over the tumor cross section.

2.2 Materials and methods

Reagents

A low-picomolar humanized antibody to carcinoembryonic antigen (CEA), designated sm3e, has previously been engineered and characterized¹⁸. This antibody was secreted in transiently transfected HEK 293 cells (Invitrogen, Carlsbad, CA), purified by protein A resin (Millipore, Billerica, MA) and buffer exchanged into PBS. The antibody was fluorescently labeled using the Alexa Fluor 488 Protein Labeling kit from Invitrogen (Carlsbad, CA). Labeling was conducted in a single batch of approximately 3 mg protein to yield a homogeneously labeled reagent source for all experiments presented. Anti-CEA monoclonal antibody M85151a was purchased from Fitzgerald (Acton, MA) and goat anti-rat 546 secondary antibody from Invitrogen. Antibody M85151a was labeled with an Alexa Fluor 647 Protein Labeling kit and has been previously determined to be noncompetitive with sm3e¹⁹.

Animal model

Animal use and care was conducted in full compliance and under approval from the MIT Committee on Animal Care. A CEA-positive human colorectal cancer cell line, LS174T, was used to induce xenograft formation in the flanks of 6-8 week old Ncr nude mice (Taconic, Hudson, NY) by subcutaneous injection of 5×10^6 cancer cells. Tumors were allowed to establish and grow to a diameter of 5-10 mm, at which point antibody injections were conducted. Varying doses of fluorescently labeled sm3e, ranging from 5 μ g to 500 μ g, were supplemented as

needed with IgG from human serum (Sigma-Aldrich, St. Louis, MO) to 500 µg total IgG, then injected retroorbitally into tumor bearing nude mice. Mice were sacrificed 24 hours after antibody administration, and tumors were immediately excised and snap frozen in Optimal Cutting Temperature (OCT) medium (Sakura Finetek USA, Torrance, CA) via isopentane over liquid nitrogen. Frozen blocks were stored at -80°C until sectioned by the Koch Institute Histology Core Facility. Frozen blocks were sectioned approximately 1-2 mm into the tumor tissue at a thickness of 8 µm and stored at -80°C until stained and imaged.

Immunofluorescence protocol

Frozen slides were first air dried for approximately 30 minutes, then tissue samples circled with a PAP pen (Invitrogen, Carlsbad, CA). Tissues were fixed for 15 minutes at room temperature in formalin, then washed 3 times with PBS. Blocking was performed with 5% goat serum (Invitrogen) in PBS for 1 hour at room temp. Primary antibody incubation was 5% goat serum in PBS + 1:100 rat anti-mouse CD31 (BD Pharmingen, San Diego, CA) overnight at 4°C. Slides were then washed three times with PBS, then incubated with PBS+0.1% Tween 20 (Sigma-Aldrich, St. Louis, MO) + 1:200 goat anti-rat 546 (Invitrogen, Carlsbad, CA) + 1:100 M85151a-647 anti-CEA antibody (Fitzgerald, Acton, MA) for 1 hour at room temperature. Slides were washed 4 times with PBS, then mounted in Vectashield + DAPI medium (Vector Labs, Burlingame, CA).

Fluorescence imaging

Slides were imaged using a DeltaVision Spectris microscope (Applied Precision, Issaquah, WA) equipped with a motorized stage and running Softworx software (Applied Precision). Emission and excitation filters were arranged to permit simultaneous 4-color imaging of DAPI, 488, 546, and 647. The paneling feature of Softworx was used to capture the entire tumor section at a resolution of 1.336 µm/pixel and to stitch together the fields into a single large mosaic image for subsequent analysis (Figure 2.1).

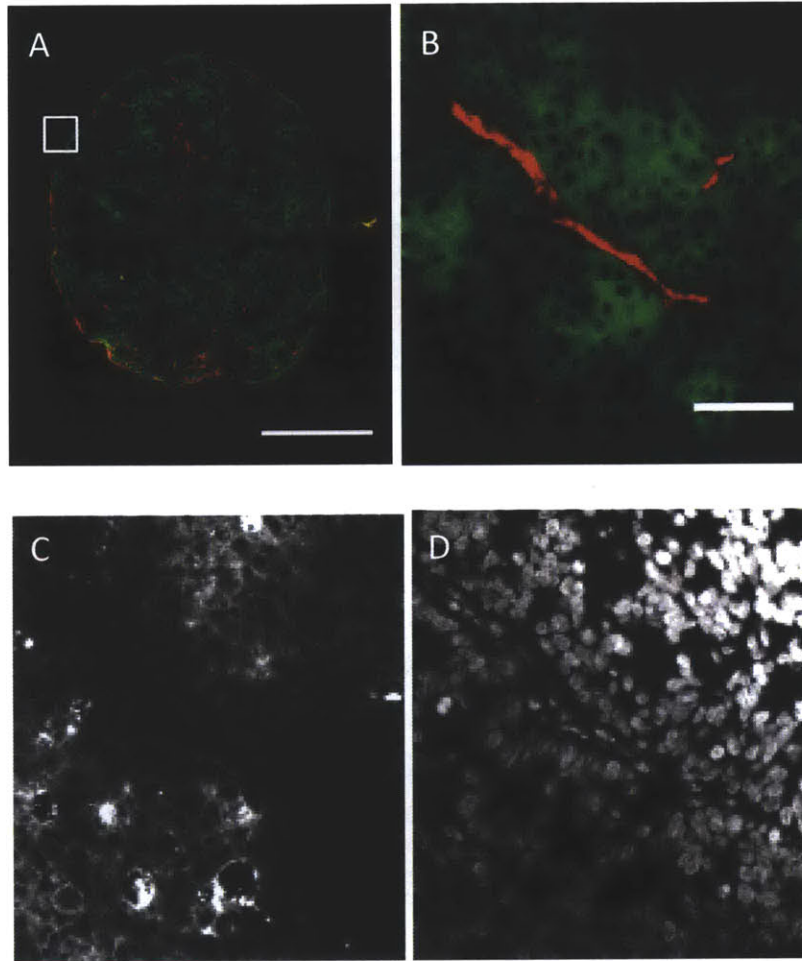


Figure 2.1. Example of resolution and scale of immunofluorescence images. Panel A, full tumor section with antibody pseudocolored green and CD31 (blood vessels) red. Boxed area denotes approximate zoomed region in B,C, and D. Scale bar, 1 mm. Panel B, zoomed area from panel A. Scale bar, 50 μm . Panel C, antigen (CEA) channel in the same region. Panel D, DAPI channel in same region.

2.3 Mathematical modeling

Modeling

Antibody extravasation was modeled using an extension of a previously described Krogh cylinder model of the tumor vasculature as detailed in Appendix A. Criteria for tumor saturation were estimated using the Thiele modulus concept described previously and using parameters extracted from the literature or measured directly in tumor sections. The key assumption underlying the Thiele modulus is that the extent of antibody distribution through

the tumor volume is determined by the balance between endocytic consumption of bound antibody and extravasation/diffusion. The Thiele modulus represents the dimensionless ratio of these competing rates, and is described mathematically as:

$$\phi^2 = \frac{k_e R_{krogh}^2 \left(\frac{[Ag]}{\varepsilon} \right)}{D \left(\frac{2PR_{cap} [Ab]_{plasma}}{D} + K_d \right)}$$

When $\phi^2 = 1$, these characteristic rates are equal and hence saturation of the tumor tissue is approximately achieved. k_e is the endocytic rate constant for antibody/antigen complexes. R is the average distance to the nearest blood vessel in the tumor. $[Ag]$ is the antigen concentration on a per-tumor-volume basis. ε is the fraction of tumor volume accessible to the antibody. D is the diffusivity of the antibody in tumor tissue. P is the vascular permeability coefficient. R_{cap} is the average capillary radius. $[Ab]_{plasma}$ is the peak plasma concentration of antibody. K_D is the antibody/antigen equilibrium dissociation constant. Parameter values are given in Table 1.

In addition to the dimensional analysis used in the Thiele modulus, a numerical simulation based upon the Krogh cylinder geometry was also carried out. This model tracks the concentrations of the antibody, antigen, bound antibody, and internalized antibody species as a function of distance from the blood vessel and time. This model assumes that antibody transport in tumor tissue is dominated by diffusion, as has been shown in the literature^{20,21}. The numerical simulation is carried out using the Matlab software package. Details of the simulation are given in Appendix A.

Krogh cylinder model parameter values			
Parameter	Definition	Value	Citation
ϵ	Tumor void volume	0.2391	²²
D	Diffusivity	2.54×10^{-7} cm ² /s	²²
P	Vascular permeability	3.87×10^{-7} cm/s	²²
R _{Krogh}	Krogh cylinder radius	60 μ m	Measured
R _{cap}	Capillary radius	8 μ m	²³
K _d	Monovalent affinity	10 pM	Measured
[Ag]	Antigen concentration	150 nM	^{24,25}
k _e	Antigen endocytosis rate	$1.3e-5$ s ⁻¹	¹⁹

Table 2.1. Parameter values used in the Thiele modulus analysis of the criteria for tumor saturation in the case of IgG antibodies and using CEA as a model antigen in LS174T tumor xenografts. Values were measured by experiment or taken from the literature.

2.4 Results

Unbiased Image Analysis

Rather than introduce potential observer bias by manually selecting individual blood vessels for analysis, images were analyzed as entire tumor sections for features including intervessel distance, antibody penetration from blood vessels, and antigen distribution. The 546 nm (blood vessel) plane was isolated, thresholded to include vessels only, and converted to a binary image using ImageJ (NIH, Bethesda, MD). A Euclidean distance map was created from the vessel binary, and this map was used as a mask to measure average intensity in the antibody (488) and antigen (647) planes as a function of distance from nearest blood vessel by an automated MATLAB (The Mathworks, Natick, MA) computer script (Figure 2.2). Regions of the tumor revealed to be necrotic or stromal tissue by examination of H&E staining or by absence of antigen were excluded from the analysis.

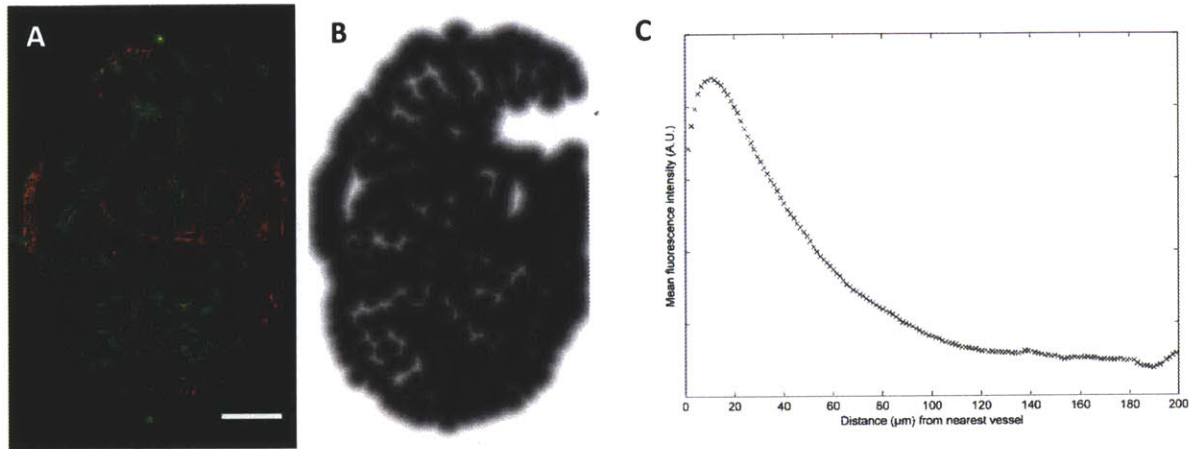


Figure 2.2. A depiction of an example immunofluorescence image. Objects pseudocolored red indicate blood vessels, and green pseudocoloring represents extravasated antibody. Antibody was administered to the tumor-bearing mouse 24 h before euthanasia at a dose of 50 μg . Not shown for clarity are DAPI and antigen, both of which are also imaged with blood vessels and antibody. Scale bar, 1 mm. B, blood vessels have been thresholded and a Euclidean distance map applied to the thresholded vessels. Antigen negative and necrotic regions of the tumor section can be manually removed from the analysis of this image. Pixel intensities are directly proportional to distance from nearest blood vessel. C, Output of the automated MATLAB analysis of antibody distribution from blood vessels. Antibody intensity values at large distances from blood vessels are indistinguishable from those measured in tumors that did not receive antibody. Not shown for clarity is the corresponding antigen distribution.

Microdistribution experimental results

An anti-CEA IgG was dosed at levels ranging from 5 to 500 μg in mice with xenografted LS174T tumors. Mosaic images of full tumor cross sections that have been intensity scaled identically are shown in Figure 2.3. Corresponding imaging of antigen expression in these tumor sections confirms CEA expression throughout.

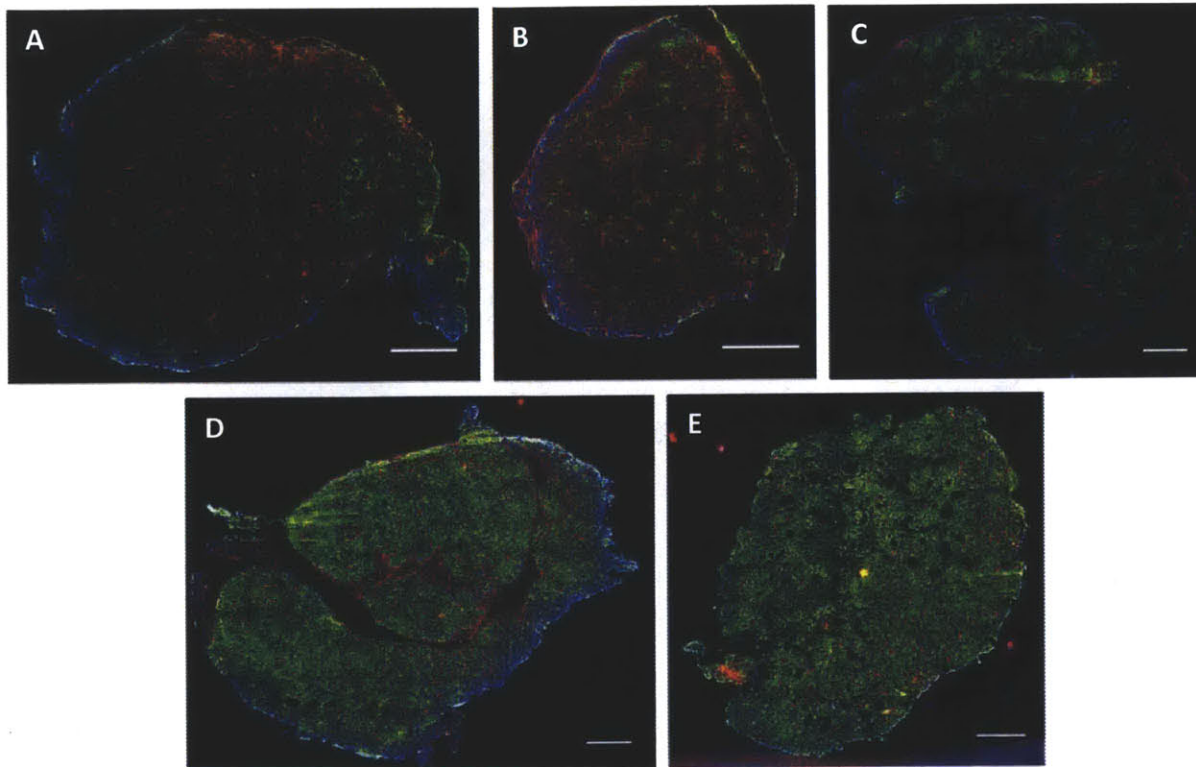


Figure 2.3. Selected images of tumor sections from xenografts in mice administered between 5 and 500 μg of anti-CEA antibody sm3e labeled with Alexa Fluor 488 24 hours before sacrifice and tumor harvest. Blue pseudocolor represents DAPI; green pseudocolor represents sm3e; red pseudocolor represents blood vessels; not shown for clarity is antigen, which was also imaged in each section. Doses were 5, 15, 50, 150, and 500 μg in panels a-e, respectively. Note that low doses at 50 μg or less show clear perivascular distribution, while higher doses of 150 μg and 500 μg appear to show complete saturation of the tumor. All scale bars are 1 mm.

At low antibody doses, ranging from 5 μg to 50 μg , considerable perivascular binding and localization of extravasated antibody is observed, with a general trend of increasing penetration distance and perivascular antibody intensity with increased antibody dose (Figure 2.3 a-c). In contrast, higher doses of 150 and 500 μg show near complete penetration of the tumor, with no clear perivascular distribution of antibody. When tumor sections are analyzed by computer to quantitatively determine microdistribution trends, doses of 5 and 15 μg are seen to display perivascular distribution that then decreases to near background levels approximately 40-50

μm from the blood vessels on average. In contrast, the 50 μg dose also shows enhanced localization adjacent to blood vessels with decreasing signal with distance from vessels beginning approximately 20 μm from the vessel, but this dose retains some degree of specific signal and never drops to background levels. The highest two dose levels which appear to saturate the tumor tissue show no perivascular localization. Essentially all tumor tissue is reached, with marginal additional binding detectable between the 150 and 500 μg doses.

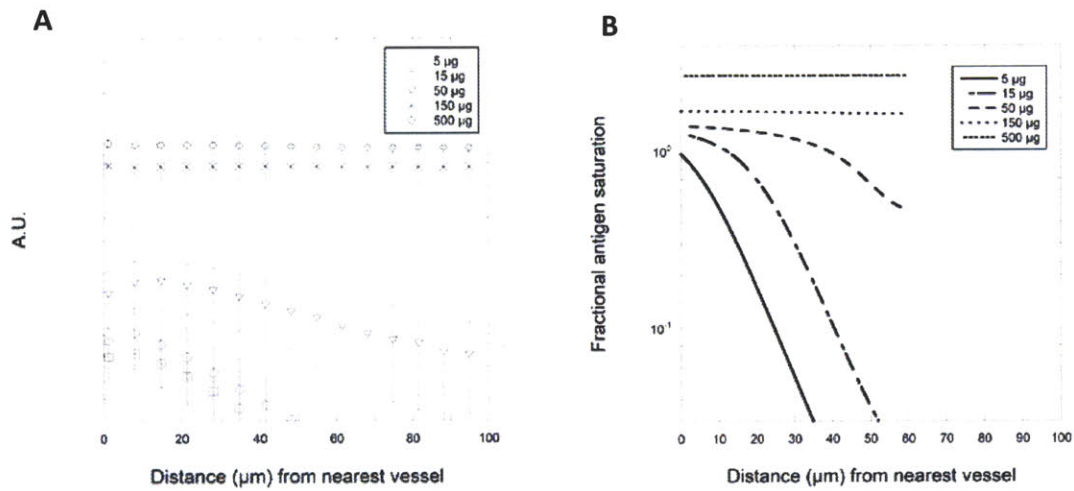


Figure 2.4. Experimentally observed perivascular antibody:antigen distribution ratio as a function of dose (a) and Krogh cylinder based predicted perivascular distribution of extravasated antibody (b). The lower limit for signal in (a) was taken to be three standard deviations over the background signal. Equations and parameters used to generate panel (b) are detailed in Appendix A.

Microdistribution mathematical modeling

To predict how antibody penetration will depend on parameters such as antigen density and endocytic half-life and antibody affinity, a previously described Krogh cylinder-based model was extended (Appendix A)²⁵. Parameter values were determined from the literature where appropriate and from direct measurement in the case of the Krogh cylinder radius. This model includes the effects of blood clearance, extravasation, antibody diffusion through the interstitial space, binding, unbinding, and endocytic clearance. Simulations of single-vessel extravasated

antibody profiles over the experimental dose range show excellent agreement with the experimental results (Figure 2.4). These experimental results represent the averages of the antibody microdistribution from thousands of blood vessels per tumor section analyzed. The model reproduces the perivascular distribution seen at low doses, as well as the complete penetration which occurs at the highest doses and the intermediate condition observed at the 50 μg dose level.

Thiele modulus analysis

For the LS174T tumor and the CEA-targeting sm3e antibody used in this study, tumor saturation appears to occur at a dose between 50 and 150 μg . However, the dose required to saturate a tumor will be dependent on several antibody- and antigen-dependent factors, including antigen density and turnover rate as well as antibody affinity, permeability, diffusivity, and clearance rate. For the case of IgGs, previous analyses have strongly suggested that the factors limiting tumor penetration are not blood clearance related, but instead related to binding and endocytosis of antibody-antigen complexes². A dimensionless number termed the Thiele modulus (ϕ^2) can be used to quantitatively describe the ratio of the rate of binding and endocytosis of an antibody to its rate of extravasation and diffusion into the tumor. This rate of extravasation and diffusion must be greater than the rate of binding and endocytosis (i.e., $\phi^2 < 1$) for the antibody to fully penetrate a given distance. Applying this dimensionless analysis using parameters obtained from the literature or directly measured from experimental data (Table 2.1) allows the determination of saturation criteria for a tumor as a function of antigen density and turnover rate, parameters easily found in the literature or measured for a tumor model of interest (Figure 2.5). Antibody affinity also can play a significant role, as very high affinity antibodies bind essentially irreversibly to tumor antigen and are eventually endocytosed and degraded.

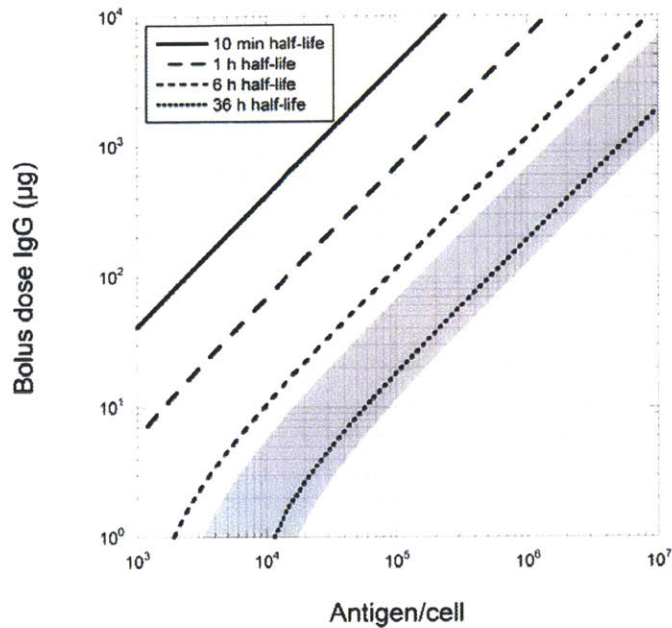


Figure 2.5. Plots of $\phi^2=1$ trendlines as a function of bolus dose IgG injected and number of cell-surface antigens per tumor cell, allowing for the estimation of minimum doses required for tumor saturation. Data are plotted for a wide range of physiologically relevant antigen turnover rates. The shaded band represents a typical range of constitutive turnover half-lives for membrane proteins. Parameters used in model calculations are given in Table 2.1.

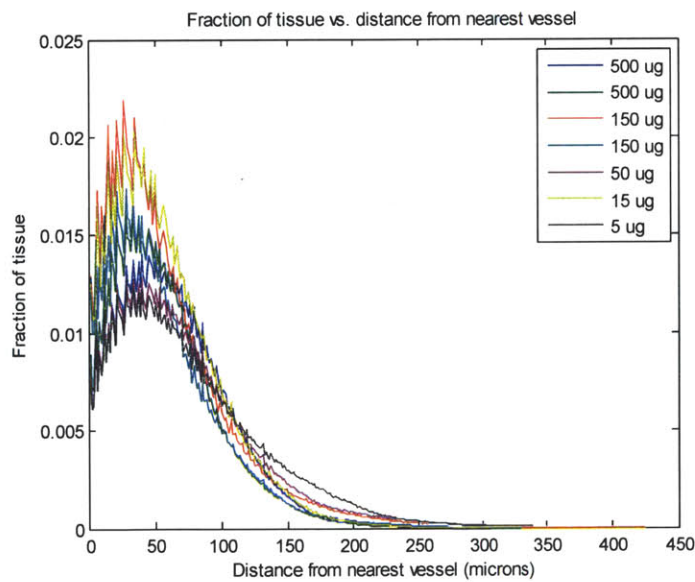
2.5 Discussion

We present here an unbiased image analysis of microdistribution of antibody and antigen in xenograft tumors. The use of appropriately selected fluorophores allows the independent imaging of extravasated antibodies, blood vessels, and antigen in entire xenograft tumor cross sections. The full cross section, less any non-tumor or necrotic areas, can then be analyzed by the use of a MATLAB program that measures and averages the pixel intensities in the antibody and antigen channels for each of the blood vessels in a tumor section. These data represent a snapshot of the average extravasated antibody distribution from all the vessels in an entire tumor section. This two-dimensional cross section of a three dimensional tumor volume can be treated as representative of the tumor volume because the thickness of the section is

approximately 8 μm , which is a negligible distance relative to the typical diameter of the tumor (5-10 mm).

Using this image analysis method, we determined that for the particular antigen and antibody pair used here, complete tumor penetration occurs at a dose between 50 and 150 μg .

Quantitatively, perivascular distribution is clearly observed in low doses (5 and 15 μg), less prominent at 50 μg , and absent at doses which fully penetrate the tumor. Interestingly, the normalized antibody:antigen intensity changes relatively little between the highest dose levels, suggesting that antigen saturation may have occurred and that increasing antibody dose beyond this level has little potential beneficial effect on targeting tumor cells.



Tumor	Krogh cylinder radius (μm)
500 ug	60.1
500 ug	52.1
150 ug	50.1
150 ug	48.1
50 ug	62.8
15 ug	51.8
5 ug	66.8
Average	55.6 ± 7.2

Figure 2.6. Experimental measurement of R_{krogh} in xenograft tumor tissue. Fraction of tissue vs. distance from nearest blood vessel plotted at left for seven randomly selected tumors imaged. Right, determination of median distance from nearest blood vessel for each section shown at left.

A Krogh cylinder model of antibody distribution around a blood vessel was employed to predict these results. This model uses parameters of the antibody and antigen that have been culled from the recent literature, or measured from experimental results in the case of the Krogh cylinder radius. This parameter was estimated directly from intervessel distribution data measured in the tumor sections imaged (Figure 2.6). Using no fit parameters, the model shows excellent agreement with the data. Despite the simplifications inherent in the use of the Krogh cylinder model, the model is able to quantitatively predict the antibody distribution profiles across the dose ranges examined. Low doses indicate an exclusively perivascular distribution, moderate (50 μg) doses show enhanced binding near blood vessels but retain binding much further from the vessel, and high doses show uniform antigen saturation. The model predicts that the highest doses saturate all antigen binding sites; additional antibody accumulation at these high doses is due to unbound antibody that has extravasated into the tumor and is free to diffuse or bind free antigen. The experimental images may not capture this unbound antibody, as during the tumor excision, embedding, sectioning, and immunofluorescent staining processes there are abundant potential opportunities to wash away free antibody.

These concepts can be generalized to different antibody-antigen combinations through the use of the Thiele modulus dimensionless quantity. This number, a ratio of the rate of binding and catabolism to the rate of extravasation and diffusion, succinctly captures the limiting rate processes for long serum half-life therapeutics like antibodies. It should be noted that molecules with substantially shorter half-lives may also be limited by their rapid blood clearance, although this is not the case for IgGs². Setting the Thiele modulus equal to unity, at which point the rates are equal, allows the determination of the minimum criteria for full penetration of a tumor. These criteria will depend upon the easily measured quantities of antigen density and endocytosis rate, as well as antibody properties. Typical antibody properties are used for the plots in Figure 4 and listed in Table 1. The rate of antigen turnover can be seen to have a very strong effect on tumor penetration, suggesting that antigens which are endocytosed as a part of constitutive membrane turnover may be good targets with respect to beneficial intratumoral distribution.

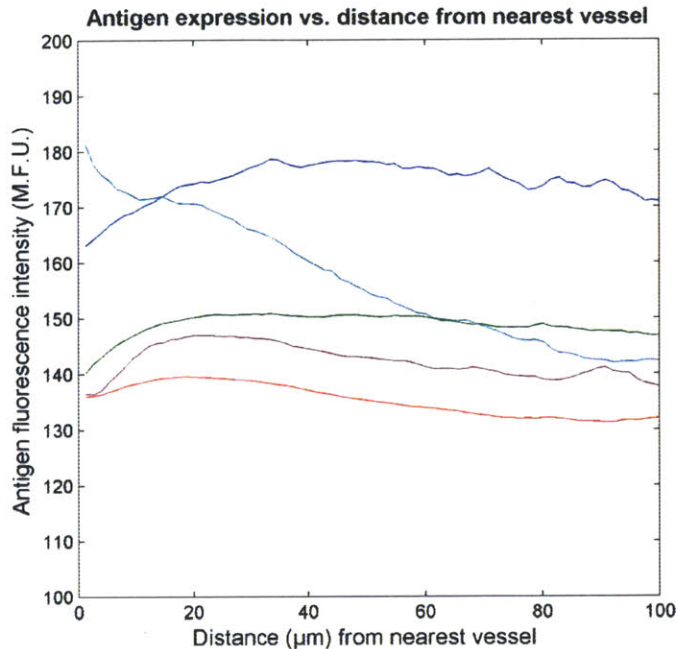


Figure 2.7. CEA expression vs. distance from nearest vessel for 5 randomly selected tumor sections. Examples are typical in that antigen expression is maintained at essentially constant levels through distances of more than 100 μm from vessels, beyond which many of the cells are necrotic.

Antibody affinity may also play a significant role in tumor penetration; the criteria for penetration of a 10 pM binder are markedly different from those of a 1 nM binder. This phenomenon occurs as a consequence of the different time scales of unbinding for high versus moderate affinity binders. High affinity binders rarely dissociate over the lifespan of bound antigen, while moderate affinity binders are more likely to bind multiple antigens, diffusing between each one. This may allow moderate affinity binders to penetrate farther into the tumor than very high affinity binders, albeit at the cost of fewer antibodies per targeted cell. This topic will be addressed in greater detail in Chapter 3.

Quantitative analysis and modeling of perivascular antibody distribution can be a useful window into elucidating the factors which ultimately determine whether a given therapeutic is able to fully penetrate tumor tissue. Experiments using a well characterized antibody-antigen model system *in vivo* provide validation for the mathematical framework and show that tumor

penetration should be possible at antibody doses near the high end of those commonly used in preclinical studies. However, penetration is much easier to achieve for slowly internalizing antigens such as those turned over constitutively with the cell membrane. Actively endocytosed antigens require much larger doses for complete penetration; this is an important consideration for antibody-drug conjugates, which are typically targeted to rapidly internalized antigens. The pharmacodynamic benefits of efficient antibody-drug conjugate internalization are obtained at the micropharmacokinetic cost of impeded tumor penetration.

Inefficient tumor penetration also has potential implications for the theory of tumor growth based upon cancer stem cells (CSCs). There is evidence to suggest that these cells are responsible for the generation of new cancer cells and ultimately the growth, differentiation, and metastasis of tumors²⁶. Under the CSC theory, it is paramount that the CSCs be targeted by any potential therapeutic—if they are not killed, the tumor can be regenerated by the surviving stem cells. However, there is also evidence to suggest that CSCs are often present in hypoxic regions of the tumor which are far from blood vessels **NEED TO FIND CITATIONS HERE**. The CSC theory of tumor growth suggests that penetration of therapeutics into hypoxic regions will be necessary for the success of the treatment. This should be considered when choosing therapeutic targets, as antigens with low endocytosis rates and moderate expression levels will be more conducive to high tissue penetration. Another opportunity to target CSCs might lie in determining antigens which are upregulated or selectively expressed on CSCs, thereby enabling them to be targeted with no or reduced rates of endocytic consumption by normal (non-proliferative) tumor cells located in perivascular regions. Such a strategy might then be combined with “conventional” antibody therapy to eliminate CSCs and tumor cells in a single step.

Consideration must be given to translating tumor penetration and antibody distribution data obtained in preclinical animal models to the clinic. Xenograft models can be unreliable models for preclinical drug efficacy experiments, and moreover morphologically xenograft tumors often poorly resemble the primary tumors from which they were derived^{27–29}. There is limited evidence that poor penetration of antibody therapeutics is observed in clinical cases.

Compellingly, one of the studies most directly showing heterogeneous antibody distribution in the clinic involves an antibody against the antigen A33, which has an extremely slow endocytosis rate and as such is predicted to be a relatively “easy” tumor to penetrate^{16,30,31}. Clinical studies of antibody therapeutics almost always show levels of accumulation of antibody in the tumor as less than 0.1% injected dose/gram. In animal models, typical values are approximately two orders of magnitude higher. This would argue that poor distribution seen in animal models would if anything understate the magnitude of the issue in human patients.

NOTE: This chapter was adapted from work previously published in Rhoden JJ and Wittrup KD. Dose dependence of intratumoral perivascular distribution of monoclonal antibodies. *Journal of Pharmaceutical Sciences* 101: 860-867 (2012).

2.6 References

1. Beckman, R. A., Weiner, L. M. & Davis, H. M. Antibody constructs in cancer therapy. *Cancer* **109**, 170–179 (2007).
2. Thurber, G. M., Schmidt, M. & Wittrup, K. D. Antibody tumor penetration: Transport opposed by systemic and antigen-mediated clearance. *Advanced Drug Delivery Reviews* (2008).
3. Rakesh K. Jain & Triantafyllos Stylianopoulos Delivering nanomedicine to solid tumors. *Nat Rev Clin Oncol* **7**, 653–664 (2010).
4. Minchinton, A. I. & Tannock, I. F. Drug penetration in solid tumours. *Nature Reviews Cancer* **6**, 583–592 (2006).
5. Heldin, C.-H., Rubin, K., Pietras, K. & Östman, A. High interstitial fluid pressure—an obstacle in cancer therapy. *Nature Reviews Cancer* **4**, 806–813 (2004).
6. Gerlowski, L. E. & Jain, R. K. Microvascular permeability of normal and neoplastic tissues. *Microvascular Research* **31**, 288–305 (1986).
7. Tredan, O., Galmarini, C. M., Patel, K. & Tannock, I. F. Drug resistance and the solid tumor microenvironment. *Journal of the National Cancer Institute* **99**, 1441–1454 (2007).
8. Adams, G. P. *et al.* High affinity restricts the localization and tumor penetration of single-chain Fv antibody molecules. *Cancer Research* **61**, 4750–4755 (2001).
9. Oosterwijk, E. *et al.* Antibody localization in human renal-cell carcinoma: A phase I study of monoclonal antibody G250. *Journal of Clinical Oncology* **11**, 738–750 (1993).
10. Yokota, T., Milenic, D. E., Whitlow, M. & Schlom, J. Rapid tumor penetration of a single-chain Fv and comparison with other immunoglobulin forms. *Cancer Research* **52**, 3402–2408 (1992).
11. Flynn, A. A., Boxer, G. M., Begent, R. H. J. & Pedley, R. B. Relationship between tumour morphology, antigen and antibody distribution measured by fusion of digital phosphor and photographic images. *Cancer Immunology Immunotherapy* **50**, 77–81 (2001).
12. Emir, E. E. *et al.* Predicting response to radioimmunotherapy from the tumor microenvironment of colorectal carcinomas. *Cancer Research* **67**, 11896–11905 (2007).
13. Freeman, D. J. *et al.* Tumor penetration and epidermal growth factor receptor saturation by panitumumab correlate with antitumor activity in a preclinical model of human cancer. *Molecular Cancer* **11**, 47 (2012).
14. Carol M Lee & Ian F Tannock The distribution of the therapeutic monoclonal antibodies cetuximab and trastuzumab within solid tumors. *BMC Cancer* **10**, (2010).

15. Baker, J. H. E. *et al.* Direct visualization of heterogeneous extravascular distribution of trastuzumab in human epidermal growth factor receptor type 2 overexpressing xenografts. *Clinical Cancer Research* **14**, 2171–2179 (2008).
16. Ackerman, M. E., Pawlowski, D. & Wittrup, K. D. Effect of antigen turnover rate and expression level on antibody penetration into tumor spheroids. *Molecular Cancer Therapeutics* **7**, 2233–2240 (2008).
17. Greg M. Thurber & K. Dane Wittrup Quantitative Spatiotemporal Analysis of Antibody Fragment Diffusion and Endocytic Consumption in Tumor Spheroids. *Cancer Res* **68**, 3334–3341 (2008).
18. Graff, C. P., Chester, K., Begent, R. & Wittrup, K. D. Directed evolution of an anti-carcinoembryonic antigen scFv with a 4-day monovalent dissociation half-time at 37 C. *Protein Engineering, Design & Selection* **17**, 293–304 (2004).
19. Schmidt, M. M., Thurber, G. M. & Wittrup, K. D. Kinetics of anti-carcinoembryonic antigen antibody internalization: effects of affinity, bivalency, and stability. *Cancer Immunology Immunotherapy* **57**, 1879–1890 (2008).
20. Boucher, Y., Baxter, L. T. & Jain, R. K. Interstitial pressure gradients in tissue-isolated and subcutaneous tumors: Implications for therapy. *Cancer Research* **50**, 4478–4484 (1990).
21. Rippe, B. & Haraldsson, B. Fluid and protein fluxes across small and large pores in the microvasculature. Application of two-pore equations. *Acta Physiol. Scand.* **131**, 411–428 (1987).
22. Michael M. Schmidt & K. Dane Wittrup A modeling analysis of the effects of molecular size and binding affinity on tumor targeting. *Mol Cancer Ther* **8**, 2861–2871 (2009).
23. Duane E. Hilmas & Edward L. Gillette Morphometric analyses of the microvasculature of tumors during growth and after X-irradiation. *Cancer* **33**, 103–110 (1974).
24. Laurence T. Baxter & Rakesh K. Jain Transport of fluid and macromolecules in tumors: 3. Role of binding and metabolism. *Microvascular Research* **41**, 5–23
25. Thurber, G. M., Zajic, S. C. & Wittrup, K. D. Theoretic Criteria for Antibody Penetration into Solid Tumors and Micrometastases. *Journal of Nuclear Medicine* **48**, 995–999 (2007).
26. Visvader, J. E. & Lindeman, G. J. Cancer stem cells in solid tumours: accumulating evidence and unresolved questions. *Nature Reviews Cancer* **8**, 755–768 (2008).
27. Kelland, L. R. 'Of mice and men': values and liabilities of the athymic nude mouse model in anticancer drug development. *European Journal of Cancer* **40**, 827–836 (2004).
28. Sharpless, N. E. & DePinho, R. A. The mighty mouse: genetically engineered mouse models in cancer drug development. *Nature Reviews Drug Discovery* **5**, 741–754 (2006).

29. Relationships between drug activity in NCI preclinical in vitro and in vivo models and early clinical trials. *British Journal of Cancer* **84**, (2001).
30. Scott, A. M. *et al.* A Phase I Trial of Humanized Monoclonal Antibody A33 in Patients with Colorectal Carcinoma: Biodistribution, Pharmacokinetics, and Quantitative Tumor Uptake. *Clin Cancer Res* **11**, 4810–4817 (2005).
31. Welt, S. *et al.* Quantitative analysis of antibody localization in human metastatic colon cancer: a phase I study of monoclonal antibody A33. *JCO* **8**, 1894–1906 (1990).
32. Rhoden, J. J. & Wittrup, K. D. Dose dependence of intratumoral perivascular distribution of monoclonal antibodies. *Journal of Pharmaceutical Sciences* **101**, 860–867 (2012).

3. ANTIBODY AFFINITY VS. PENETRATION AND ACCUMULATION

3.1 Introduction

Poor penetration of therapeutic monoclonal antibodies has been well documented in numerous preclinical models¹⁻¹². Furthermore, there is some evidence that poor penetration of these antibodies correlates with decreased therapeutic efficacy^{9,11}. Most therapeutic antibodies which target solid tumors are developed and engineered to have a high affinity for their target antigen. This is thought to be beneficial for antibodies because high affinity antibodies will bind strongly to their targets and remain bound for a longer period. Typical therapeutic antibodies have affinities of single digit nanomolar or below, resulting in a typical dissociation half-life of hours to days.

High affinity antibodies have been shown to exhibit a phenomenon *in vivo* that has been termed the “binding site barrier”¹³. This phenomenon occurs exclusively with high affinity antibodies, and is observed as a perivascular distribution of antibody therapeutics. Tumor cells and tumor antigens near blood vessels are well targeted, but a few cell layers away from blood vessels there are large areas which escape treatment. Over the last two decades, research has shown that the “binding site barrier” is a consequence of many factors regulating the transport of antibodies and other macromolecules into tumors^{2,8,12,14-16}. Antibodies are large molecules, and consequently have slower diffusivity and vascular permeability than smaller molecules. High affinity antibodies are unique in that they bind very tightly to their target antigens, and this in turn means that they remain bound for a long time. In the context of solid tumors, binding to antigen exposes the antibody to antigen-mediated clearance, and ultimately this has been shown to be a major cause of the “binding site barrier” and perivascular distribution^{2,7,8,14}.

Recent research on the binding characteristics of therapeutic antibodies, including the FDA-approved antibodies cetuximab and trastuzumab, has shown that affinity can have a strong influence on the distribution of antibodies in tumor tissue^{10,17}. High affinity antibodies at moderate doses are localized to the perivascular space, while lower affinity antibodies penetrate farther into the tumor tissue. However, as antibody affinity becomes lower, bulk

tumor accumulation can decrease rapidly^{1,2,18}. We seek to study the effect of affinity on tumor penetration and tumor accumulation in a quantitative fashion to determine whether there may be an “optimal” affinity at which high tumor accumulation is achieved while maximizing tumor penetration.

In the tumor space, high affinity antibodies tend to bind the first free antigen that they encounter. Then, because they are high affinity, they will tend to remain bound for hours to days. In contrast, moderate affinity antibodies might bind tumor antigen and remain bound for a therapeutically relevant time period, but then unbind and have the opportunity to diffuse farther into the tumor tissue. In this way, moderate affinity antibodies might sacrifice very high binding in the perivascular region, while increasing penetration into tumor tissue farther from blood vessels. This idea is illustrated schematically in Figure 3.1.

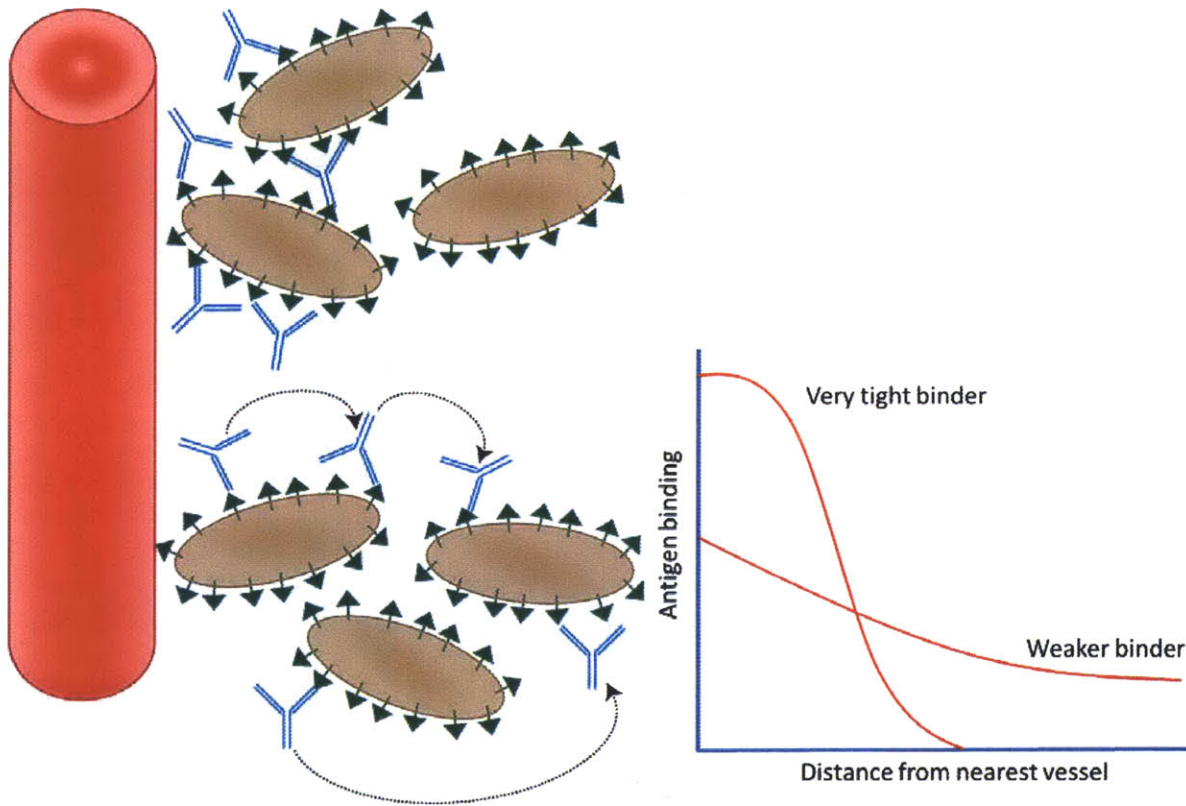


Figure 3.1. Left, schematic illustration of the extravasation and binding of high affinity antibodies (top) and moderate affinity antibodies (bottom). High affinity antibodies bind available antigen as they diffuse from the blood vessel and usually have very long dissociation half lives, so they are often internalized and degraded by the antigen they bind. Moderate affinity antibodies also bind available antigen as they diffuse from the blood vessel, but have shorter dissociation half lives and will more often unbind, continue to diffuse, and bind again until they are eventually endocytosed and degraded. At right, illustration of the antigen binding characteristics that high affinity and moderate affinity antibodies might exhibit around blood vessels. High affinity antibodies are expected to bind more antigen closer to blood vessels, while moderate affinity antibodies are expected to have lowered antigen exposure in the perivascular region while gaining access to tissue located farther from the blood vessels.

3.2 Materials and methods

Reagents

A low-picomolar humanized antibody to carcinoembryonic antigen (CEA), designated sm3e, has previously been engineered and characterized¹⁹. Another high affinity version of this antibody which was isolated earlier in the directed evolution process, termed shMFE, was also used in

this study. Both of these IgGs were used as the backbone to engineer monovalent constructs consisting of the Fc domain and and scFv of the parent antibody, resulting in binding moieties termed ds(Fv)-Fc's measuring approximately 79 kDa in size targeting the same epitope and possessing similar pharmacokinetic properties as the parent IgGs²⁰. In addition, point mutants of shMFE with mutations to single amino acids in the complementarity determining regions were created and screened for changes in binding affinity. Several mutants were chosen for further study based upon their decreased affinity to CEA. All antibodies and antibody fragments were secreted in transiently transfected HEK 293 cells (Invitrogen, Carlsbad, CA), purified by protein A resin (Millipore, Billerica, MA) and buffer exchanged into PBS. Anti-CEA monoclonal antibody M85151a was purchased from Fitzgerald (Acton, MA) and goat anti-rat 546 and goat anti-human Fc antibody secondaries from Invitrogen. Antibody M85151a was labeled with an Alexa Fluor 647 Protein Labeling kit and has been previously determined to be noncompetitive with sm3e²¹. Goat anti-human Fc antibody was labeled with an Alexa Fluor488 Protein Labeling kit.

Animal model

Animal use and care was conducted in full compliance and under approval from the MIT Committee on Animal Care. A CEA-positive human colorectal cancer cell line, LS174T, was used to induce xenograft formation in the flanks of 6-8 week old Ncr nude mice (Taconic, Hudson, NY) by subcutaneous injection of 5×10^6 cancer cells. Tumors were allowed to establish and grow to a size of 5-10 mm, at which point antibody injections were conducted. A 50 μ g (approximately 2 mg/kg) dose of antibody or antibody fragment was injected retroorbitally into tumor bearing nude mice. Mice were sacrificed 24 hours after antibody administration, and tumors were immediately excised and snap frozen in Optimal Cutting Temperature (OCT) medium (Sakura Finetek USA, Torrance, CA) via isopentane over liquid nitrogen. Frozen blocks were stored at -80°C until sectioned by the Koch Institute Histology Core Facility. Frozen blocks were sectioned approximately 1-2 mm into the tumor tissue at a thickness of 8 μ m and stored at -80°C until stained and imaged.

Immunofluorescence protocol

Frozen slides were first air dried for approximately 30 minutes, then tissue samples circled with a PAP pen (Invitrogen, Carlsbad, CA). Tissues were fixed for 10 minutes at room temperature in formalin, then washed 3 times with PBS. Blocking was performed with 5% goat serum (Invitrogen) in PBS for 1 hour at room temp. Primary antibody incubation was 5% goat serum in PBS + 1:100 rat anti-mouse CD31 (BD Pharmingen, San Diego, CA) overnight at 4°C. Slides were then washed three times with PBS, then incubated with PBS+0.1% Tween 20 (Sigma-Aldrich, St. Louis, MO) + 1:200 goat anti-rat 546 (Invitrogen, Carlsbad, CA) + 1:100 M85151a-647 anti-CEA antibody (Fitzgerald, Acton, MA) + 1:100 goat anti-human Fc-488 for 1 hour at room temperature. Slides were washed 4 times with PBS, then mounted in Vectashield + DAPI medium (Vector Labs, Burlingame, CA).

Fluorescence imaging

Slides were imaged using a DeltaVision Spectris microscope (Applied Precision, Issaquah, WA) equipped with a motorized stage and running Softworx software (Applied Precision). Emission and excitation filters were arranged to permit simultaneous 4-color imaging of DAPI, 488, 546, and 647. The paneling feature of Softworx was used to capture the entire tumor section at a resolution of 1.336 $\mu\text{m}/\text{pixel}$ and to stitch together the fields into a single large mosaic image for subsequent analysis.

Unbiased Image Analysis

Rather than introduce potential observer bias by manually selecting individual blood vessels for analysis, images were analyzed as entire tumor sections for features including intervessel distance, antibody penetration from blood vessels, and antigen distribution. The 546 nm (blood vessel) plane was isolated, thresholded to include vessels only, and converted to a binary image using ImageJ (NIH, Bethesda, MD). A Euclidean distance map was created from the vessel binary, and this map was used as a mask to measure average intensity in the antibody (488) and antigen (647) planes as a function of distance from nearest blood vessel by an automated MATLAB (The Mathworks, Natick, MA) computer program. Regions of the tumor revealed to

be necrotic or stromal tissue by examination of H&E staining or by absence of antigen were excluded from the analysis.

Modeling

Antibody extravasation was modeled using an extension of a previously described Krogh cylinder model of the tumor vasculature^{22,23}. A mathematical model, detailed in Appendix A, was solved numerically in MATLAB (MathWorks, Natick, MA) using the method of lines and the built-in numerical ordinary differential equation solver. Simulation results are reported as fractional antigen saturation as defined below:

$$\text{Fractional saturation} = \frac{\text{Antibody bound to tumor antigen} + \text{free antibody in tumor interstitium}}{\text{Total tumor antigen}}$$

All simulation results were reported at a 24 hour time point to match experimental results. The parameters which inform the model were all either directly measured or taken from the literature. In the case of the diffusivity and vascular permeability of the novel monomeric ds(Fv) antibody fragments, these parameters were estimated from fits of literature data describing the effects of molecular size on these parameters¹⁸.

3.3 Results

High affinity anti-CEA antibodies and ds(Fv)-Fc derivatives

High-affinity anti-CEA antibodies and their monovalent derivatives were produced and purified as previously described. The apparent affinities (bivalent for the IgGs, and monovalent for the ds(Fv)s) against CEA expressing LS174T cells were measured, and results are summarized in Figure 3.2.

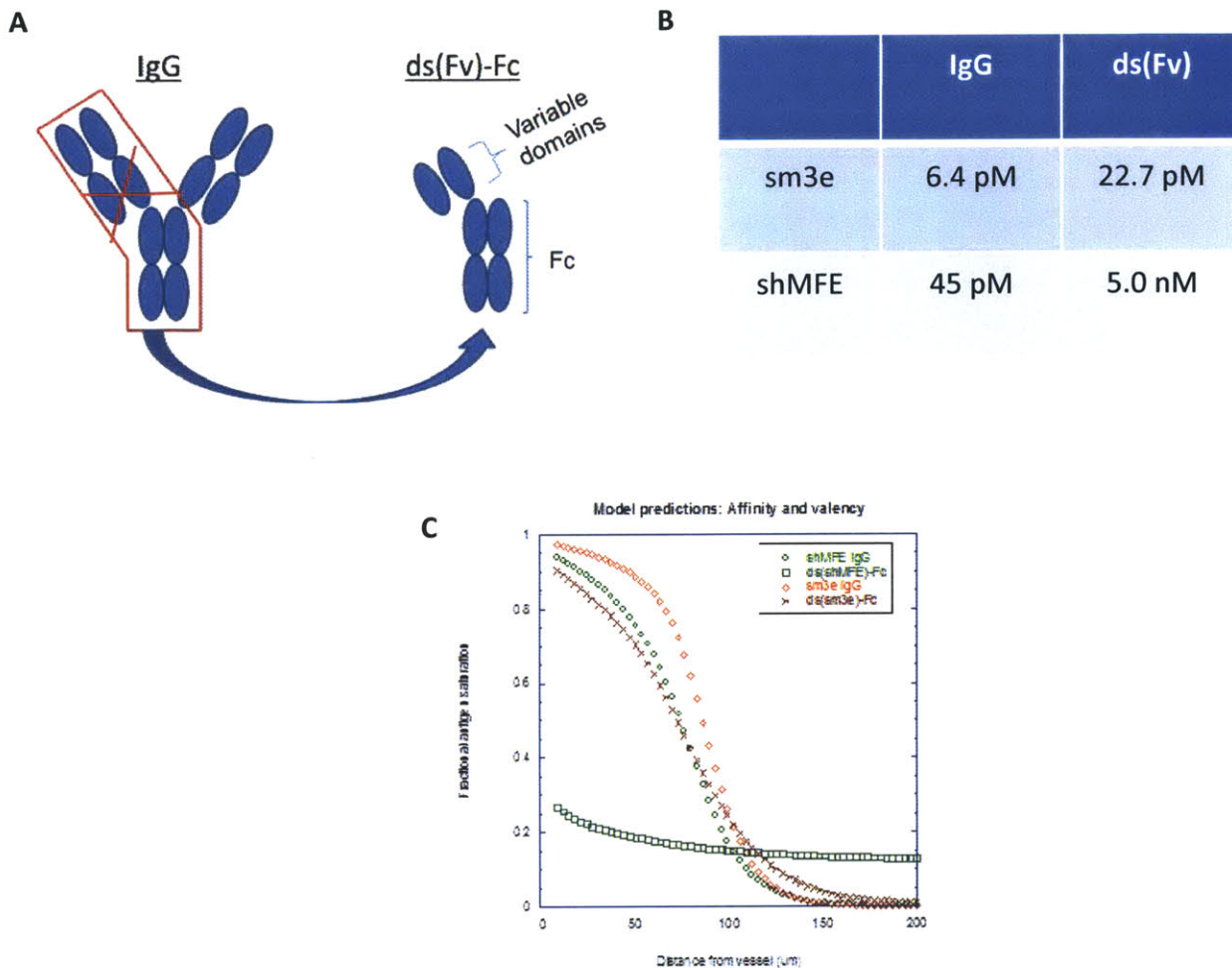


Figure 3.2. A, schematic representation of IgGs (sm3e and shMFE) and the ds(Fv)-Fc constructs derived from them. The ds(Fv)s are approximately half the molecule weight and retain similar blood clearance as the full IgGs due to the presence of intact Fc²¹. B, apparent affinity of anti-CEA IgGs and ds(Fv)s against fixed LS174T cells as measured by flow cytometry. Measured affinities are bivalent for the IgGs and monovalent for their ds(Fv) derivatives. C, simulation predictions for all four constructs based upon measured affinities and other parameters taken from the literature.

These anti-CEA antibodies were injected into LS174T tumor bearing mice at 50 μ g, the tumors excised and stained immunofluorescently as previously described. The full tumor cross sections were imaged at high resolution and representative images scaled identically are shown in Figure 3.3. The high affinity proteins (all except ds(shMFE)-Fc) all exhibit perivascular distributions, with cells near blood vessels well targeted but leaving large areas of the tumor untargeted. The substantially lower affinity ds(shMFE)-Fc has a much different distribution, with much lower intensity, but much more homogeneous, antibody staining. There is little of

the perivascular distribution seen in the case of these tumors. However, the staining is substantially above the background seen in mock (PBS) injected tumors, suggesting that the observed staining derives from the presence of antibody.

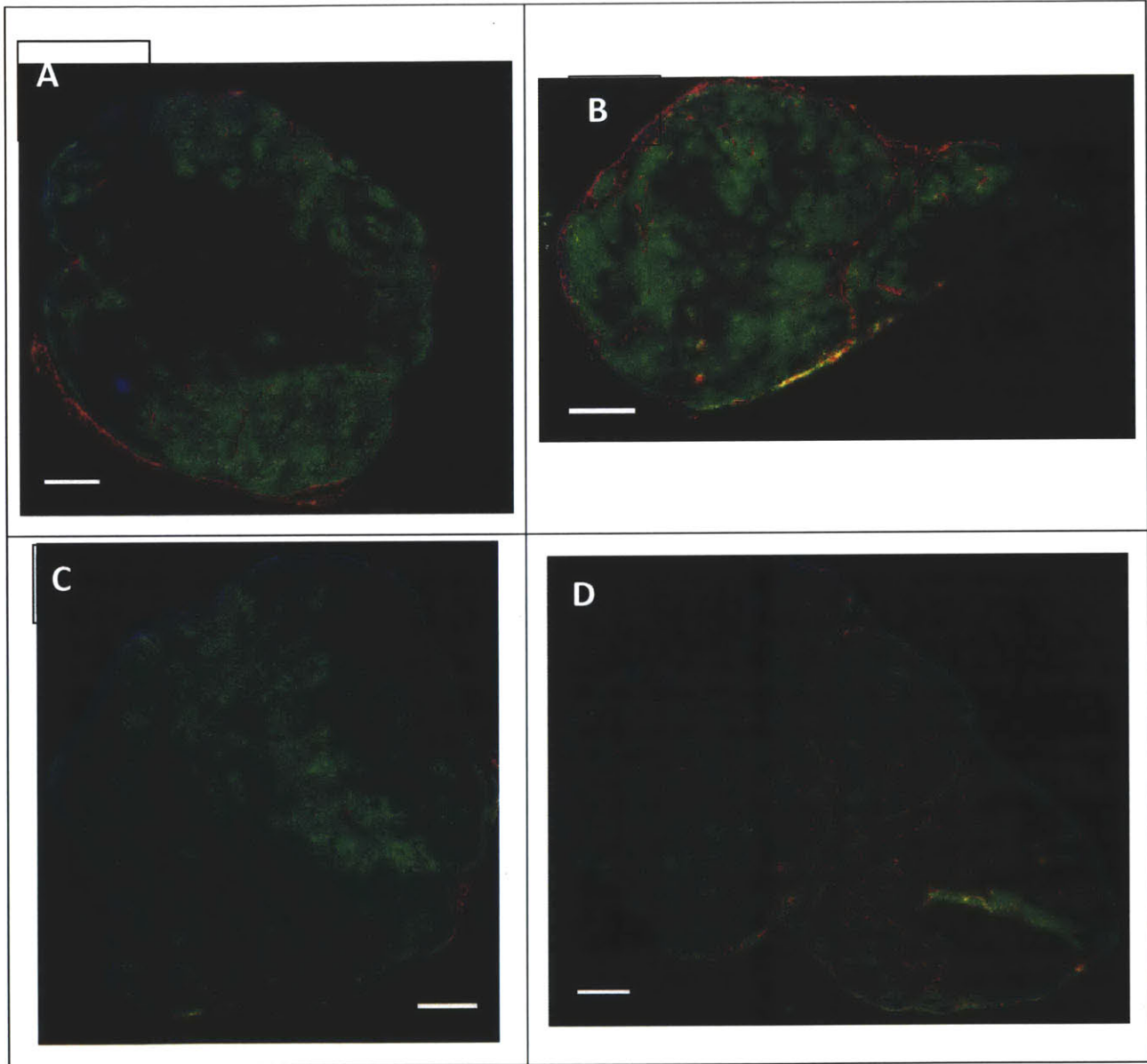


Figure 3.3. A-C, sm3e IgG, ds(sm3e)-Fc, and shMFE IgG representative immunofluorescent images, respectively. D, ds(shMFE)-Fc representative immunofluorescent image. All images were scaled identically, and all scale bars are 1 mm. Large areas of unstained tissue in the interior regions of panels A and C are necrotic regions as evidenced by H&E. Not shown for clarity is the antigen stain, which was expressed uniformly throughout the viable tissue.

The immunofluorescent images were processed as described previously to quantify the distribution of the anti-CEA antibodies and constructs. The results of the unbiased image analysis are shown in Figure 3.4. The three high affinity proteins, each of which possessed an apparent K_d *in vitro* of less than 50 pM, are statistically indistinguishable from one another and indicate a high level of antibody binding near blood vessels. The ds(shMFE)-Fc construct, in contrast, is markedly different and shows a uniformly much lower degree of antibody binding, consistent with the immunofluorescence imaging (Figure 3.3). To a distance of approximately 120 μm , beyond which there exists very little viable tissue (data not shown), all of the constructs show a fairly homogeneous distribution with little dependence on distance from nearest blood vessel.

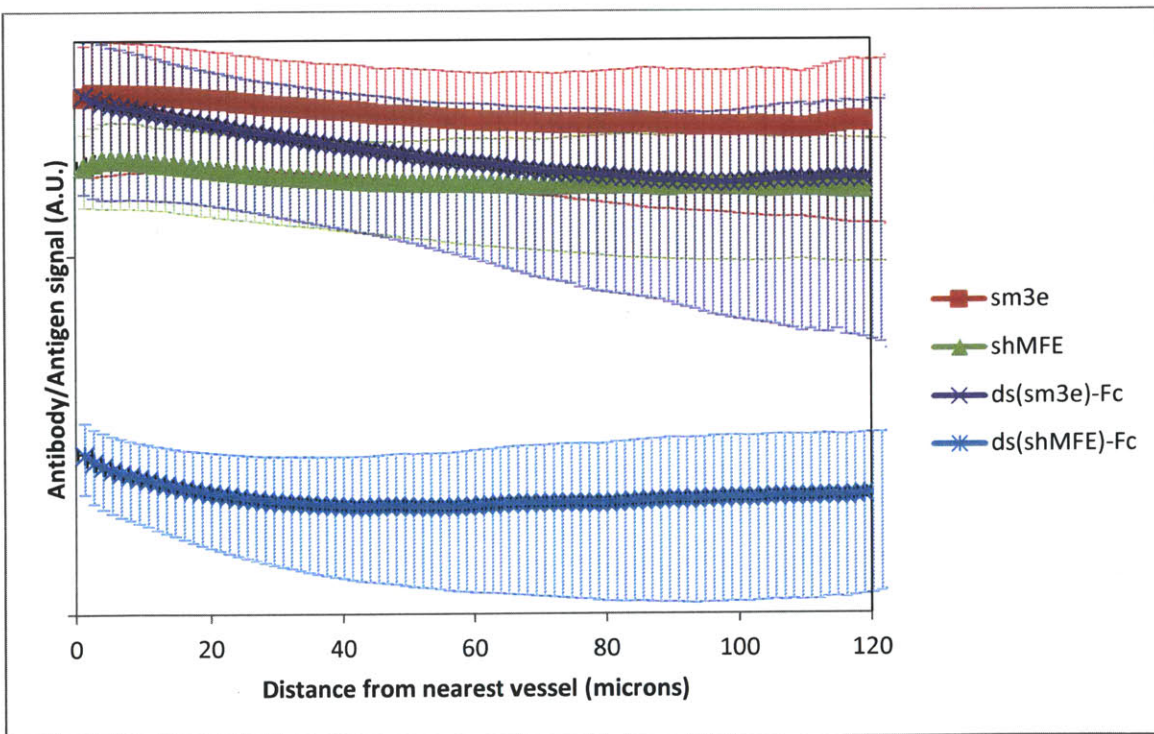


Figure 3.4. Whole-section automated image analysis results. Antibody and antigen fluorescence signals are quantitated and the antibody signal normalized to antigen signal. Error bars are \pm S.D of analysis of 3-5 tumors per construct.

Since there is very little viable tissue far from blood vessels, the data from whole tumor sections is typically heavily weighted toward tissue near blood vessels. To better analyze

antibody penetration into tissue far from blood vessels, individual blood vessels isolated from regions of low vascularity were found and analyzed to examine the penetration of the various antibody constructs into the viable tissue surrounding these vessels. Approximately 5-8 such vessels were identified and analyzed in 3-4 tumor sections per antibody construct, and the results of the analysis of antibody distribution around these isolated vessels is shown in Figure 3.5. As indicated by the error bars, the distribution around blood vessels is highly variable. However, just as in the case of the whole tumor sections, the high affinity antibodies are indistinguishable from one another in their distribution and intensity, while the moderate affinity ds(shMFE)-Fc is significantly lower intensity and more homogenous in its distribution.

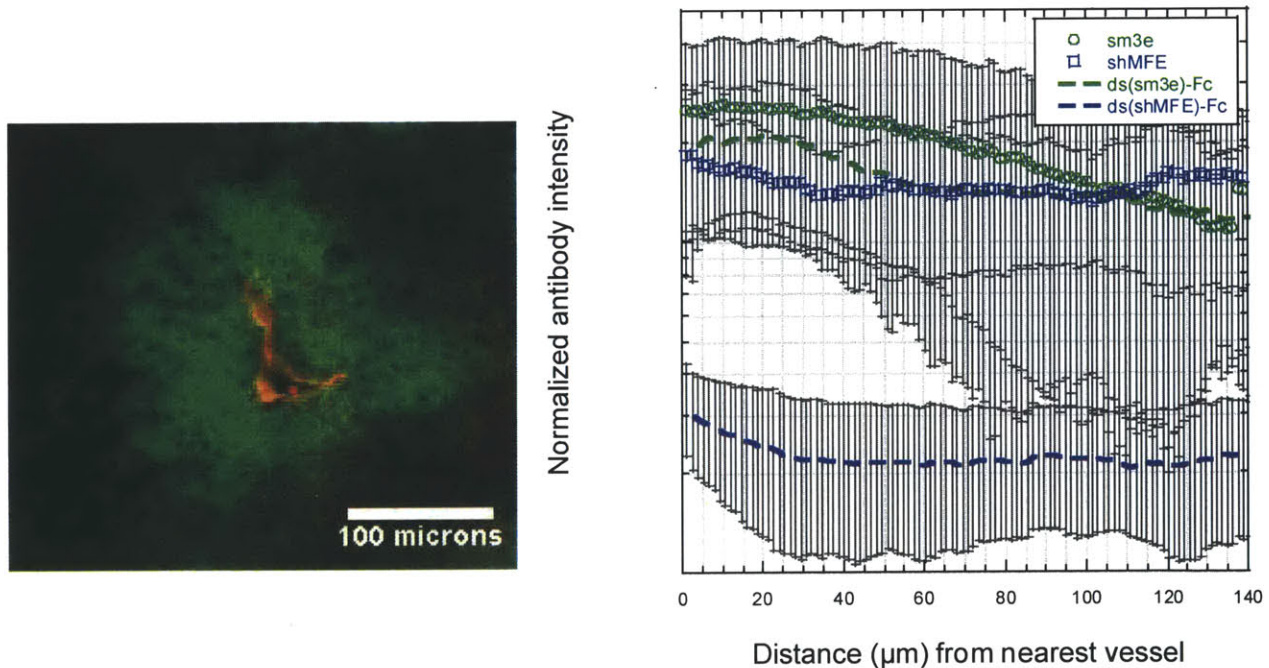


Figure 3.5. Left, high resolution image of isolated blood vessel surrounded by viable tumor tissue. Red denotes blood vessels (CD31) and green anti-CEA antibody. Right, unbiased image analysis to quantitate antibody distribution around isolated vessels. Error bars are \pm S.D. and antibody signal is normalized to antigen signal.

As a final method to analyze the distribution of these four antibody constructs, we sought to evaluate the perceived distribution in whole tumor sections as rated by impartial and blinded

human observers. Observers were asked to rate their perception of the heterogeneity or homogeneity of antibody distribution on a five point scale. The observers were presented with images processed to remove stromal and necrotic tissue and were not told in advance of the purpose of the analysis. They were allowed to adjust the scaling of the antibody channel to better examine the images. Results are shown in Figure 3.6. As in the previous analyses, observers were unable to distinguish between the high affinity antibodies and rated them all highly heterogeneous at approximately a 4 on a 5 point scale. They rated the moderate affinity antibody differently and much more homogeneously, at approximately a 2 on a 5 point scale.

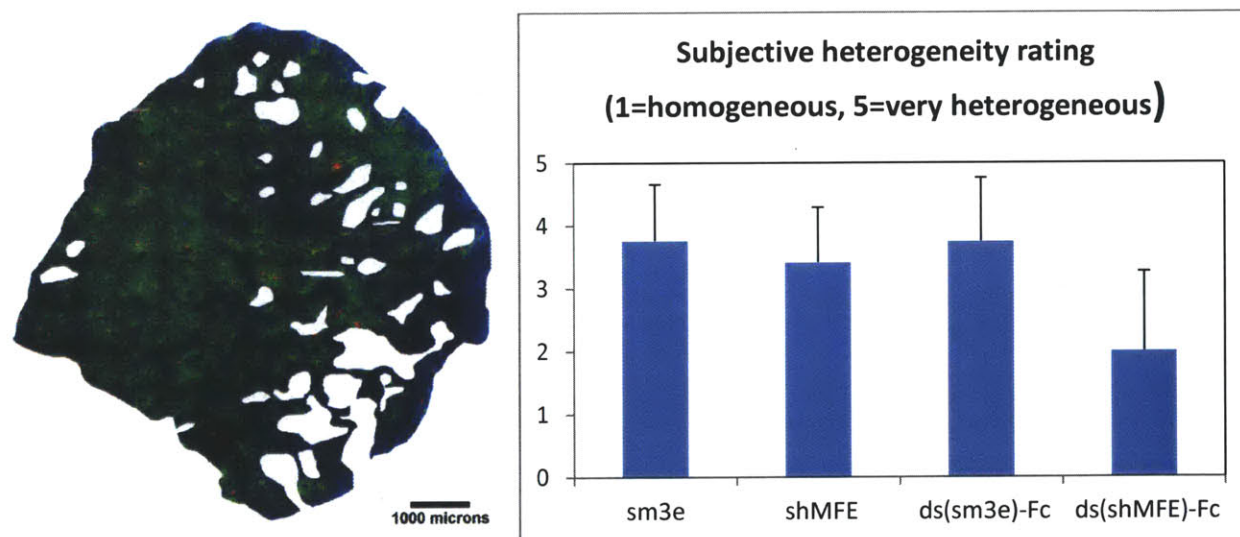


Figure 3.6. Left, representative processed image shown to blinded and impartial observers for subjective heterogeneity rating. Observers were asked to rate heterogeneity of the antibody signal (green) on a five point scale. Right, results from n=4 observers. Error bars are \pm S.D.

shMFE affinity series

To better study the range of antibody affinities in the “moderate” range of single and double digit nanomolar, a set of point mutants of the shMFE high affinity (~ 50 pM) antibody was generated and tested for binding to CEA expressing cells, resulting in the selection of a set of anti-CEA binders with affinities spanning over three orders of magnitude (Table 3.1).

Importantly, all five antibodies are full length human IgG1 isotype antibodies, and all have a

common heritage through the affinity maturation of parent antibody MFE^{19,24}. As a result, they are expected to be very similar molecules biochemically and also behave similar in their *in vivo* pharmacokinetics.

α-CEA antibody affinity series derived from common parent	
Sm3e	~10 pM
shMFE	~50 pM
shMFE-F	~2 nM
shMFE-L	~20 nM
shMFE-T	~30 nM

Table 3.1. Apparent (bivalent) affinities of anti-CEA antibodies on CEA-expressing fixed tumor cells as measured by flow cytometry. Sm3e is an affinity-matured derivative of shMFE, and shMFE was subjected to selective point mutations in the complementarity determining region to generate moderate affinity shMFE-F, -L, and -T antibodies.

This affinity series of antibodies was injected into nude mice bearing LS174T tumors, allowed to circulate for 24 hours, and the tumor excised, sectioned, and stained for immunofluorescence as previously described. Whole tumor sections were then imaged at high resolution, stitched together into a large mosaic image, and processed using the unbiased image analysis and quantitation tools described earlier. Representative immunofluorescent images are shown in Figure 3.7.

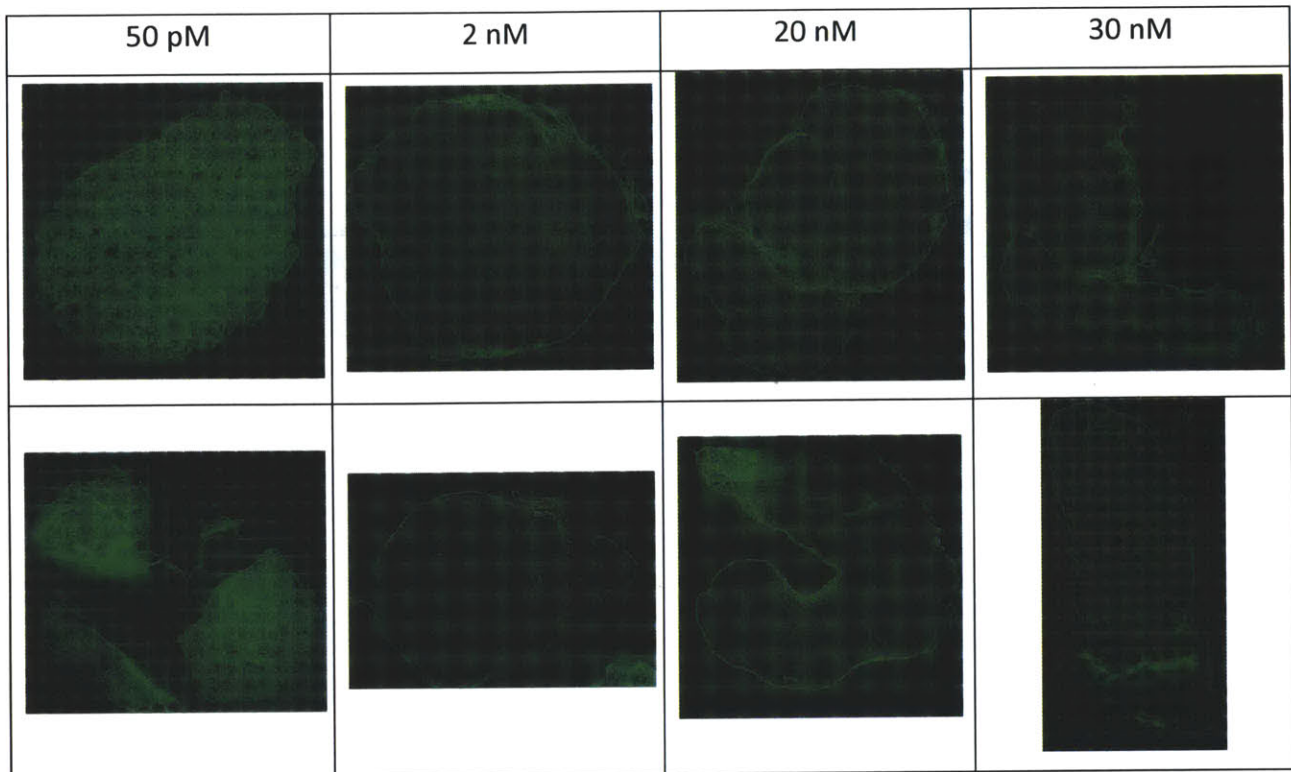


Figure 3.7. Representative immunofluorescent images of tumor sections dosed with shMFE or various lower affinity point mutants of shMFE. For clarity, only antibody signal is shown (green). Cross-hatching is an artifact resulting from the microscopy process. All sections measure 5-10 mm across.

As antibody signals were much lower than anticipated for the shMFE point mutants, a biodistribution study was conducted by collaborators at Beth Israel Deaconess Medical Center (BIDMC). All five anti-CEA antibodies were labeled with a radioactive marker, dosed into tumor bearing mice, and the organs removed 24 hours following antibody dosing for determination of the antibody signal in each organ. These data are presented in Figure 3.8. By comparing the antigen positive (LS174T) and antigen negative (c6) tumors, it is possible to determine the signal that results from specific accumulation due to antigen binding and the amount that accumulates nonspecifically. The subnanomolar binders, sm3e and shMFE, both show strong accumulation in the antigen-positive tumor over the antigen-negative tumor, indicating binding-mediated retention and accumulation. In contrast, all three lower affinity shMFE point mutants show approximately equal binding in the antigen-positive and antigen-negative tumors, indicating that binding is unlikely to be a major contributor to enhancing tumor accumulation. This agrees with the immunofluorescence data, which was also unable to detect

significant binding in the tumor in the case of the shMFE point mutants, but showed strong specific binding of shMFE and sm3e.

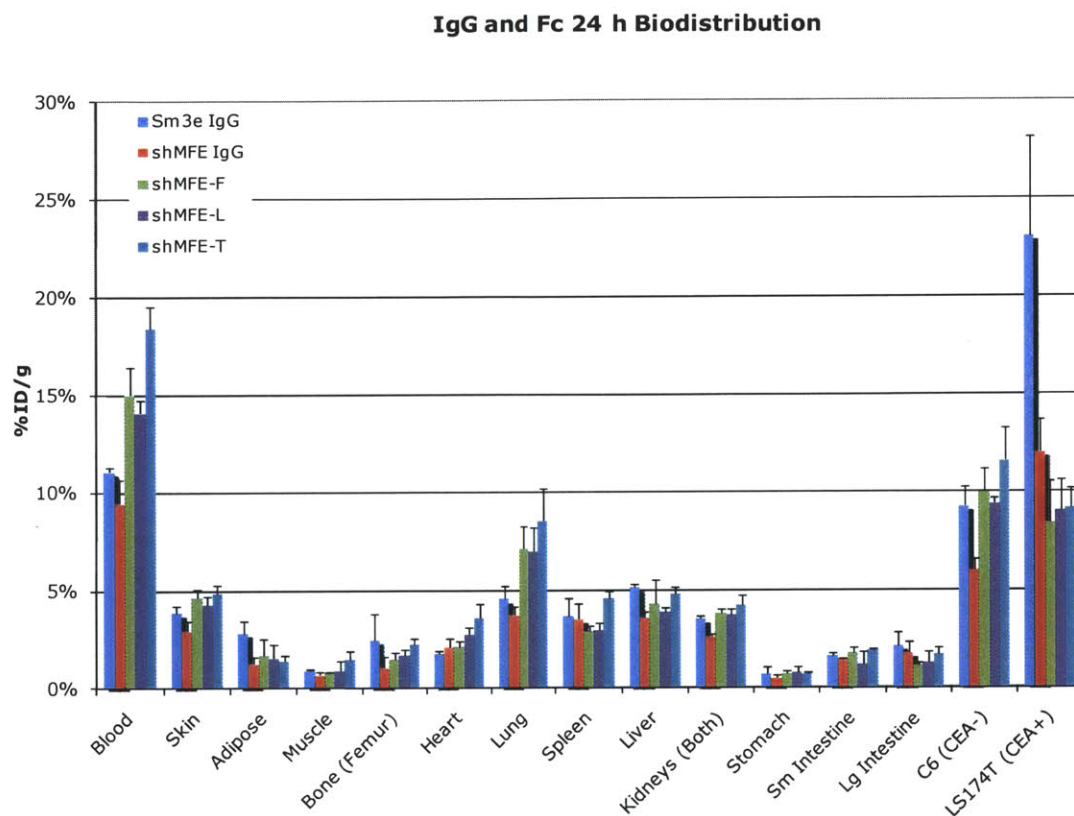


Figure 3.8. Biodistribution data, courtesy of Kelly Orcutt and taken at BIDMC, shows that subnanomolar affinity binders accumulate specifically in antigen-positive tumors versus antigen-negative tumors at the 24 h time point. Weaker binders show equivalent accumulation regardless of the presence or absence of antigen, indicating that antigen-mediated antibody accumulation is not a major contributor with these antibodies.

3.4 Discussion

Two separate experiments were conducted, both using antibodies or antibody fragments directed against CEA. In both cases, subnanomolar affinity binders exhibited quantitatively and qualitatively different microdistribution and tumor accumulation characteristics than did nanomolar or weaker affinity binders. High affinity antibodies, such as sm3e (~10 pM) and shMFE (~50 pM) both showed perivascular distribution which is characteristic of high affinity antibodies given at subsaturating doses^{1,7,25}. These high affinity antibodies were all less than

100 pM binding affinity, and experimentally were indistinguishable from one another. This is not surprising, as high affinity antibodies in this range of K_d values are predicted to have very similar perivascular distributions (Figure 3.2C). Examination of the experimental data in Figure 3.4 also shows that whole tumor section microdistribution data can be heterogeneous, as could be expected given the heterogeneity inherent in the tumor microenvironment.

The moderate affinity antibodies were expected to show a qualitatively and quantitatively different distribution in the tumor (Figure 3.2). These antibodies, because they are more likely at any given time to unbind antigen and be free to diffuse through tumor tissue, were expected to penetrate farther into the tumor tissue at the expense of maximizing antigen binding in regions proximal to blood vessels. Experimentally, the moderate affinity (2-30 nM) antibodies showed a much more homogeneous distribution through the tissue and little dependence on distance from blood vessels. Mathematical modeling (Figure 3.2) suggested this general trend, but seems to have underestimated the degree to which the phenomenon occurs. Extending the modeling to weaker affinity antibodies offers a more complete picture as depicted in Figure 3.9. From Figure 3.9A, we see that antibodies around 1-10 nM are predicted to lose a great deal of their perivascular distribution and transition to a more homogeneous distribution without a strong dependence on distance from blood vessels. At very low affinities, there appears to be no such dependence and much of the antibody in the tumor is retained nonspecifically as free (unbound) antibody. This appears to be the situation encountered with the sHMFE point mutants, which at moderate affinities lost perivascular dependence and showed little to no antigen-mediated retention in the tumor (Figure 3.8). In Figure 3.9B, we see the effect of antibody affinity and desired receptor occupancy on the predicted penetration distance. For high receptor occupancy, it is necessary to have a high affinity antibody that remains bound to cells near the blood vessel that are bound as the antibody extravasates. However, as receptor occupancy decreases, distance penetrated into the tumor increases dramatically. It can also be seen that there may be some benefit to moderate affinity in terms of penetration distance. The 0.1 fractional receptor occupancy curve shows enhanced penetration in the single digit nanomolar range relative to any other affinity. However, it should be noted for all occupancy levels that the decrease in penetration distance as affinity

decreases past a certain point is extremely rapid, and so slightly weaker than expected affinities can result in a complete failure to achieve a desired receptor occupancy.

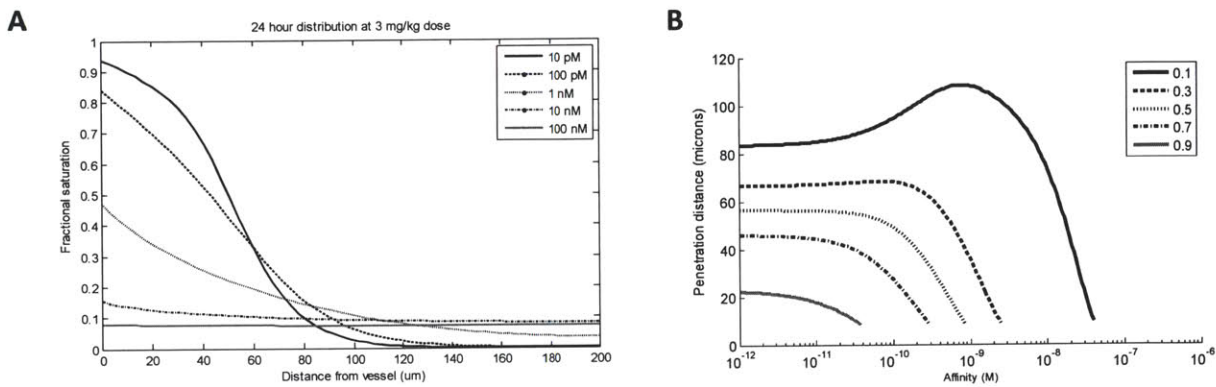


Figure 3.9. A, modeling results of penetration from blood vessels as a function of antibody affinity. Simulation results span from 10 pM to 100 nM, a range which includes the vast majority of antibodies. B, predicted penetration distance of antibodies as a function of affinity and receptor occupancy. Lines represent receptor occupancy (fraction of available antigen bound by antibody).

As can be seen in Figure 3.9, modeling predicts that moderate affinity antibodies penetrate farther into the tumor. Experimentally, this phenomenon was rarely observed, although it was seen, for example as shown in Figure 3.10. Both modeling and experiment agree that any enhanced penetration of moderate affinity antibodies would only be seen at relatively far distances from blood vessels—approximately 100 μm or more. In practice, very little viable tissue exists so far from blood vessels, largely because the diffusion limit of oxygen through tissue is thought to be just beyond this limit²⁶. However, there is evidence to suggest that these isolated regions may harbor tumor stem cells, which are known to be resistant to hypoxia and are able to regenerate the tumor if not killed themselves^{27,28}. In an attempt to examine these regions, isolated vessels supplying tissue farther than 100 μm were identified and analyzed for their perivascular distribution characteristics (Figure 3.5). However, there were few differences found among the high affinity antibodies, and the moderate affinity antibodies distributed well but with relatively low binding.

The predicted distributions for the moderate affinity antibodies (Figures 3.2 and 3.9) were not seen experimentally. Instead, a distribution more similar to a much weaker affinity antibody,

such as a 100 nM affinity antibody (Figure 3.9) was observed. The cause of this may be that the affinity of all antibody constructs was measured *in vitro* on fixed cells. This environment is much different than the tumor interstitium in which the antibodies were binding in the *in vivo* experiments, and it seems reasonable that the apparent affinity might be lower in such a complex environment with many other competing molecules. Therefore, an antibody measured at a relatively high affinity *in vitro* might behave as a lower affinity antibody *in vivo*.

Although enhanced penetration at distances far from tumor vessels was observed in some isolated instances (Figure 3.10), generally the distribution was split between high affinity (100 pM or better) antibodies and lower affinity (single digit nanomolar or higher) antibodies, each of which were indistinguishable from one another. Little evidence of intermediate behavior, i.e. of somewhat enhanced penetration while retaining a high degree of antigen binding, was observed. Insights into the cause of this behavior come from mathematical modeling and data from the literature (Figure 3.10). This analysis suggests that the “window” for enhanced tumor penetration spans only a small affinity range of less than an order of magnitude. In this window, penetration can be enhanced by a distance of approximately a cell layer or slightly more. However, as shown in Figure 3.10, this window of enhanced penetration is also very close to the “cliff” of greatly decreased tumor accumulation. So, although there are marginal potential gains to be made in a certain moderate affinity range, this range is quite narrow. Moreover, this range is positioned on the edge of a “cliff” beyond which accumulation of antibody in the tumor decreases dramatically.

This observation has significant implications for therapeutic applications. Depending upon the mechanism of action, high antigen saturation may be important or critical—for example, a monoclonal antibody which exerts an effect by blocking ligand binding. Other mechanisms may require only very small amounts of antigen binding, such as very potent immunotoxins or some radioimmunotherapies. These different mechanisms of action call for substantially different criteria for tumor penetration and fractional antigen saturation. This research may have implications for the development of antibody-based therapeutics in many different indications and disease types.

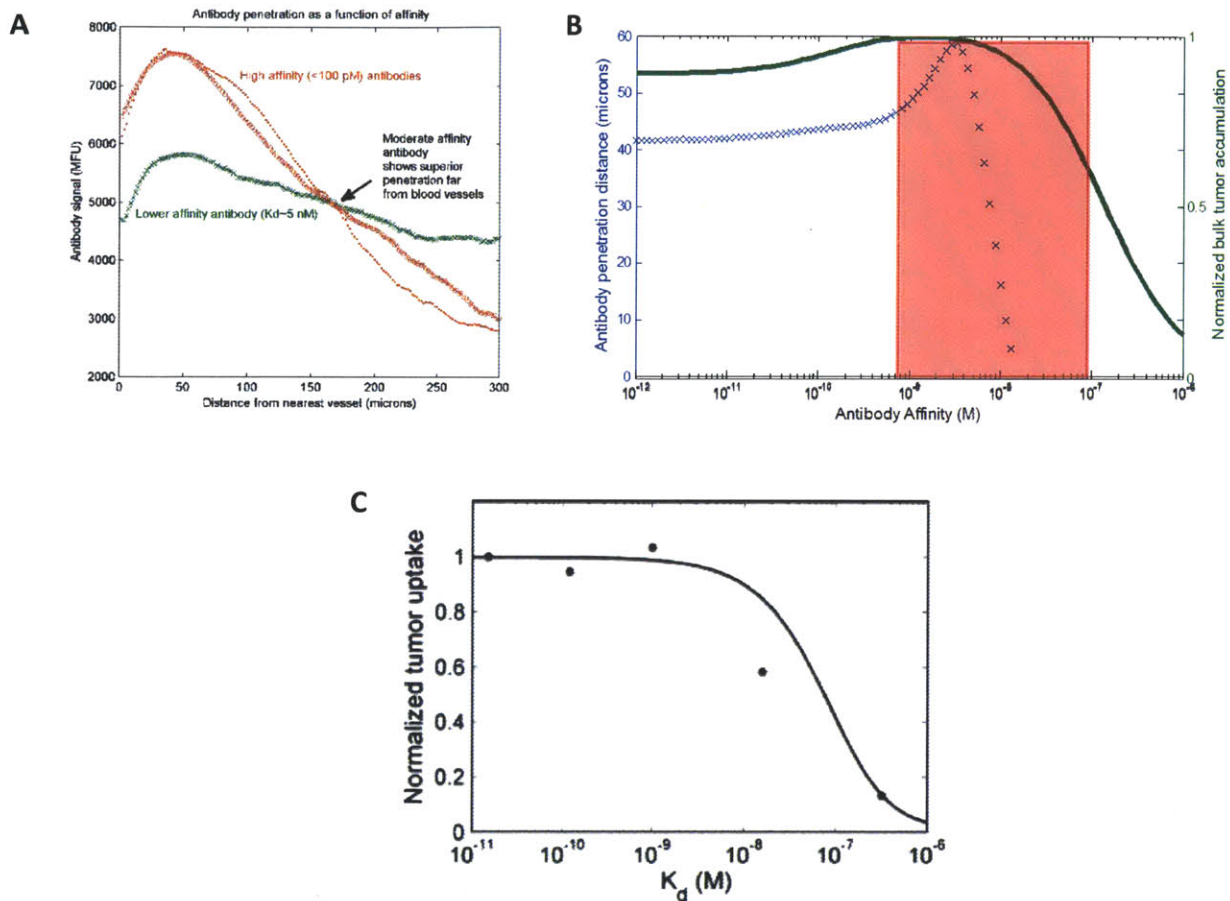


Figure 3.10. A, example of one experiment in which a moderate affinity ($\sim 5\text{ nM } K_d$, shown in green) antibody was shown to penetrate farther into tumor tissue than high affinity antibodies. Note that the moderate affinity antibody has a lower signal at the blood vessel, but higher signal far from the blood vessel. B, plot of antibody penetration (defined as the maximum distance at which 50% receptor occupancy is retained at 24 hours post-injection) and bulk uptake of antibody (normalized to maximum uptake at 24 hours) vs. antibody affinity. Shaded red is the zone of moderate affinity in which enhanced tumor penetration may be achieved. Note that this region is very close to a rapid decrease in bulk uptake with weakening affinity. C, plot adapted from ¹⁸ and showing theoretical (solid line) and data from the literature (points) illustrating the decrease in tumor uptake of antibodies with decreasing affinity. These data and modeling agree well with panel B.

3.5 References

1. Adams, G. P. *et al.* High affinity restricts the localization and tumor penetration of single-chain Fv antibody molecules. *Cancer Research* **61**, 4750–4755 (2001).
2. Rudnick, S. I. *et al.* Influence of Affinity and Antigen Internalization on the Uptake and Penetration of Anti-HER2 Antibodies in Solid Tumors. *Cancer Research* **71**, 2250–2259 (2011).
3. Rudnick, S. I. & Adams, G. P. Affinity and avidity in antibody-based tumor targeting. *Cancer biotherapy and radiopharmaceuticals* **24**, 155–161 (2009).
4. Emir, E. E. *et al.* Predicting response to radioimmunotherapy from the tumor microenvironment of colorectal carcinomas. *Cancer Research* **67**, 11896–11905 (2007).
5. Fidarova, E. F. *et al.* Microdistribution of Targeted, Fluorescently Labeled Anti-Carcinoembryonic Antigen Antibody in Metastatic Colorectal Cancer: Implications for Radioimmunotherapy. *Clinical Cancer Research* **14**, 2639–2646 (2008).
6. Flynn, A. A., Boxer, G. M., Begent, R. H. J. & Pedley, R. B. Relationship between tumour morphology, antigen and antibody distribution measured by fusion of digital phosphor and photographic images. *Cancer Immunology Immunotherapy* **50**, 77–81 (2001).
7. Rhoden, J. J. & Wittrup, K. D. Dose dependence of intratumoral perivascular distribution of monoclonal antibodies. *Journal of Pharmaceutical Sciences* **101**, 860–867 (2012).
8. Ackerman, M. E., Pawlowski, D. & Wittrup, K. D. Effect of antigen turnover rate and expression level on antibody penetration into tumor spheroids. *Molecular Cancer Therapeutics* **7**, 2233–2240 (2008).
9. Minchinton, A. I. & Tannock, I. F. Drug penetration in solid tumours. *Nature Reviews Cancer* **6**, 583–592 (2006).
10. Baker, J. H. E. *et al.* Direct visualization of heterogeneous extravascular distribution of trastuzumab in human epidermal growth factor receptor type 2 overexpressing xenografts. *Clinical Cancer Research* **14**, 2171–2179 (2008).
11. Freeman, D. J. *et al.* Tumor penetration and epidermal growth factor receptor saturation by panitumumab correlate with antitumor activity in a preclinical model of human cancer. *Molecular Cancer* **11**, 47 (2012).
12. Baxter, L. T. & Jain, R. K. Transport of Fluid and Macromolecules in Tumors IV: A Microscopic Model of the Perivascular Distribution. *Microvascular Research* 252–272 (1991).
13. Fujimori, K., Covell, D., Fletcher, J. & Weinstein, J. A Modeling Analysis of Monoclonal-Antibody Percolation Through Tumors - a Binding-Site Barrier. *J. Nucl. Med.* **31**, 1191–1198 (1990).

14. Thurber, G. M., Schmidt, M. & Wittrup, K. D. Antibody tumor penetration: Transport opposed by systemic and antigen-mediated clearance. *Advanced Drug Delivery Reviews* (2008).
15. Wittrup, K. D., Thurber, G. M., Schmidt, M. M. & Rhoden, J. J. Practical theoretic guidance for the design of tumor-targeting agents. *Meth. Enzymol.* **503**, 255–268 (2012).
16. Greg M. Thurber & K. Dane Wittrup Quantitative Spatiotemporal Analysis of Antibody Fragment Diffusion and Endocytic Consumption in Tumor Spheroids. *Cancer Res* **68**, 3334–3341 (2008).
17. Carol M Lee & Ian F Tannock The distribution of the therapeutic monoclonal antibodies cetuximab and trastuzumab within solid tumors. *BMC Cancer* **10**, (2010).
18. Michael M. Schmidt & K. Dane Wittrup A modeling analysis of the effects of molecular size and binding affinity on tumor targeting. *Mol Cancer Ther* **8**, 2861–2871 (2009).
19. Graff, C. P., Chester, K., Begent, R. & Wittrup, K. D. Directed evolution of an anti-carcinoembryonic antigen scFv with a 4-day monovalent dissociation half-time at 37 C. *Protein Engineering, Design & Selection* **17**, 293–304 (2004).
20. Schmidt, M. M. Engineering antibodies for improved targeting of solid tumors. (2009).at <<http://dspace.mit.edu/handle/1721.1/61239>>
21. Schmidt, M. M., Thurber, G. M. & Wittrup, K. D. Kinetics of anti-carcinoembryonic antigen antibody internalization: effects of affinity, bivalency, and stability. *Cancer Immunology Immunotherapy* **57**, 1879–1890 (2008).
22. Thurber, G. M., Zajic, S. C. & Wittrup, K. D. Theoretic Criteria for Antibody Penetration into Solid Tumors and Micrometastases. *Journal of Nuclear Medicine* **48**, 995–999 (2007).
23. Krogh, A. The number and distribution of capillaries in muscles with calculations of the oxygen pressure head necessary for supplying the tissue. *J Physiol* **52**, 409–415 (1919).
24. Boehm, M. K. & Perkins, S. J. Structural models for carcinoembryonic antigen and its complex with the single-chain Fv antibody molecule MFE23. *FEBS Letters* **475**, 11–16 (2000).
25. Zuckier, L. S. *et al.* Influence of affinity and antigen density on antibody localization in a modifiable tumor targeting model. *Cancer Research* **60**, 7008–2013 (2000).
26. Helmlinger, G., Yuan, F., Dellian, M. & Jain, R. K. Interstitial pH and pO₂ gradients in solid tumors in vivo: High-resolution measurements reveal a lack of correlation. *Nature Medicine* **3**, 177–182 (1997).
27. Magee, J. A., Piskounova, E. & Morrison, S. J. Cancer Stem Cells: Impact, Heterogeneity, and Uncertainty. *Cancer Cell* **21**, 283–296 (2012).
28. Visvader, J. E. & Lindeman, G. J. Cancer stem cells in solid tumours: accumulating evidence and unresolved questions. *Nature Reviews Cancer* **8**, 755–768 (2008).

4. ANTIBODY DOSING STRATEGIES TO IMPROVE TUMOR PENETRATION

4.1 Introduction

Poor penetration of monoclonal antibodies into tumor tissue in preclinical animal models of cancer has been well documented for many antibodies, antigens, and tumor types¹⁻¹¹. The studies which have shown poor penetration into solid tumors typically consist of a single intravenous or intraperitoneal injection of the antibody of interest, followed by a waiting period of hours to days to allow the antibody to circulate and extravasate, and finally evaluation of the distribution of the antibody at the desired time point. In the clinic, however, antibody treatments are typically not administered as a single bolus dose. Instead, multiple infusions are given spaced out over weeks to months. This strategy has been necessary for many cancer treatments, most notably chemotherapy, because the therapeutic is itself toxic and so periods of time between doses are necessary to allow healthy tissue to recover. Antibodies similarly often have some degree of toxicity *in vivo* and are therefore administered in multiple doses separated by waiting periods to allow healthy tissue to recover.

Clinical studies of doses and dosing strategies for therapeutic monoclonal antibodies illustrate this dosing strategy. For instance, a phase II clinical trial of FDA-approved monoclonal antibody cetuximab in patients with colorectal cancer involved weekly i.v. infusions of antibody¹². A phase III trial of trastuzumab, another FDA approved antibody, for metastatic breast cancer involved 6 cycles of weekly i.v. infusions of a the drug¹³.

The *in vivo* tissue distribution of multiple doses of antibodies in dosing strategies similar to the clinical situation has not been well studied. These strategies raise new issues that are not important for single-dose studies, namely in that the therapeutic antibodies are likely to exert a pharmacodynamic effect on the tumor in these studies. Many therapeutic antibodies have been shown to delay or shrink tumors in animal models, and others have been shown to alter antigen expression or catabolism^{2,14,15}. Antigen expression and turnover rate have been shown to be important parameters in determining the penetration and catabolism of antibodies in tumors^{5,6,10,16}. The effects of tumor cell killing also complicate the picture, adding additional

rates to consider in the rate at which tumor cells are killed and the rate in which tumors are repopulated and grow.

One possible outcome of serial dosing of therapeutic antibodies is to progressively penetrate farther into the tumor, killing tumor cells layer-by-layer with successive doses. This idea is illustrated schematically in Figure 4.1. This hypothesis seems likely to occur if the rate of antibody-mediated cell killing is more rapid than the rate of tumor cell growth. However, if tumor cells grow more rapidly than they can be killed, then this strategy may succeed in slowing the growth of the tumor, but will not shrink or eliminate the tumor. Further complicating matters is the possibility of other physiological changes brought about by multiple dosing strategies, such as dead tumor cell “debris” impeding transport in tumors, or the possibility of developing resistance to therapy over the longer time periods of these dosing strategies¹⁷⁻¹⁹.

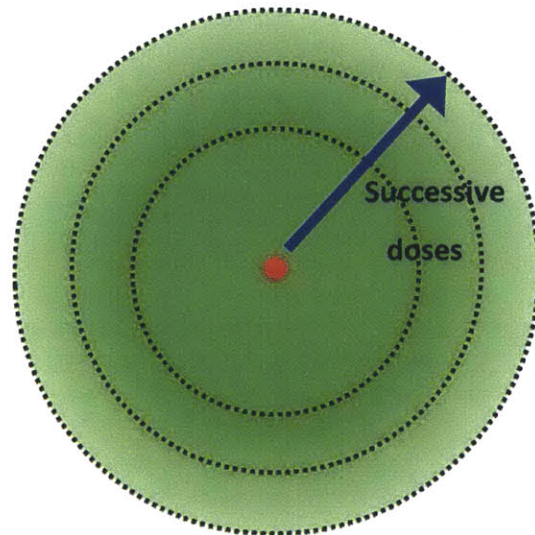


Figure 4.1. Schematic illustration of a multiple dosing strategy on the distribution of a therapeutic antibody around a blood vessel. The red circle in the center represents a tumor vessel, and the green region surrounding it represents the region penetrated by a therapeutic antibody. Successive doses penetrate farther and farther from the vessel as perivascular tumor cells are killed off, as represented by the concentric dashed circles.

4.2 Materials and methods

Reagents

A trispecific EGFR binding protein based upon the backbone of antibody 225, which is in clinical use as cetuximab, has been previously generated and characterized and was termed HN-D/LC-A¹⁴. This antibody as well as parental 225 antibody were secreted in transiently transfected HEK 293 cells (Invitrogen, Carlsbad, CA), purified by protein A resin (Millipore, Billerica, MA) and buffer exchanged into PBS. Goat anti-rat 546 and goat anti-human Fc antibody secondary antibodies were purchased from Invitrogen (Carlsbad, CA). The anti-human Fc secondary antibody was labeled with an Alexa Fluor 488 Protein Labeling kit (Invitrogen). Aliquots of HN-D/LC-A were labeled with Alexa Fluor 488 or 647 protein labeling kits.

Animal model

Animal use and care was conducted in full compliance and under approval from the MIT Committee on Animal Care. An EGFR-positive human colorectal cancer cell line, HCT-116, was used to induce xenograft formation in the flanks of 6-8 week old Ncr nude mice (Taconic, Hudson, NY) by subcutaneous injection of 5×10^6 cancer cells. Tumors were allowed to establish and grow for one week, at which point antibody injections were conducted at schedules and doses detailed in the Results section. Tumors were measured daily and volume calculated as $L^2 \times W/2$. All injections were conducted retroorbitally, alternating eyes between injections, except in the case of daily injections which were rotated between the eyes and each of the two veins in the tail (four sites total). The penultimate antibody injection was labeled with Alexa Fluor 647, and the final antibody injection was labeled with Alexa Fluor 488. Mice were sacrificed 24 hours after the final antibody administration, and tumors were immediately excised, cut in half with a razor blade, and one half snap frozen in Optimal Cutting Temperature (OCT) medium (Sakura Finetek USA, Torrance, CA) via isopentane over liquid nitrogen. Frozen blocks were stored at -80°C until sectioned by the Koch Institute Histology Core Facility. Frozen blocks were sectioned approximately 1-2 mm into the tumor tissue at a thickness of $8 \mu\text{m}$ and stored at -80°C until stained and imaged.

Tumor dissociation and flow cytometry

One half of each freshly excised tumor was finely diced with a razor. The diced tumor was digested in 2 ml digest medium consisting of 1 mg/ml collagenase A (Roche, Indianapolis, IN) and 105 units/ml DNase I (Roche) in RPMI medium (American Type Culture Collection, Manassas, VA) for 45 minutes at 37°C. The digestion was quenched by the addition of 0.5 ml fetal bovine serum (Invitrogen) and passed through a cell strainer (BD Biosciences, San Jose, CA). Cells were washed with sterile phosphate buffered saline (PBS, Invitrogen) and red blood cells were lysed for 5 minutes in 5 ml lysis buffer composed of 8.26 g ammonium chloride, 1 g potassium bicarbonate, and 0.037 EDTA per liter of water. Lysis was quenched with 45 ml PBS, cells spun down, and then resuspended and stained for flow cytometry. For flow cytometric analysis, cells were incubated with fluorescently labeled antibodies, including PE anti-human HLA-A2 (BioLegend, San Diego, CA) to distinguish human cells and propidium iodide (Sigma Aldrich, St Louis, MO) for live/dead analysis. Cells were washed with PBS, then run on flow cytometry using an Accuri c6 cytometer (BD Biosciences) and 4 color detection.

Immunofluorescence protocol

Frozen slides were first air dried for approximately 30 minutes, then tissue samples circled with a PAP pen (Invitrogen, Carlsbad, CA). Tissues were fixed for 10 minutes at room temperature in formalin, then washed 3 times with PBS. Blocking was performed with 5% goat serum (Invitrogen) in PBS for 1 hour at room temp. Primary antibody incubation was 5% goat serum in PBS + 1:100 rat anti-mouse CD31 (BD Pharmingen, San Diego, CA) overnight at 4°C. Slides were then washed three times with PBS, then incubated with PBS+0.1% Tween 20 (Sigma-Aldrich, St. Louis, MO) + 1:200 goat anti-rat 546 (Invitrogen, Carlsbad, CA) + 1:100 goat anti-human Fc 488 antibody for 1 hour at room temperature. Slides were washed 4 times with PBS, then mounted in Vectashield + DAPI medium (Vector Labs, Burlingame, CA).

Fluorescence imaging

Slides were imaged using a DeltaVision Spectris microscope (Applied Precision, Issaquah, WA) equipped with a motorized stage and running Softworx software (Applied Precision). Emission

and excitation filters were arranged to permit simultaneous 4-color imaging of DAPI, 488, 546, and 647. The paneling feature of Softworx was used to capture the entire tumor section at a resolution of 1.336 $\mu\text{m}/\text{pixel}$ and to stitch together the fields into a single large mosaic image for subsequent analysis.

Unbiased Image Analysis

Rather than introduce potential observer bias by manually selecting individual blood vessels for analysis, images were analyzed as entire tumor sections for features including intervessel distance, antibody penetration from blood vessels, and antigen distribution. The 546 nm (blood vessel) plane was isolated, thresholded to include vessels only, and converted to a binary image using ImageJ (NIH, Bethesda, MD). A Euclidean distance map was created from the vessel binary, and this map was used as a mask to measure average intensity in the antibody (488 and/or 647) plane as a function of distance from nearest blood vessel by an automated MATLAB (The Mathworks, Natick, MA) computer program. Regions of the tumor revealed to be necrotic or stromal tissue by examination of H&E staining or by absence of antigen were excluded from the analysis.

Modeling

Antibody extravasation was modeled using an extension of a previously described Krogh cylinder model of the tumor vasculature^{20,21}. A mathematical model, detailed in Appendix A, was solved numerically in MATLAB (MathWorks, Natick, MA) using the method of lines and the built-in numerical ordinary differential equation solver. Simulation results are reported as fractional antigen saturation as defined below:

$$\text{Fractional saturation} = \frac{\text{Antibody bound to tumor antigen} + \text{free antibody in tumor interstitium}}{\text{Total tumor antigen}}$$

All simulation results were reported at a 24 hour time point to match experimental results. The parameters which inform the model were all either directly measured or taken from the literature (Appendix A).

4.3 Results

To compare varying dosing strategies of a therapeutic antibody, an experiment was devised to administer the EGFR-targeted trispecific antibody HN-D/LC-A via three different dosing regimens in a mouse xenograft model of cancer. This antibody was administered to mice bearing HCT-116 colorectal cancer xenografts, a model in which EGFR was previously shown to be downregulated by HN-D/LC-A¹⁴. Antibody treatment was carried out in three treatment groups as shown in Figure 4.2, plus a PBS vehicle control group. A fixed dose of 300 μg of HN-D/LC-A weekly was administered, split into either a single weekly bolus dose, twice weekly doses, or daily doses of only 43 μg . Tumor growth was monitored regularly throughout the treatment period of five weeks. The penultimate dose of antibody was labeled with Alexa Fluor 647 fluorescent dye, and the final dose at 24 hours before euthanasia was labeled with Alexa Fluor 488 fluorescent dye.

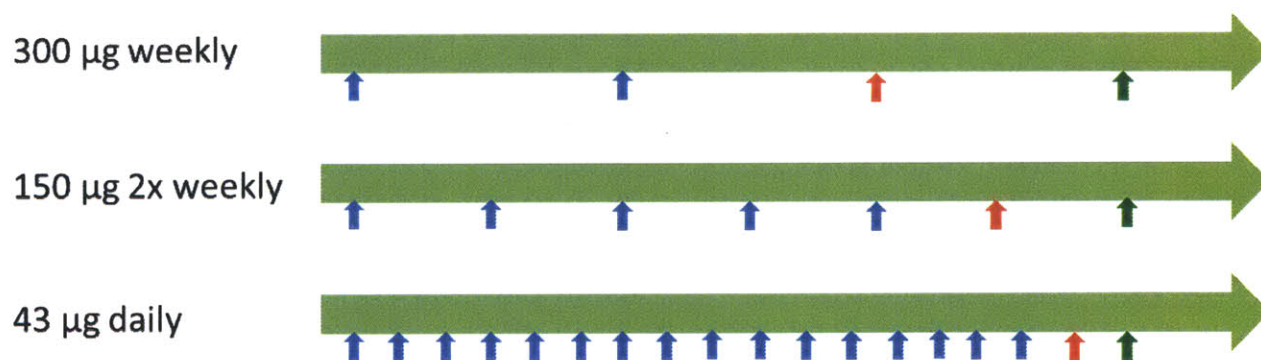


Figure 4.2. Illustration of HN-D/LC-A dosing schedule. Top, 300 μg dose given weekly. Middle, 150 μg dose given twice weekly. Bottom, 43 μg dose given daily. All doses sum to 300 μg total weekly dose. Arrows indicate doses; red arrows indicate 647-labeled HN-D/LC-A doses, and green arrows represent 488-labeled doses. All mice were sacrificed 24 hours following administration of the last dose (488-labeled dose).

Modeling of expected plasma concentrations of HN-D/LC-A and tumor penetration profiles based upon a Krogh cylinder model were carried out concurrently with the *in vivo* experiment. The results of these simulation are shown in Figure 4.3. In the case of weekly and twice weekly HN-D/LC-A injections, tumor plasma concentrations change little from dose to dose. In general, there is a spike around the time of the injection, then a rapid decline in plasma concentrations

to a fraction of the peak. The pattern repeats with each dose, with a marginal increase in maximal plasma concentrations with the first few doses. In contrast, the daily dosing schedule displays the same peak-to-valley distribution, but with a marked change in the average plasma concentration of the therapeutic during the first few doses. The first 3-5 doses show a gradual increase in plasma concentration until achieving an apparent plateau approximately one week after beginning dosing.

The predicted distribution of the therapeutics around blood vessels also shows a distinct profile dependent upon the dosing regimen. In the case of daily injections, the radius of targeted tissue increases with time and number of doses, plateauing after approximately a week. Twice weekly and weekly dosing strategies shown less of a dependence on time, presumably because the plasma concentrations with time are little changed over repeated doses. Interestingly, these more widely spaced doses show the effects of antigen-mediated endocytosis (Figure 4.3 weekly dosing). In this case, the distribution between doses is markedly different than the distribution immediately following doses. Between doses, because relatively little HN-D/LC-A is available in the circulation, antigen-mediated catabolism dominates and markedly reduces the penetration of extravasated HN-D/LC-A into the tumor tissue. This effect is seen less in the case of twice weekly dosing and very little in the case of daily dosing because plasma drug concentrations are maintained at higher levels.

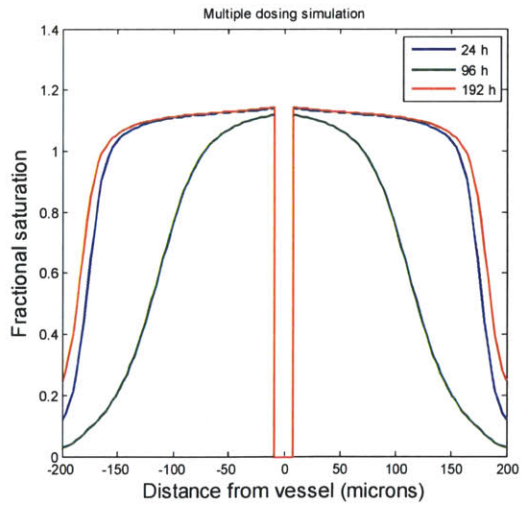
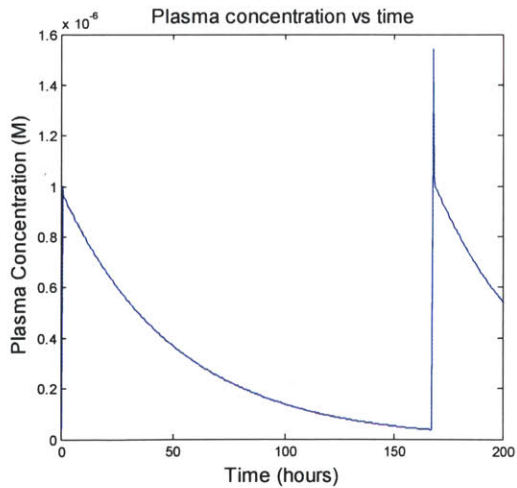
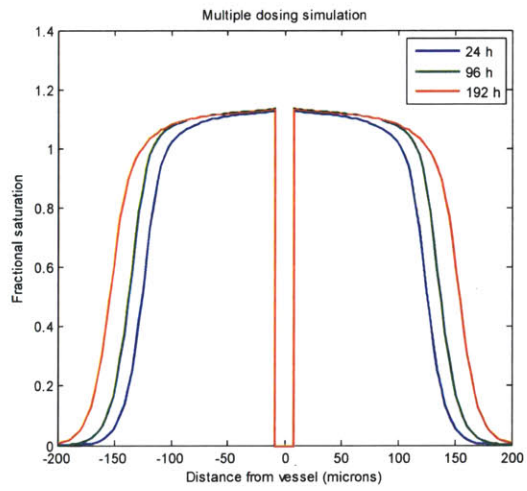
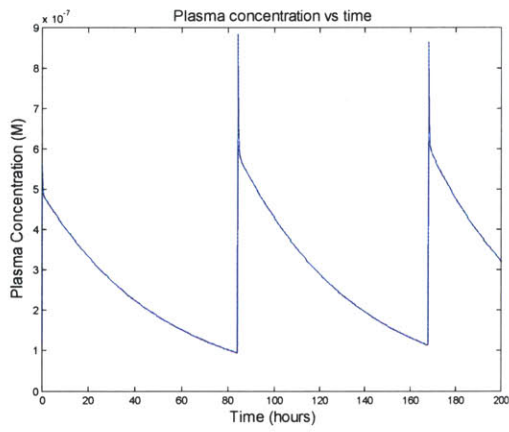
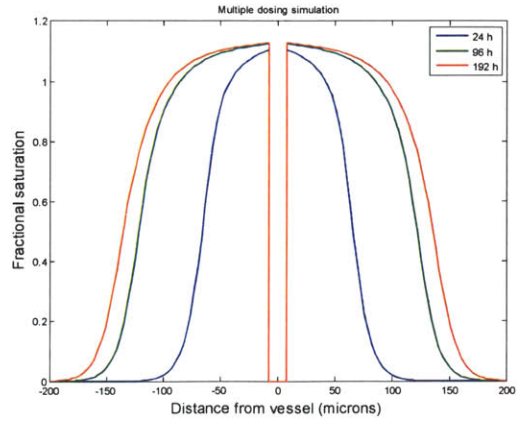
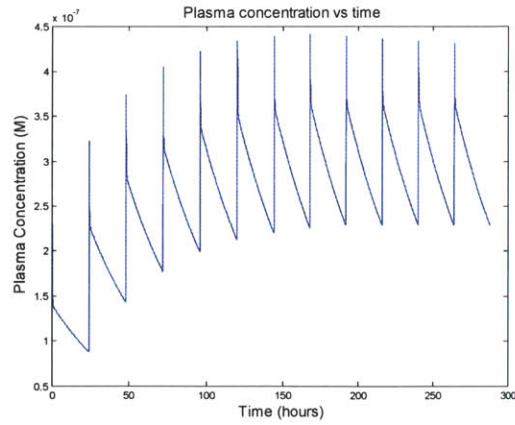


Figure 4.3. Simulated plasma concentration (left column) and perivascular distribution profile at different time points (right column). Top, daily dosing; middle, twice weekly dosing; bottom, weekly dosing. All dosing strategies administered 300 μg of HN-D/LC-A per weekly period.

Tumor growth was highly heterogeneous, as shown in Figure 4.4. Average tumor sizes never significantly diverged from one another throughout the five weeks of treatment, and all three treatment groups were statistically indistinguishable from one another and the PBS control group at the end of the treatment cycle. Examination of the individual tumor growth curves gives some insights into the growth characteristics of the tumors. Two tumors grew much more rapidly than the rest of the tumors, and several tumors, including two in the twice weekly treatment group, were quite well controlled and in one case complete remission was achieved. The majority of the tumors grew at a similar, gradual pace during antibody treatment.

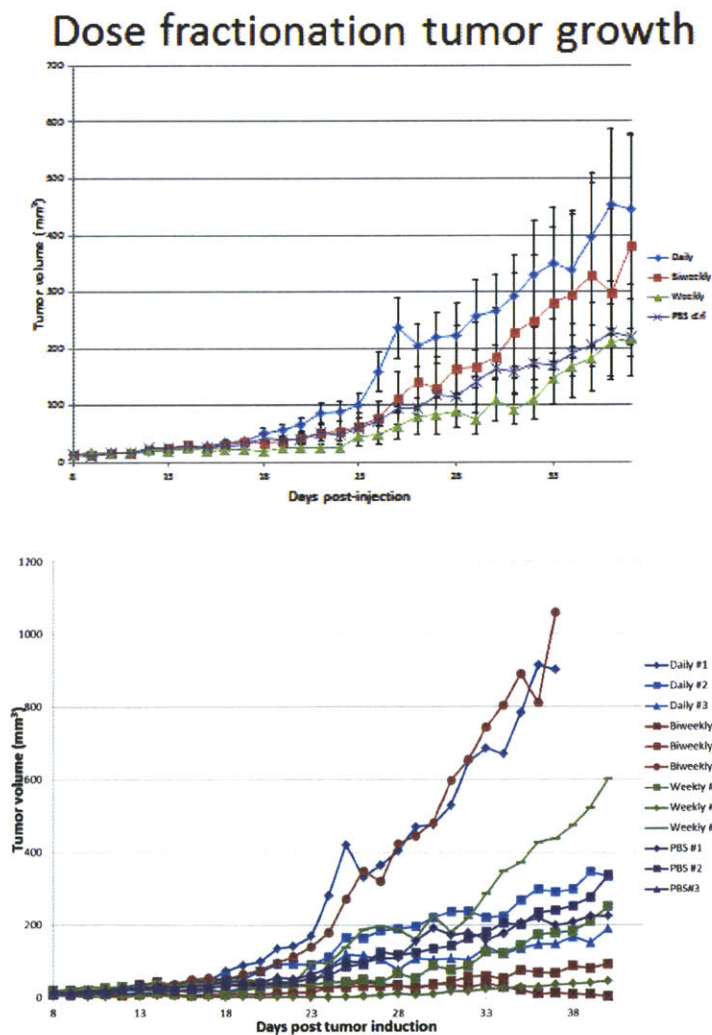


Figure 4.4. Growth of xenograft tumors. Average tumor sizes (error bars \pm S.E.) are shown at left, and individual tumor curves are shown at right. Tumor were measured by calipers daily and volumes estimated by $L^2 \times W/2$.

Upon reaching the end of five weeks of antibody treatment, the mice were sacrificed and the tumors excised for analysis. Each tumor was cut in half, and one of these halves was dissociated and stained for human cells by human HLA antibody and viability by propidium iodide. Four color flow cytometry also allowed the collection of fluorescence data corresponding to the Alexa Fluor 488 and 647 labeled therapeutic antibodies. Several thousand cells were collected for each of seven mice, and the results of the flow cytometric analysis of these mice are shown in Figure 4.5. In the case of both fluorophores, no apparent signal could be observed. The PBS control mice, which received no antibody, were indistinguishable from each of the three treatment groups. This was the case for not only the penultimate dose of 647-labeled protein (Figure 4.5, right) but also the last dose of 488-labeled protein which was administered 24 hours prior to euthanasia for all mice.

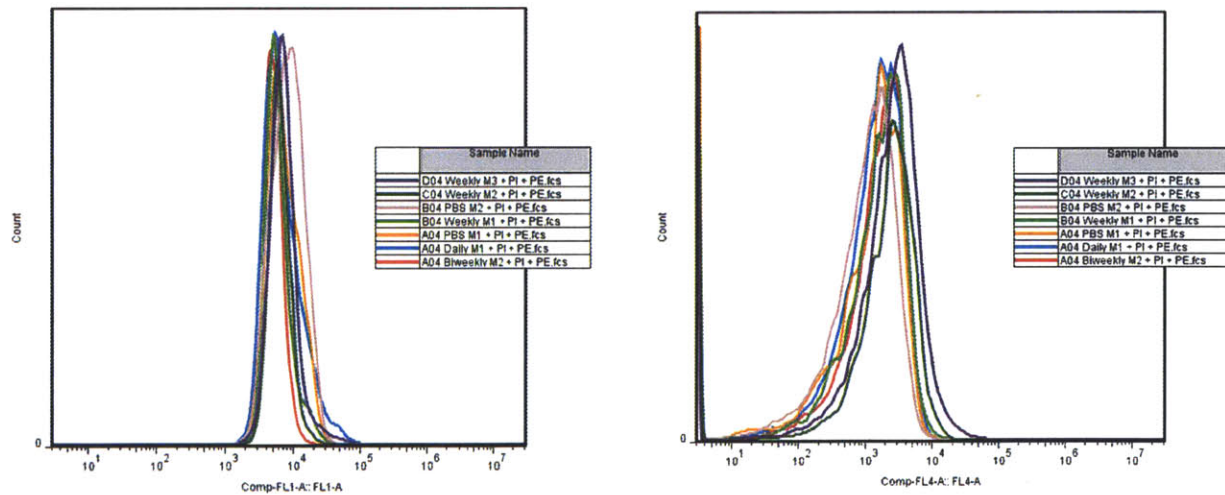


Figure 4.5. Flow cytometric analysis of dissociated tumor xenografts freshly excised from the flanks of tumor-bearing mice. The penultimate antibody dose was labeled with Alexa Fluor 647 (cytometry gate FL4) and the last dose of antibody, administered 24 hours prior to tumor excision, was labeled with Alexa Fluor 488. At left, results of 7 mice, at least one from each treatment group, in the FL1 channel. At right, results of the same 7 mice in the FL4 channel. Gating was done on human HLA-positive cells which were viable by PI staining.

The second half of each tumor was flash frozen, sectioned, and immunofluorescently stained for DAPI and CD31. These tumors were examined using a fluorescence microscope. At low magnification, little evidence of the 488 or 647 signals corresponding to the last and penultimate HN-D/LC-A doses was present. However, at high magnification, evidence of both fluorophores became apparent as shown in Figure 4.6. In particular, the last dose which was labeled with Alexa Fluor 488 could clearly be seen and was distributed in a punctate manner which has previously been documented for this EGFR trispecific antibody¹⁴. The 647-labeled dose, which was administered 48 hours to 8 days prior to euthanasia, depending on the dosing scheme, was occasionally observed but was markedly less intense as well as less widely distributed. The antibody signal could only be observed at an appreciable signal when magnified 40x or greater, and since this magnification would require many thousands of individual panels to be stitched together to reconstitute the entire tumor, it was not computationally feasible to image the entire tumor for paneling. Instead, multiple regions of apparent antibody signal were acquired for each tumor for subsequent analysis and quantitation of antibody signal and localization.

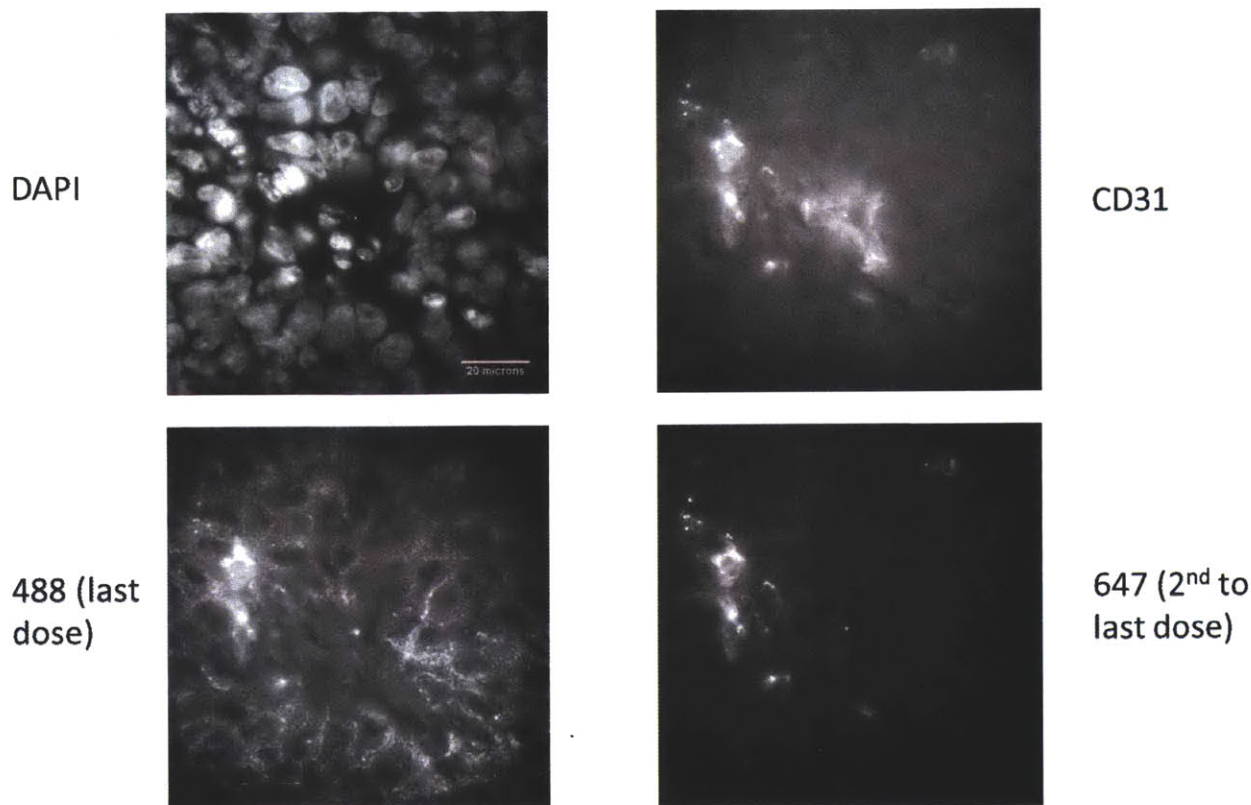


Figure 4.6. Representative high-magnification immunofluorescent images of HCT-116 xenograft tumor sections. DAPI and CD31 staining were clear and consistent throughout the tumor. Evidence of the last antibody dosed appears in the 488 channel, where the antibody can be observed distributed around perfused blood vessels and clustered into punctate spots around cell membranes. The penultimate antibody dose was 647 labeled and was administered 2 days prior to euthasia (daily dosing), 4 days prior to euthanasia (twice weekly dosing), or 8 days prior to euthanasia (weekly dosing).

Adding to the complications for immunofluorescent imaging of the HCT-116 was the unusual distribution of viable tumor tissue in the tumor sections. Examination of H&E sections from these tumors reveals a serpiginous distribution of necrotic tissue in these sections, regardless of treatment schedule or size of the tumor (Figure 4.7). Around much of the periphery of the tumor and throughout the interior of the tumor in small “islands” around blood vessels are pockets of viable tumor tissue. However, they are often surrounded by necrotic tissue, making analysis of large regions of the tumor difficult because these large regions tend to be composed largely of dead tissue.

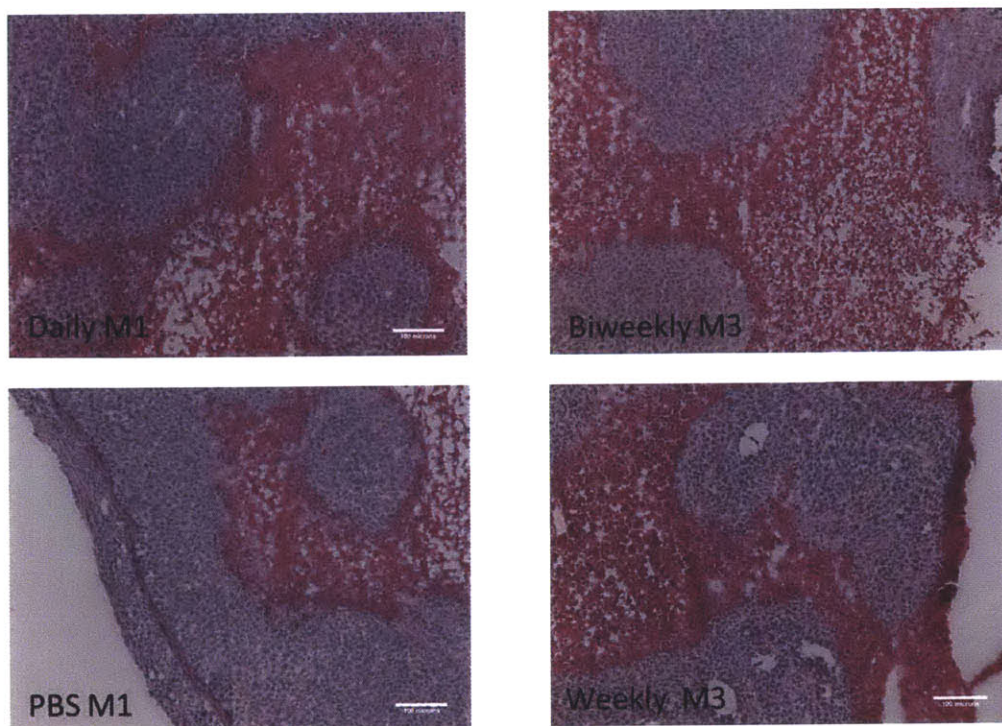


Figure 4.7. Representative H&E images of tumor sections from all four treatment groups. Lighter purple areas are viable tumor cells and tend to be localized in all sections around the periphery of the tumor and in small pockets in the interior of the tumor. Pink to red regions surrounding these viable pockets are regions of necrotic tissue.

This complication, along with the observation that 488 and 647 antibody signals corresponding to the injected antibody were quite low and only visible at high magnification, led to the decision to visualize injected antibody with an anti-human Fc secondary antibody. Using this secondary antibody dramatically increases the immunofluorescent signal corresponding to the injected antibody (Figure 4.8) at the cost of the loss of the ability to distinguish the last dose and penultimate dose from one another. In addition, because viable tumor tissue was only present in small pockets throughout the tumor, vessels were isolated for analysis on a vessel-by-vessel basis with 5-12 representative vessels chosen from each tumor section for analysis as depicted in Figure 4.8.

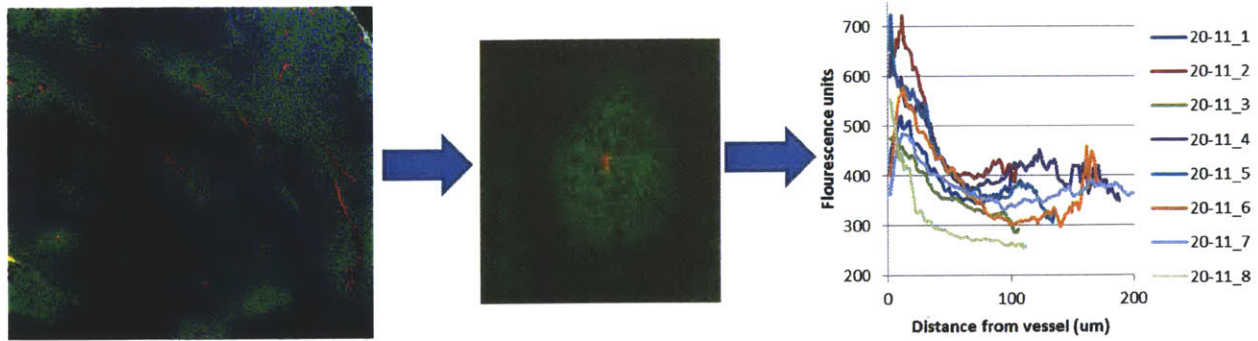


Figure 4.8. Representative immunofluorescent images and data analysis using anti-human Fc-488 secondary antibody to visualize injected HN-D/LC-A antibody. At left, low magnification (10x) image of DAPI (blue), HN-D/LC-A (green), and CD31 (red). Middle, image of a representative vessel chosen for subsequent image analysis and quantitation. Green represents extravasated antibody, and red CD31. Right, example of analysis of antibody intensity and perivascular localization in several such vessels.

Analysis of the images of single vessels in many different tumor sections is depicted in Figure 4.9. It can clearly be seen that substantial heterogeneity exists from section to section, even within each treatment group. In most tumors, antibody intensity shows a modest dependence on proximity to nearest vessel, although there are a few tumors which do not. All tumors show enhanced antibody signal near blood vessels relative to PBS controls and stromal tissue. In this study, stromal tissue comes from one tumor that was controlled by treatment (Figure 4.4) and was revealed to be scar tissue upon tumor excision. Maximum antibody intensity and decrease in intensity with distance are highly variable through the sections.

On average (Figure 4.9), the antibody intensity profiles in the three treatment groups follow very similar patterns. There is a perivascular localization of antibody, with highest signal nearest the blood vessel and a decrease in signal through approximately 100 μm . There is no statistical difference between the treatment groups, although all three are substantially different than the PBS cohort or the stromal tissue.

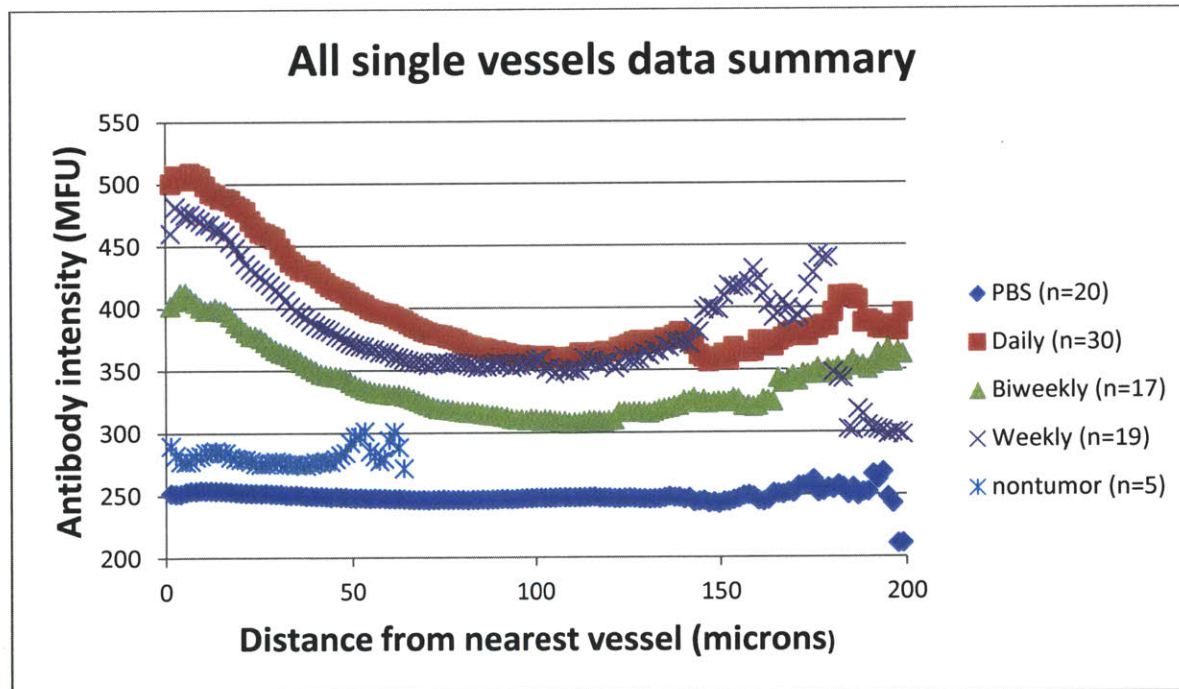
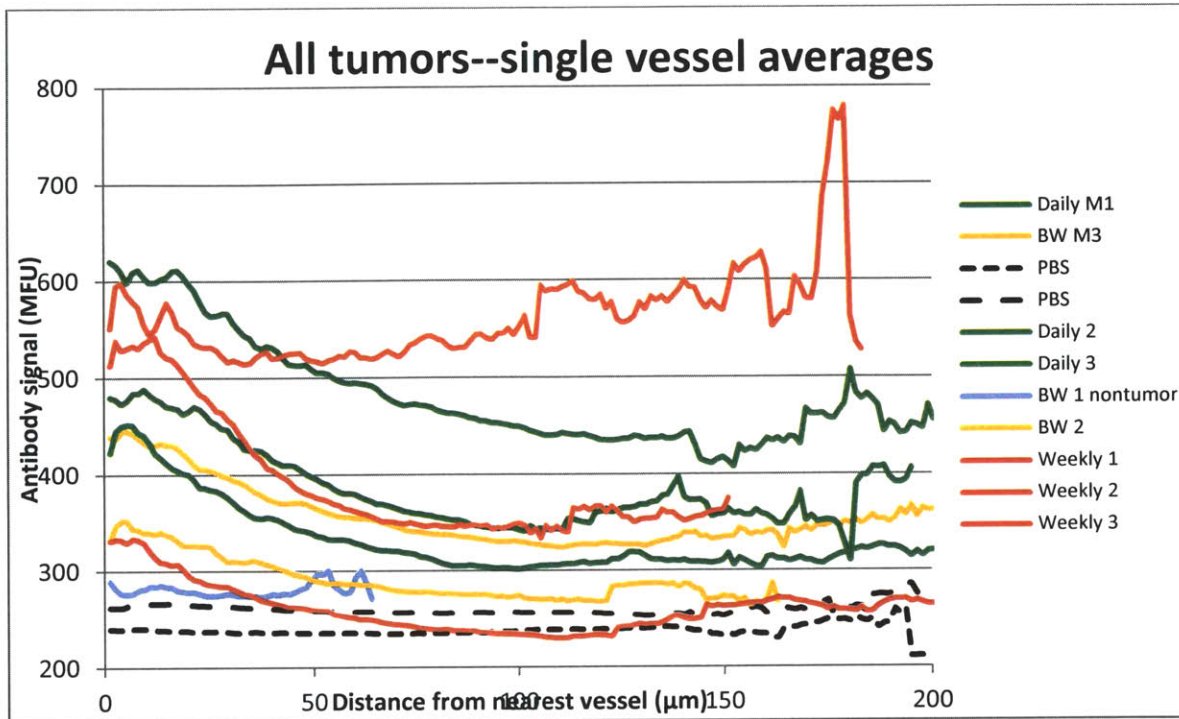


Figure 4.9. Top, antibody intensity vs. distance from nearest vessel for each tumor analyzed. Curves represent averages of 5-12 vessels per tumor. Bottom, average of all vessels for each treatment group. Nontumor tissue refers to scar tissue found in place of tumor in a mouse which experienced complete tumor regression. Error bars not shown for clarity. No significant difference was observed between treatment groups.

4.4 Discussion

We present here a study of efficacy and intratumor microdistribution of therapeutic monoclonal antibodies administered through several different dosing strategies. A fixed weekly quantity of a trispecific anti-EGFR antibody was dosed either weekly, twice weekly, or daily for a five week course of treatment of mice bearing xenograft tumors shown to be sensitive to the treatment *in vitro*. Tumor growth inhibition was monitored during the treatment regimen, and following treatment the remaining tumors were resected, sectioned, and quantitatively analyzed for levels and perivascular localization characteristics of the extravasated and bound antibody in the tumor sections. Through these studies, we sought to correlate any observed differences in tumor control with the degree to which the antibody therapeutics were able to penetrate the tumor tissue.

The tumor growth inhibition part of the study demonstrated a great deal of heterogeneity in the growth rate of the tumors regardless of treatment group or schedule. Some tumors grew quite rapidly, while others grew gradually. No significant difference in tumor growth rate was observed between groups or relative to PBS-treated control mice. Although not statistically significant, it is interesting to note that four of the five smallest tumors at the conclusion of the study, including the only tumor to regress completely, belonged to the weekly or biweekly treatment groups, which also received the largest bolus doses of antibody. The heterogeneity in tumor growth makes it difficult to draw conclusions and appears to be somewhat random. For instance, as shown in Figure 4.10, the size of the tumor at the start of treatment (day 10) is strongly correlated with the size at after nearly 4 weeks of treatment, regardless of treatment regimen.

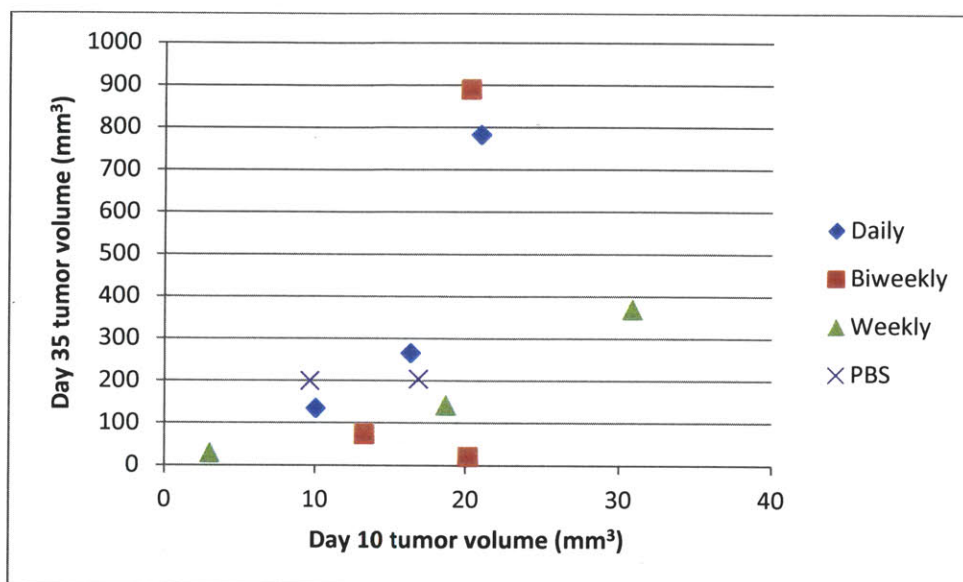


Figure 4.10. Tumor volume measured near the start of treatment (day 10) vs. the size of the tumor after 3.5 weeks of HN-D/LC-A treatment (day 35). Regardless of treatment group or schedule, the size of the tumor at day 35 is correlated with its size at the start of treatment.

The results of the analysis of antibody penetration into tumor tissue indicate that tumor penetration was not significantly different between the tumor groups. Efforts to use flow cytometry to quantify the fraction of tumor cells targeted by antibody failed. This likely occurred because the process used to dissociate the tumor involves proteolytic enzymes to separate tumor cells which may also have dissociated the bound antibody from the cells. It is possible that a more mild dissociation protocol may have given different results. However, frozen tumor sections retained bound antibody and were amenable to immunofluorescent imaging and study. Weak signal could be observed from the last two doses of fluorescently labeled antibody administered to the mice in some cases. However, the signal was weak and only readily observable under high magnification. We hypothesize that the signal was weak because EGFR is a very rapidly internalized and degraded antigen, especially when targeted by HN-D/LC-A¹⁴. It seems plausible that the 24 hour period between the last antibody dose and collection of the tumor was enough time for a substantial quantity of the antibody to be degraded, reducing the signal to the degree observed.

To enhance the signal of the bound HN-D/LC-A, a secondary antibody was used, resulting in the loss of the ability to distinguish between the penultimate and final antibody doses, but dramatically increasing the immunofluorescent signal to a level more amenable to imaging large regions of the tumor for subsequent quantitative analysis. Tumors were imaged in this manner and stitched together to be analyzed for quantitation of antibody distribution around blood vessels. However, examination of H&E sections of adjacent tumor tissue revealed that ~70-80% of the tumor was necrotic, regardless of treatment schedule (Figure 4.7). Moreover, the necrotic regions were distributed in a serpiginous fashion, leaving “islands” of viable tissue distributed throughout the tumor and near the tumor periphery. This growth pattern appeared in the control mice as well as treated mice, and so it seems to be part of the normal growth characteristics of this tumor cell line.

Since these tumor sections were dominated by necrotic tissue and therefore not amenable to large-scale analysis entire tumor sections, small regions of vascularized viable tissue were chosen for analysis. Many such regions were identified in each tumor section, resulting in tens of vessels per dose schedule for subsequent analysis. This analysis (Figure 4.9) revealed a great deal of heterogeneity in the distribution of antibody between tumor sections. All tumor sections had antibody signal well above background in the perivascular region, but there were no clear trends in the distribution among the daily, twice weekly, and weekly treatment groups. On the average, all three treatment groups showed a perivascular antibody distribution with detectable antibody penetrating to a distance of approximately 100 μm . However, the amount of antibody detected was statistically indistinguishable across the three groups.

Mathematical modeling based upon a Krogh cylinder model of the tumor tissue has been used previously to quantitatively probe the distribution of antibody around tumor blood vessels^{10,20}. When applied to HCT-116 tumors and known characteristics of EGFR endocytosis and trafficking, the simulated distribution of daily, twice weekly, and weekly doses can be generated as shown in Figure 4.11. All three dosing schedules are predicted to have similar perivascular distributions, especially after 8 or more days of treatment. Experimentally, this is exactly what was observed. The daily injection simulation suggests that tumor penetration is

gradually enhanced over the first approximately one week of treatment, after which plasma antibody concentrations have reached a consistent range as shown in Figure 4.3 and the penetration profile has reached its maximum. In contrast, the more widely spaced doses are separated by a time that is several times longer than the antibody serum half life, and so the serum concentrations fall to near zero levels prior to each successive dose. As a consequence, each dose exists essentially independent of the others and the penetration profile with these dosing schedules is little changed with time.

It is important to note that this modeling does not take into account the pharmacodynamics of the treatment. In this experiment, HCT-116 tumors were not consistently well controlled by the HN-D/LC-A treatment, and so the experiment and model (which does not consider tumor control or growth) can be compared with some degree of confidence. However, in a therapeutic context in which effective targeting of tumor antigen can be expected to result in some degree of cell killing, the model will need to be altered to take this into account. No evidence of serial dosing strategies enhancing efficacy was seen with this model, but perhaps a more efficacious drug would be more impactful and allow a better understanding of the potential relationship between antibody penetration and antitumor efficacy.

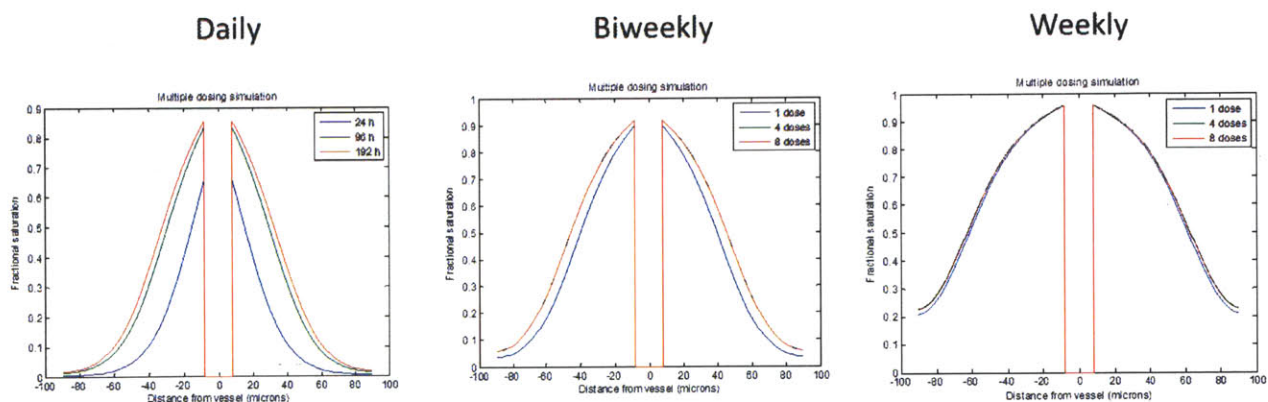


Figure 4.11. Numerical simulations of antibody distribution profiles based upon a Krogh cylinder geometry and HCT-116 EGFR density and turnover rate. Parameters from the literature and measured in the laboratory for antibody clearance, permeability and diffusivity, as well as tumor parameters such as tumor cell density, antigens per cell, antigen turnover rate, and void fraction, were used to simulate antibody distribution at varying times and for daily, twice weekly, and weekly antibody injections. In all cases, a fixed 300 μg weekly dose was simulated and identical parameters other than antibody dosing were used. PHarmacodynamic effects of treatment, e.g. receptor downregulation or tumor control, are ignored in this simulation.

4.5 References

1. Adams, G. P. *et al.* High affinity restricts the localization and tumor penetration of single-chain Fv antibody molecules. *Cancer Research* **61**, 4750–4755 (2001).
2. Freeman, D. J. *et al.* Tumor penetration and epidermal growth factor receptor saturation by panitumumab correlate with antitumor activity in a preclinical model of human cancer. *Molecular Cancer* **11**, 47 (2012).
3. Minchinton, A. I. & Tannock, I. F. Drug penetration in solid tumours. *Nature Reviews Cancer* **6**, 583–592 (2006).
4. Pastuskovas, C. V. *et al.* Effects of anti-VEGF on pharmacokinetics, biodistribution and tumor penetration of trastuzumab in a preclinical breast cancer model. *Molecular Cancer Therapeutics* (2012).doi:10.1158/1535-7163.MCT-11-0742-T
5. Rudnick, S. I. *et al.* Influence of Affinity and Antigen Internalization on the Uptake and Penetration of Anti-HER2 Antibodies in Solid Tumors. *Cancer Research* **71**, 2250–2259 (2011).
6. Thurber, G. M., Schmidt, M. & Wittrup, K. D. Antibody tumor penetration: Transport opposed by systemic and antigen-mediated clearance. *Advanced Drug Delivery Reviews* (2008).
7. Carol M Lee & Ian F Tannock The distribution of the therapeutic monoclonal antibodies cetuximab and trastuzumab within solid tumors. *BMC Cancer* **10**, (2010).
8. Fidarova, E. F. *et al.* Microdistribution of Targeted, Fluorescently Labeled Anti-Carcinoembryonic Antigen Antibody in Metastatic Colorectal Cancer: Implications for Radioimmunotherapy. *Clinical Cancer Research* **14**, 2639–2646 (2008).
9. Flynn, A. A., Boxer, G. M., Begent, R. H. J. & Pedley, R. B. Relationship between tumour morphology, antigen and antibody distribution measured by fusion of digital phosphor and photographic images. *Cancer Immunology Immunotherapy* **50**, 77–81 (2001).
10. Rhoden, J. J. & Wittrup, K. D. Dose dependence of intratumoral perivascular distribution of monoclonal antibodies. *Journal of Pharmaceutical Sciences* **101**, 860–867 (2012).
11. Sato, N. *et al.* Intratumoral Distribution of Radiolabeled Antibody and Radioimmunotherapy in Experimental Liver Metastases Model of Nude Mouse. *J Nucl Med* **40**, 685–692 (1999).
12. Saltz, L. B. *et al.* Phase II Trial of Cetuximab in Patients With Refractory Colorectal Cancer That Expresses the Epidermal Growth Factor Receptor. *JCO* **22**, 1201–1208 (2004).
13. Robert, N. *et al.* Randomized Phase III Study of Trastuzumab, Paclitaxel, and Carboplatin Compared With Trastuzumab and Paclitaxel in Women With HER-2–Overexpressing Metastatic Breast Cancer. *JCO* **24**, 2786–2792 (2006).

14. Spangler, J. B., Manzari, M. T., Rosalia, E. K., Chen, T. F. & Wittrup, K. D. Triepitopic Antibody Fusions Inhibit Cetuximab-Resistant BRAF and KRAS Mutant Tumors via EGFR Signal Repression. *Journal of molecular biology* (2012).doi:10.1016/j.jmb.2012.06.014
15. Naundorf, S. *et al.* In vitro and in vivo activity of MT201, a fully human monoclonal antibody for pancreatic carcinoma treatment. *International Journal of Cancer* **100**, 101–110 (2002).
16. Ackerman, M. E., Pawlowski, D. & Wittrup, K. D. Effect of antigen turnover rate and expression level on antibody penetration into tumor spheroids. *Molecular Cancer Therapeutics* **7**, 2233–2240 (2008).
17. Mittendorf, E. A. *et al.* Loss of HER2 Amplification Following Trastuzumab-Based Neoadjuvant Systemic Therapy and Survival Outcomes. *Clin Cancer Res* **15**, 7381–7388 (2009).
18. Nahta, R., Takahashi, T., Ueno, N. T., Hung, M.-C. & Esteva, F. J. P27kip1 Down-Regulation Is Associated with Trastuzumab Resistance in Breast Cancer Cells. *Cancer Res* **64**, 3981–3986 (2004).
19. Smith, M. R. Rituximab (monoclonal anti-CD20 antibody): mechanisms of action and resistance. *Oncogene* **22**, 7359–7368 (2003).
20. Thurber, G. M., Zajic, S. C. & Wittrup, K. D. Theoretic Criteria for Antibody Penetration into Solid Tumors and Micrometastases. *Journal of Nuclear Medicine* **48**, 995–999 (2007).
21. Krogh, A. The number and distribution of capillaries in muscles with calculations of the oxygen pressure head necessary for supplying the tissue. *J Physiol* **52**, 409–415 (1919).

5. ORTHOTOPIC AND ECTOPIC XENOGRAFT TUMORS

5.1 Introduction

Xenograft mouse models of cancer have been used for the study of cancer and to screen potential cancer therapeutics *in vivo* for decades. Mice are inexpensive, can be bred rapidly, and were among the first organisms to have their genome completely sequenced, advancing the study of cancer genetics¹. These models have contributed to the understanding of the biology of cancer and to elucidating the efficacy and mechanism of action of many anticancer agents. Because many different cancer cell lines representing cancers of many different types and origins can be studied in xenograft models, they models have been perceived as very flexible platforms.

The canonical host of xenograft tumors is the nude, or athymic, mouse. In 1972, it was shown that nude mice, which lack a thymus and therefore lack mature T-cells and are unable to mount an effective immune response against foreign tissue, can act as hosts for human tumor cells². Many preclinical drug efficacy studies have been carried out using the nude mouse model, most often utilizing subcutaneous implantation of hundreds of thousands to millions of cancer cells to generate a solid tumor. This model is in wide use because of the ease of inducing tumors and the accessibility of the tumor which arises to observation and measurement. Virtually all prospective therapeutics must prove efficacy in a mouse model of cancer before reaching human clinical trials. However, the predictive power of subcutaneous xenograft models of cancer is debatable³.

A recent study by the National Cancer Institute attempted to examine the predictive power of xenograft models by retrospective analysis of 39 oncology compounds with data on both preclinical xenograft testing and phase II clinical trials. This study showed that fewer than half of all compounds which showed substantial efficacy in mouse models showed statistically significant clinical activity⁴. These data are complicated by the myriad variables inherent in xenograft studies, e.g. site of implantation, size of tumor at treatment initiation, strain of

mouse used, and route of administration. However, they do raise questions regarding the predictive utility of subcutaneous xenograft models in the context of human disease.

One of the properties often lacking in subcutaneous xenograft models of cancer is interaction with the host stromal tissue. Tumors are initiated by injection of hundreds of thousands to millions of cells, which then begin to grow in the mouse. Once reaching a size of approximately one millimeter in diameter, they must recruit murine vasculature in order to support their continued growth⁵. Not only must murine vasculature be recruited to human tumor cells, but the signaling pathways and molecules which are involved in angiogenesis are complex and inconsistent between species⁶. In addition, it has recently become clear that stromal tissue in the tumor microenvironment can play an important role in tumor signaling, angiogenesis, and immune surveillance⁷⁻¹⁰.

One of the fundamental differences between xenograft tumors and the clinical diseases which they are intended to model is the placement in the body. Most xenograft tumors are implanted subcutaneously, regardless of the type of tumor and the organ from which the tumor originates. As a consequence, cancer cells which are derived from colorectal or lung cancer are grown in a subcutaneous environment which little resembles the organ in which the primary tumor formed.

In some cases, it is possible to establish tumors in an orthotopic fashion in the organ from which the cancer cells are derived. These models are less common because they are generally more difficult to establish. They may require surgery or image-guided implantation, and once the tumors are established they are often not observable to the naked eye. In these cases, tumor growth and development may be monitored by some form of *in vivo* imaging, but this is more time consuming and often less precise than the simple caliper-based measurement of subcutaneous xenografts¹¹. However, there is evidence to suggest that orthotopic and ectopic tumors may have different properties with relevance to drug efficacy and drug development.

For example, although tumors in the clinic often metastasize, ectopic xenograft tumors virtually never do, but some orthotopic models do metastasize in a pattern similar to the primary tumors they seek to model¹²⁻¹⁵. Moreover, metastatic tumor cells injected into ectopic

locations in nude mice fail to metastasize, but injections into orthotopic locations often do metastasize¹⁶. There is also evidence to suggest that the efficacy of drugs screened in preclinical mouse models can vary depending upon whether the tumors are induced orthotopically or ectopically^{13,17}. Presumably, these differences are due to the differing tumor microenvironments and resulting biochemical and biophysical environments in which the tumors grow.

In this work, we seek to examine two sets of tumors derived from human cancer cell lines and induced orthotopically and ectopically in the same host mouse. We aim to determine whether factors in the tumor microenvironment, such as vascular density and expression levels of antigen, vary depending on tumor site. We also seek to evaluate whether the intratumoral distribution of antibodies is affected by tumor location. This work has the potential to help in choosing the appropriate mouse cancer model which captures the relevant features of the disease while maximizing ease of use and accessibility of the model.

5.2 Materials and methods

Reagents

A low-picomolar humanized antibody to carcinoembryonic antigen (CEA), designated sm3e, has previously been engineered and characterized¹⁸. In addition, murine IgG2a antibody TA99 has been shown to target the melanosome protein gp75 which is highly expressed in melanoma¹⁹. This antibody was humanized and shown to retain binding to cell surface gp75. These antibodies were secreted in transiently transfected HEK 293 cells (Invitrogen, Carlsbad, CA), purified by protein A resin (Millipore, Billerica, MA) and buffer exchanged into PBS. Anti-CEA monoclonal antibody M85151a was purchased from Fitzgerald (Acton, MA) and goat anti-rat 546 secondary antibody from Invitrogen. Antibody M85151a was labeled with an Alexa Fluor 647 Protein Labeling kit (Invitrogen) and has been previously determined to be noncompetitive with sm3e²⁰. Human TA99 antibody was also labeled with an Alexa Fluor 647 protein labeling kit.

Animal model

Animal use and care was conducted in full compliance and under approval from the MIT Committee on Animal Care. Two cell lines were utilized in this study. HT-CEA, a CEA-positive human sarcoma cancer cell line, was used to induce subcutaneous xenograft formation in the flank and intramuscular xenografts in the hind leg muscle of 6-8 week old Ncr nude mice (Taconic, Hudson, NY) by injection of 1×10^6 cancer cells into each site. B16F10, a murine metastatic melanoma cell line which highly expresses gp75, was used to induce subcutaneous xenografts by injection of 1×10^5 cells into the flank and intramuscular xenografts by injection of 2×10^5 cells into the hind leg muscle of NCr nude mice. Tumors were allowed to grow until measuring 3-10 mm in diameter in each site, then either sm3e or TA99 was injected retroorbitally into HT-CEA or B16F10 tumor bearing mice, respectively. Both antibodies were administered at a dose of 20 μ g, a dose chosen to be subsaturating of the tumor antigen. Mice were sacrificed 24 hours after antibody administration, and tumors were immediately excised and snap frozen in Optimal Cutting Temperature (OCT) medium (Sakura Finetek USA, Torrance, CA) via isopentane over liquid nitrogen. Frozen blocks were stored at -80°C until sectioned by the Koch Institute Histology Core Facility. Frozen blocks were sectioned approximately 1-2 mm into the tumor tissue at a thickness of 8 μ m and stored at -80°C until stained and imaged.

Immunofluorescence protocol

Frozen slides were first air dried for approximately 30 minutes, then tissue samples circled with a PAP pen (Invitrogen, Carlsbad, CA). Tissues were fixed for 10 minutes at room temperature in formalin, then washed 3 times with PBS. Blocking was performed with 5% goat serum (Invitrogen) in PBS for 1 hour at room temp. Primary antibody incubation was 5% goat serum in PBS + 1:100 rat anti-mouse CD31 (BD Pharmingen, San Diego, CA) overnight at 4°C . Slides were then washed three times with PBS, then incubated with PBS+0.1% Tween 20 (Sigma-Aldrich, St. Louis, MO) + 1:200 goat anti-rat 546 (Invitrogen, Carlsbad, CA) + 1:100 goat anti-human Fc 488 + 1:100 M85151a-647 (HT-CEA tumors) or 1:100 TA99-647 (B16F10 tumors) antibody for 1 hour at room temperature. Slides were washed 4 times with PBS, then mounted in Vectashield + DAPI medium (Vector Labs, Burlingame, CA).

Fluorescence imaging

Slides were imaged using a DeltaVision Spectris microscope (Applied Precision, Issaquah, WA) equipped with a motorized stage and running Softworx software (Applied Precision). Emission and excitation filters were arranged to permit simultaneous 4-color imaging of DAPI, 488, 546, and 647. The paneling feature of Softworx was used to capture the entire tumor section at a resolution of 1.336 $\mu\text{m}/\text{pixel}$ and to stitch together the fields into a single large mosaic image for subsequent analysis.

Unbiased Image Analysis

Rather than introduce potential observer bias by manually selecting individual blood vessels for analysis, images were analyzed as entire tumor sections for features including intervessel distance, antibody penetration from blood vessels, and antigen distribution. The 546 nm (blood vessel) plane was isolated, thresholded to include vessels only, and converted to a binary image using ImageJ (NIH, Bethesda, MD). A Euclidean distance map was created from the vessel binary, and this map was used as a mask to measure average intensity in the antibody (488) plane as a function of distance from nearest blood vessel by an automated MATLAB (The Mathworks, Natick, MA) computer program. Regions of the tumor revealed to be necrotic or stromal tissue by examination of H&E staining or by absence of antigen were excluded from the analysis.

5.3 Results

Xenograft tumors from both ectopic and orthotopic locations were immunofluorescently stained for extravasated antibody and processed with an unbiased image analysis algorithm to quantitate antibody intensity and localization relative to blood vessels. Results presenting the data in a variety of ways are shown in Figure 5.1 for the HT-CEA cell line and Figure 5.2 for the B16F10 cell line. Raw intensity data are shown for both sets of tumors, as well as data normalized to the background signal present in antigen-negative regions of the tumor. This normalization helps to elucidate the perivascular profile of the antibody signal since

background signal can vary somewhat from section to section. Finally, for the HT-CEA tumor sections, a noncompetitive anti-CEA antibody was used to visualize antigen distribution, allowing the antibody signal to be normalized to antigen signal as a function of distance from the nearest vessel. No such noncompetitive antibody was available for the B16F10 tumor sections.

HT-CEA tumors highly express CEA at approximately 1×10^6 antigens per cell, and as predicted by previous modeling analyses were poorly penetrated by the moderate dose of anti-CEA antibody dosed in this model²¹. A perivascular distribution which is characteristic of many monoclonal antibodies in solid tumors was observed, with the apparent penetration into the tumor tissue measuring approximately 50-80 μm . No significant difference in antibody levels or distribution profile was observed between the orthotopic and ectopic tumor models.

B16F10 tumors express the gp75 antigen on the cell surface. These tumors were also dosed with antitumor antibody at a subsaturating level and showed a perivascular localization of the antibody. The immunofluorescent signal from the bound antibody was detectable but relatively weak, possibly due to signal attenuation attributable to the melanin pigment that is highly expressed in this tumor. However, examination of the normalized antibody distribution shows tissue penetration to a distance of 40-60 μm , and as in the HT-CEA tumor model no significant difference in penetration distance or distribution profile is observed between the orthotopic and ectopic tumor models.

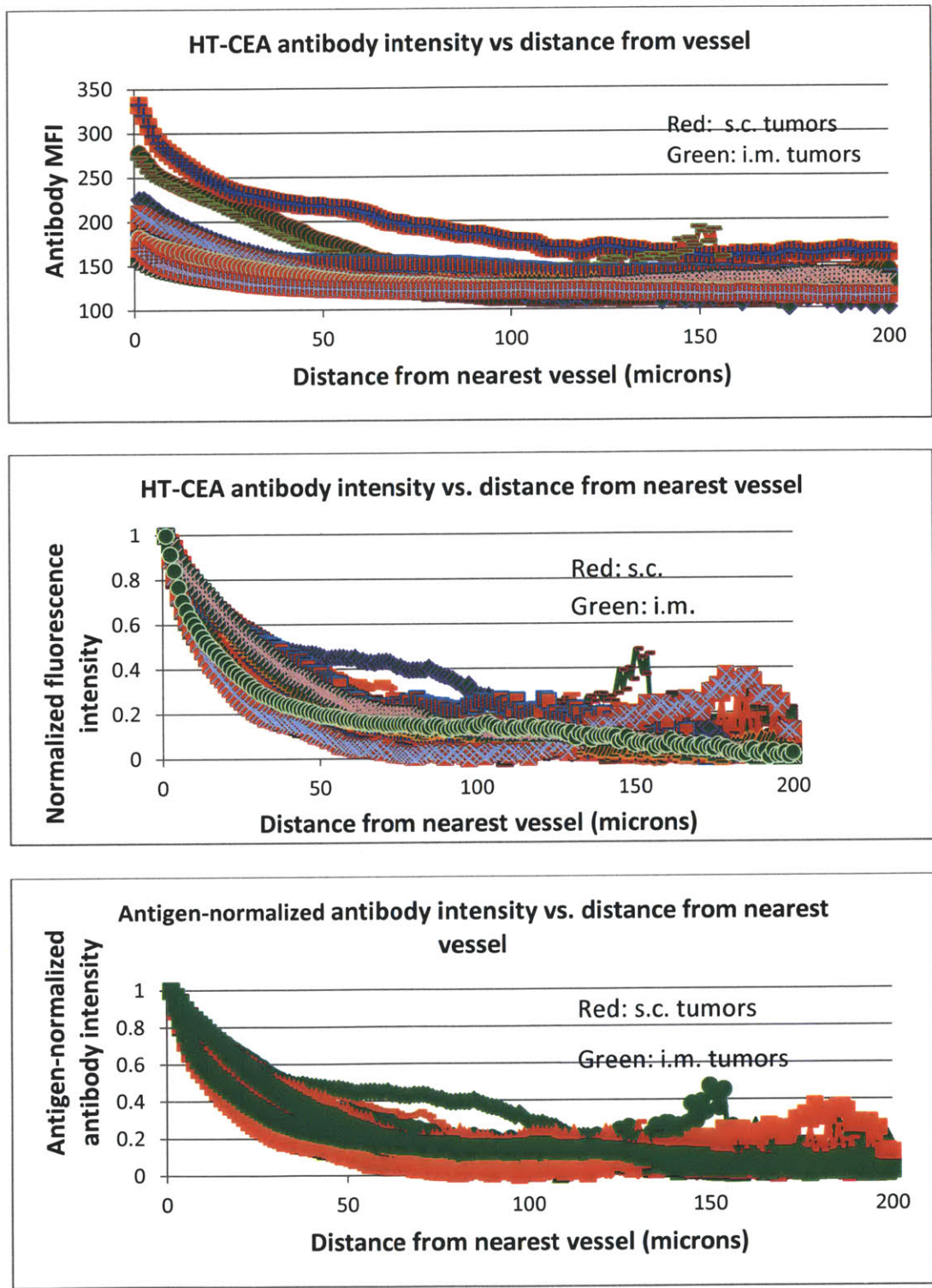


Figure 5.1. HT-CEA xenograft tumor antibody distribution around blood vessels. Top, raw antibody intensity vs. distance from nearest blood vessel. Middle, antibody intensity normalized to background vs distance from nearest blood vessel. Bottom, antibody intensity normalized to antigen signal at each distance from nearest blood vessel. Red curves denote subcutaneous (ectopic) tumors and green curves denote intramuscular (orthotopic) tumors.

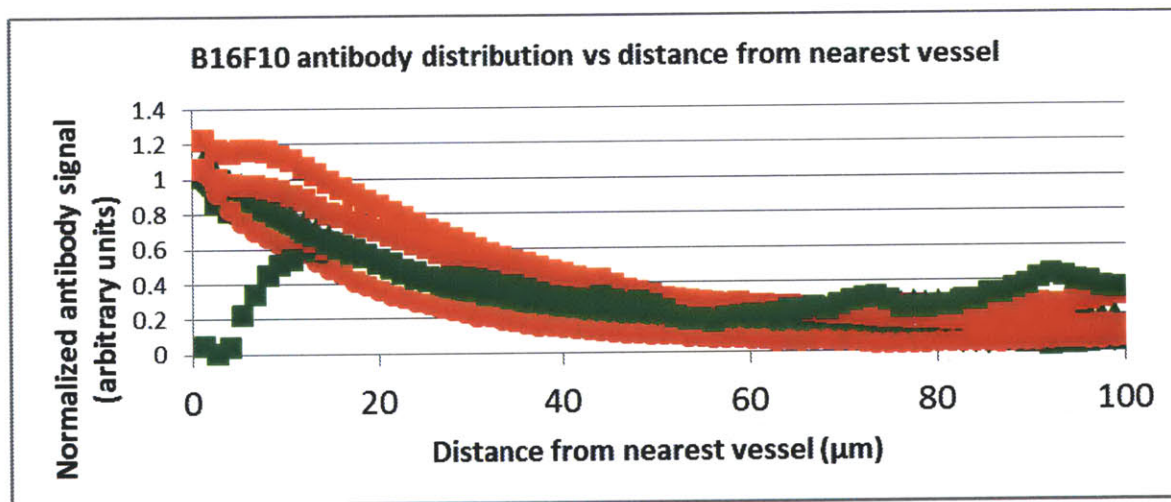
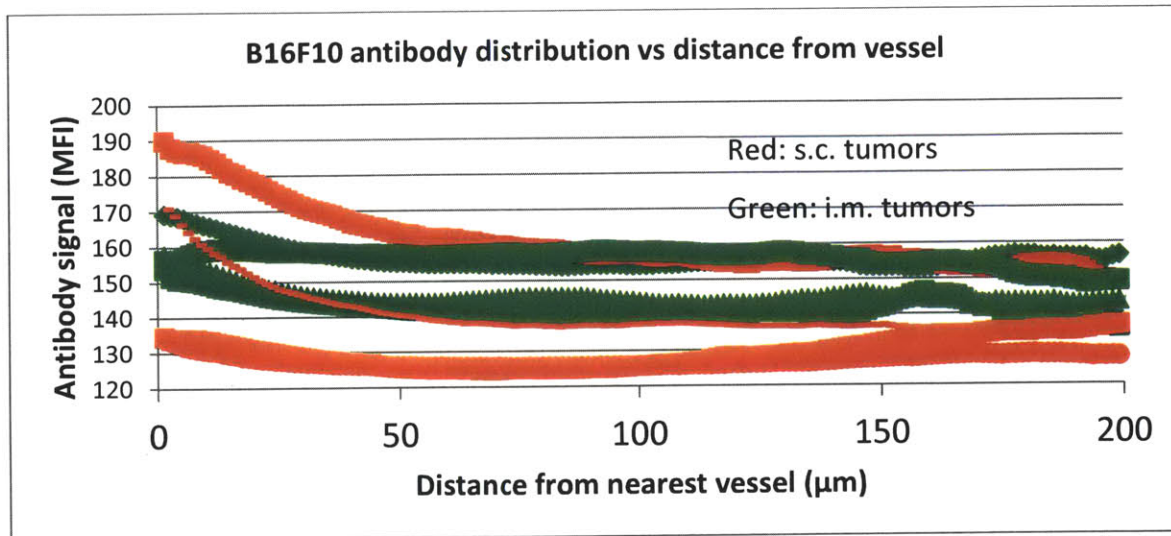


Figure 5.2. B16F10 xenograft tumor antibody distribution around blood vessels. Top, raw antibody intensity vs. distance from nearest blood vessel. Bottom, antibody intensity normalized to background signal vs. distance from nearest blood vessel. Red curves denote subcutaneous (orthotopic) tumors and green curves represent intramuscular (ectopic) tumors.

A similar analysis was conducted on both sets of tumors to determine antigen expression levels and intratumoral distribution (Figure 5.3). For the HT-CEA tumors, the noncompetitive anti-CEA antibody allows the determination of antigen distribution throughout the tumor section. The B16F10 tumors do not have a corresponding noncompetitive antibody, and so the antigen intensity as measured by immunofluorescence is attenuated where extravasated antibody

bound and occupies antigen. This is especially apparent near blood vessels, where the signal is modestly reduced due to the relatively large amount of bound antibody in these regions.

Antigen analysis conducted on HT-CEA xenografts shows a highly variable antigen signal from tumor-to-tumor. However, the variations in antigen levels do not appear to correlate with tumor placement, as both ectopic and orthotopic tumors vary in their antigen expression levels. Antigen intensity within individual tumor sections appears to be relatively homogeneous and does not correlate strongly with distance from the nearest blood vessel. Several tumors are exceptions to this and show a modest decrease in antigen signal with distance from nearest blood vessel.

The B16F10 xenografts show a much more consistent degree of antigen expression (Figure 5.3). Most of the tumors analyzed have very similar antigen expression levels. As in the HT-CEA tumors, there is little change in antigen expression with distance from the nearest blood vessel. It should be noted that any perivascular antigen level measurements may be altered by the presence of antibody that extravasated and bound tumor antigen before the mouse was euthanized, and so only data farther than the penetration distance of the antibody (40-60 μm) from the nearest blood vessel is free from this potential source of error.

To examine the vascular density of the tumor tissue, histograms were generated for each tumor type and tumor location of the fraction of tumor tissue present at each discrete distance (pixel) from the nearest blood vessel. These plots are shown in Figure 5.4. All tumors show a similar distribution of a large fraction of tumor tissue located quite close to blood vessels, with peak fractional areas located within 50 μm of blood vessels. For HT-CEA tumors, the large majority of the tumor tissue is located within 60 μm of the tumor tissue, indicating that these tumors are highly vascularized. No difference in vascularity was observed in orthotopic vs. ectopic placements of the HT-CEA cell line. The B16F10 tumors, however, showed a distribution shifted toward greater distances from the tumor tissue. In these tumors the large majority of the tumor tissue is located within 150-200 μm of the tumor tissue, indicating that they are much less well vascularized. The B16F10 tumors also show a slight but insignificant difference in vascularity by tumor location, with subcutaneous (orthotopic) tumors slightly less well vascularized than intramuscular (ectopic) tumors.

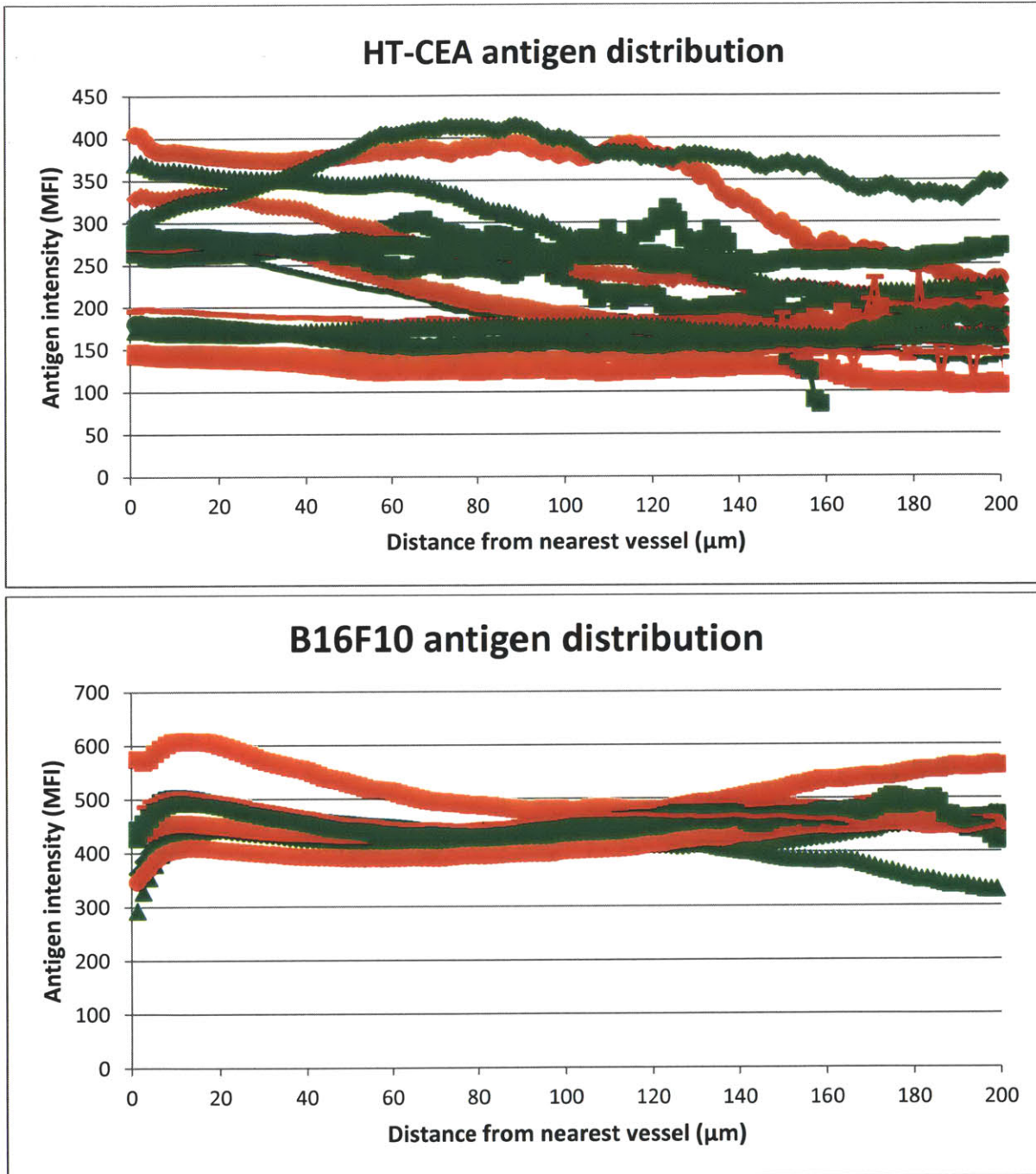


Figure 5.3. Antigen intensity and localization in xenograft tumors. Top, HT-CEA antigen distribution in intramuscular tumors (orthotopic, red curves) and subcutaneous tumors (ectopic, green curves). Bottom, B16F10 antigen (gp75) distribution in intramuscular tumors (ectopic, red curves) and subcutaneous tumors (orthotopic, green curves). Note that the B16F10 anti-gp75 antibody used to quantitate antigen levels is the same as the antibody dosed to the mice, leading to competition between the antibodies and a decreased signal especially near the blood vessels where the antibody extravasates and binds to a high degree.

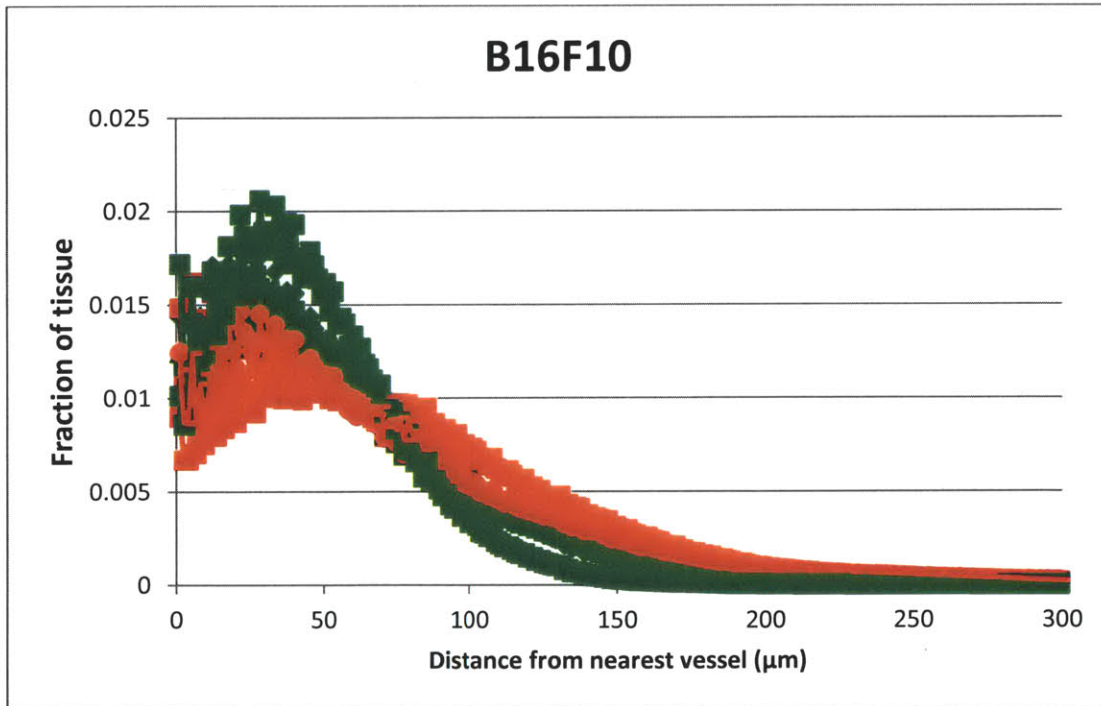
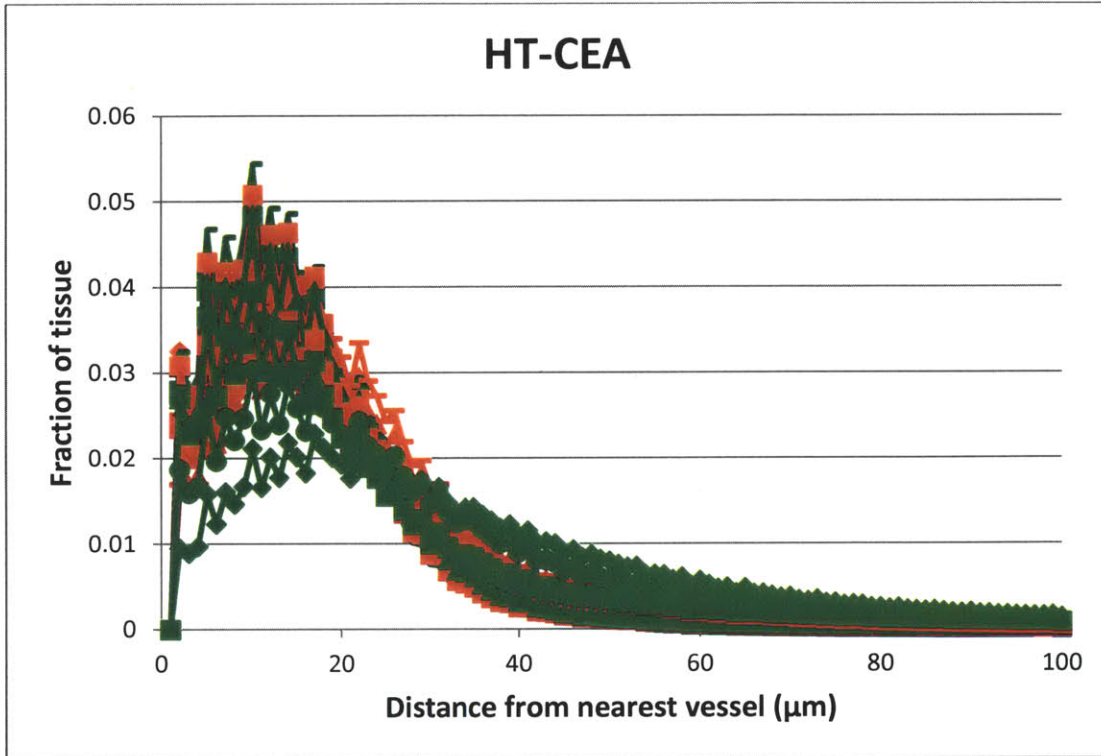


Figure 5.4. Tissue distribution around blood vessels histogram. The fraction of tumor tissue present at each discrete distance from the nearest blood vessel is plotted. Top, HT-CEA and bottom, B16F10. Red curves denote subcutaneous tumors and green curves intramuscular tumors.

5.4 Discussion

We present here a study of antibody distribution, antigen distribution, and vascularization of mouse xenograft models of human tumors in orthotopic and ectopic locations. A previously described method of immunofluorescence and unbiased quantitative image analysis allows the determination of antibody as well as antigen intensity as a function of distance from blood vessels at a resolution of approximately 1.25 microns. This analysis was applied to tumors derived from two different cell lines, each implanted in both orthotopic and ectopic locations in the same mouse. This creates a well-controlled model system for the determination of the effects of tumor placement on antibody targeting.

As shown in Figures 5.1 and 5.2, all tumors and tumor locations showed antibody binding to tumor antigen in a perivascular fashion. This distribution was anticipated from mathematical modeling and predictions from the literature, and indicates that doses of antibodies to these tumors were below the level required to saturate the tumor antigen²¹. Since the doses were subsaturating, analysis of the perivascular distribution of antibody was possible. This analysis did not show any dependence on tumor location in either the HT-CEA or B16F10 tumor cell lines. Instead, all tumors showed a similar perivascular distribution profile. Each tumor type was penetrated to a characteristic distance of ~50-80 μm for the HT-CEA tumors and ~40-60 μm for the B16F10 tumors. No significant difference in penetration distance was seen in orthotopic or ectopic tumor locations.

Quantitative analysis of antigen distribution and expression level was also carried out for all tumors. The HT-CEA tumors were particularly amenable to this analysis because the availability of a noncompetitive anti-CEA antibody allowed the entire tumor sections to be imaged and quantitated without interference from the extravasated antibody dosed to the mice. These tumors showed substantial tumor-to-tumor variability in antigen expression (Figure 5.3). The B16F10 tumors showed considerably less variation in antigen expression. Across all tumor types and locations, few tumors showed a strong variation in antigen expression versus distance from the nearest blood vessel. This was expected, as the analysis was restricted to areas of viable tumor tissue.

Interestingly, analysis of tumor antigen expression in tumors matched to the mice in which they grew shows patterns emerging (figure 5.5). The HT-CEA tumors show dramatic variation in antigen expression within the same mouse, while B16F10 tumors do not show such variation. In the HT-CEA tumors, most mice show higher antigen expression in the orthotopic location, but the difference is not statistically significant and no such trend is seen in the B16F10 tumors.

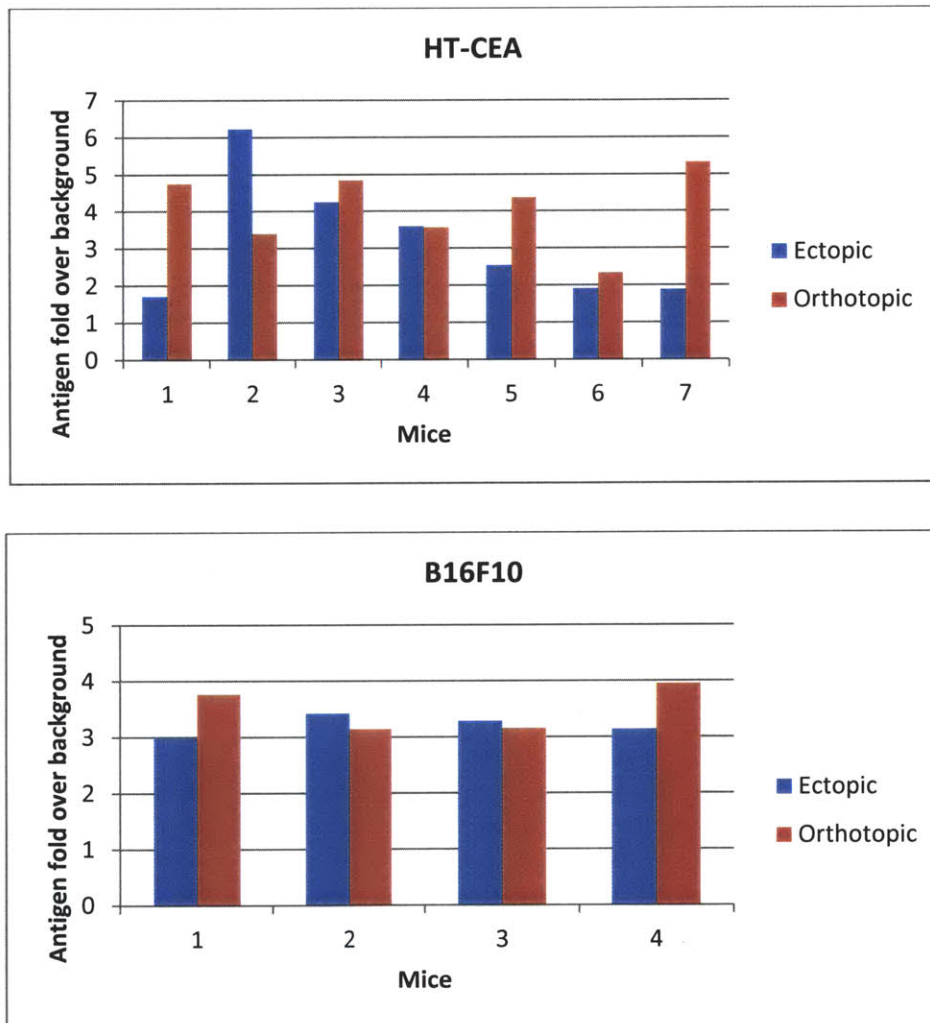


Figure 5.5. Comparison of antigen expression in orthotopic and ectopic tumors within in same mouse for HT-CEA (top) and B16F10 (bottom) xenograft tumors. Antigen expression was quantitated as the fold over background for the average of the antigen intensity from 40-60 μm from the nearest blood vessel.

The vascularization of the two different tumors is dramatically different (Figure 5.4). The HT-CEA tumors are very vascularized and the large majority of tumor tissue is located within approximately 50 μm of the blood vessels. Virtually no tissue is farther than 100 μm from the vessels. In contrast, the B16F10 tumors are much less vascularized and viable tissue exists out to approximately 200 μm , which agrees well with the diffusion limit of oxygen²². Again, though, little difference in vascularity is seen within a tumor type between orthotopic and ectopic tumor locations.

These results seem to suggest that, at least for these tumor models, tumor location does not play a significant role in the microdistribution of antibodies in tumor tissue. One potential explanation for this is that for xenograft tumors, the majority of the tumor microenvironment is made up of tumor cells and little stromal tissue is present in the tumor. As a result, the transport of macromolecules through the tumor interstitium is consistent across tumor locations. It has previously been shown that interstitial fluid pressure (IFP) can be higher in orthotopic tumors than ectopic tumors²³. It could be argued that this would be expected to impede the transport of antibodies into orthotopic tumors. However, it has also been shown that tumors have elevated IFP in general and that this serves to reduce convective transvascular transport to a level that is negligible relative to diffusive transport²⁴⁻²⁶. In this case, elevated IFP would have little effect on antibody transport because it is primarily diffusive in nature.

Another potential cause of the similarity in properties between orthotopic and ectopic tumors is the nature of xenografts. The tumor tissue appears histologically homogeneous as a layer of tumor cells with very little secondary structure. As such, inside the tumor there is little contact with the host tissue surrounding the tumor. Only at the edges of the tumor are interactions apparent as depicted in Figure 5.6. As shown, there are regions in the HT-CEA intramuscular (orthotopic) tumor site which clearly show invasion of the tumor tissue into the surrounding muscle fibers. However, these regions make up only a small fraction of the tumor tissue in this xenograft model. We believe that models which capture this invasive nature and the physical interaction of host tissue and tumor tissue are important for future investigations into the role of the tumor environment on the transport and penetration of antibodies into the tumor tissue.

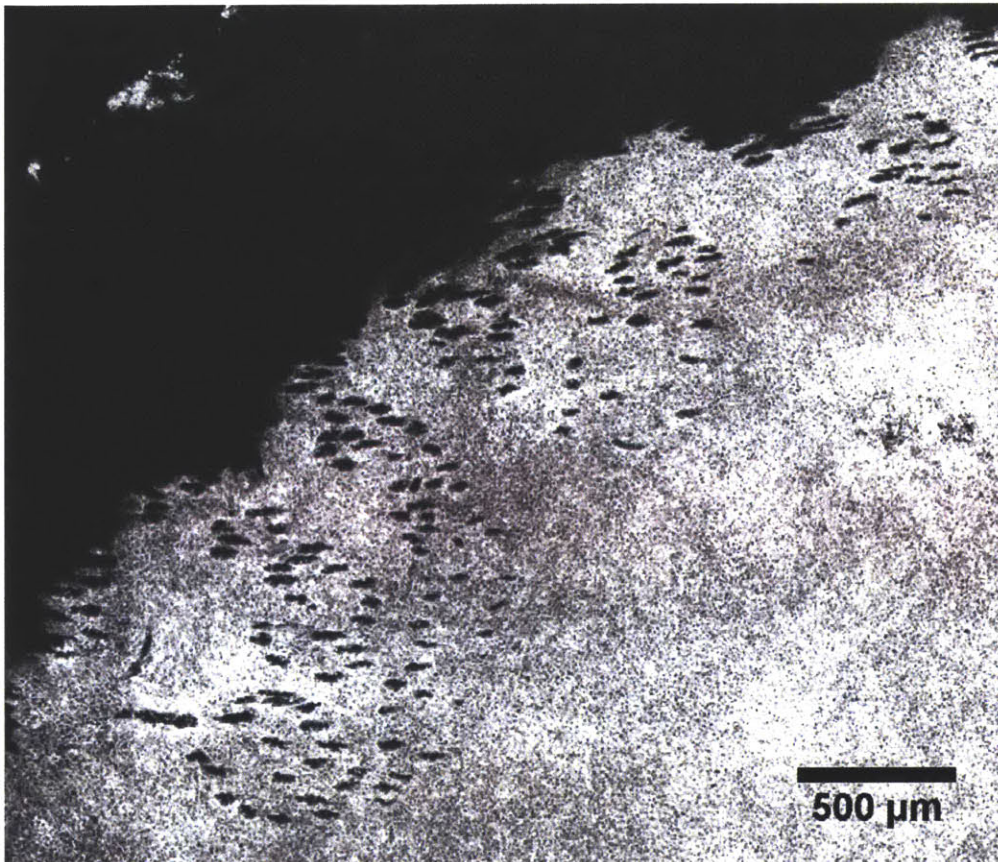


Figure 5.6. Immunofluorescent image of the antigen (CEA) in a HT-CEA xenograft tumor placed in the intramuscular (orthotopic) location. The dim tissue in the upper left of the image is the muscle, and the “holes” in the tissue near the boundary of the tumor and the muscle are muscle fibers. Tumor tissue in this region is actively invading into the muscle.

5.5 References

1. Waterston, R. H. *et al.* Initial sequencing and comparative analysis of the mouse genome. *Nature* **420**, 520–562 (2002).
2. Povlsen, C. O. & Rygaard, J. Heterotransplantation of human epidermoid carcinomas to the mouse mutant nude. *Acta Pathol Microbiol Scand A* **80**, 713–717 (1972).
3. Kelland, L. R. ‘Of mice and men’: values and liabilities of the athymic nude mouse model in anticancer drug development. *European Journal of Cancer* **40**, 827–836 (2004).
4. Relationships between drug activity in NCI preclinical in vitro and in vivo models and early clinical trials. *British Journal of Cancer* **84**, (2001).
5. Folkman, J. Anti-angiogenesis: new concept for therapy of solid tumors. *Ann Surg* **175**, 409–416 (1972).
6. Folkman, J. How Is Blood Vessel Growth Regulated in Normal and Neoplastic Tissue?—G. H. A. Clowes Memorial Award Lecture. *Cancer Res* **46**, 467–473 (1986).
7. Bhowmick, N. A. & Moses, H. L. Tumor-stroma interactions. *Current Opinion in Genetics & Development* **15**, 97–101 (2005).
8. Fukumura, D. & Jain, R. K. Tumor microvasculature and microenvironment: Targets for anti-angiogenesis and normalization. *Microvascular Research* **74**, 72–84 (2007).
9. Hanahan, D. & Coussens, L. M. Accessories to the Crime: Functions of Cells Recruited to the Tumor Microenvironment. *Cancer Cell* **21**, 309–322 (2012).
10. Tredan, O., Galmarini, C. M., Patel, K. & Tannock, I. F. Drug resistance and the solid tumor microenvironment. *Journal of the National Cancer Institute* **99**, 1441–1454 (2007).
11. Weissleder, R. Scaling down imaging: Molecular mapping of cancer in mice. *Nature Reviews Cancer* **2**, 1–8 (2002).
12. Tan, M. H., Holyoke, E. D. & Goldrosen, M. H. Murine colon adenocarcinoma: syngeneic orthotopic transplantation and subsequent hepatic metastases. *J. Natl. Cancer Inst.* **59**, 1537–1544 (1977).
13. Killion, J. J., Radinsky, R. & Fidler, I. J. Orthotopic models are necessary to predict therapy of transplantable tumors in mice. *Cancer Metastasis Rev.* **17**, 279–284 (1998).
14. Giavazzi, R., Campbell, D. E., Jessup, J. M., Cleary, K. & Fidler, I. J. Metastatic Behavior of Tumor Cells Isolated from Primary and Metastatic Human Colorectal Carcinomas Implanted into Different Sites in Nude Mice. *Cancer Res* **46**, 1928–1933 (1986).

15. Naito, S., Eschenbach, A. C. von, Giavazzi, R. & Fidler, I. J. Growth and Metastasis of Tumor Cells Isolated from a Human Renal Cell Carcinoma Implanted into Different Organs of Nude Mice. *Cancer Res* **46**, 4109–4115 (1986).
16. Fidler, I. J. Critical Factors in the Biology of Human Cancer Metastasis: Twenty-eighth G. H. A. Clowes Memorial Award Lecture. *Cancer Res* **50**, 6130–6138 (1990).
17. Wilmanns, C., Fan, D., O'Brian, C. A., Bucana, C. D. & Fidler, I. J. Orthotopic and ectopic organ environments differentially influence the sensitivity of murine colon carcinoma cells to doxorubicin and 5-fluorouracil. *Int. J. Cancer* **52**, 98–104 (1992).
18. Graff, C. P., Chester, K., Begent, R. & Wittrup, K. D. Directed evolution of an anti-carcinoembryonic antigen scFv with a 4-day monovalent dissociation half-time at 37 C. *Protein Engineering, Design & Selection* **17**, 293–304 (2004).
19. Implicating a role for immune recognition of self in tumor rejection: passive immunization against the brown locus protein. *J Exp Med* **182**, 1609–1614 (1995).
20. Schmidt, M. M., Thurber, G. M. & Wittrup, K. D. Kinetics of anti-carcinoembryonic antigen antibody internalization: effects of affinity, bivalency, and stability. *Cancer Immunology Immunotherapy* **57**, 1879–1890 (2008).
21. Rhoden, J. J. & Wittrup, K. D. Dose dependence of intratumoral perivascular distribution of monoclonal antibodies. *Journal of Pharmaceutical Sciences* **101**, 860–867 (2012).
22. Helmlinger, G., Yuan, F., Dellian, M. & Jain, R. K. Interstitial pH and pO₂ gradients in solid tumors in vivo: High-resolution measurements reveal a lack of correlation. *Nature Medicine* **3**, 177–182 (1997).
23. Boucher, Y., Baxter, L. T. & Jain, R. K. Interstitial pressure gradients in tissue-isolated and subcutaneous tumors: Implications for therapy. *Cancer Research* **50**, 4478–4484 (1990).
24. Baxter, L. T. & Jain, R. K. Transport of Fluid and Macromolecules in Tumors I: Role of Interstitial Pressure and Convection. *Microvascular Research* **37**, 77–104 (1989).
25. Chary, S. R. & Jain, R. K. Direct measurement of interstitial convection and diffusion of albumin in normal and neoplastic tissues by fluorescence photobleaching. *Proceedings of the National Academy of Science* **86**, 5385–5389 (1989).
26. Thurber, G. M., Zajic, S. C. & Wittrup, K. D. Theoretic Criteria for Antibody Penetration into Solid Tumors and Micrometastases. *Journal of Nuclear Medicine* **48**, 995–999 (2007).

6. DEVELOPMENT OF AN AUTOCHTHONOUS CEA-EXPRESSING MOUSE MODEL

6.1 Introduction

Mice have been used as model organisms for *in vivo* laboratory research for over one hundred years. Mice are appealing organisms for the study of cancer for many reasons, and the laboratory mouse has become the standard preclinical *in vivo* model system that is used in drug development for cancer. They require little space or food, reproduce relatively rapidly, and are easy to handle. For decades, they have been used to study tumorigenesis, the disposition and trafficking of candidate drugs, and often the *in vivo* efficacy of candidate drugs as a prelude to first-in-human studies.

Early mouse models of cancer used direct administration of carcinogenic compounds to induce tumor formation in mice¹. More recently, advancements in mouse models have led to the development of over 450 different strains of mice which have been bred for specific phenotypic or genotypic characteristics². These strains are often inbred for tens of generations, creating lines of mice which are genetically identical to one another. This has allowed researchers to use the same mouse models regardless of geographical location and has aided reproducibility and translation of research. Some of these inbred models were bred for the study of cancer and were predisposed to certain types of cancer³. Despite these advances in mouse models, the study of cancer in these models continued to be difficult as a consequence of the unpredictable development of tumors in these mice.

A major breakthrough in mouse cancer models was achieved with the advent of immunocompromised mouse models. The first immunocompromised mice to be widely used in cancer studies were athymic, or nude, mice⁴. Since these mice lack a thymus, they fail to develop mature T cells and are unable to mount an effective response against many immune stimuli. Other immunocompromised mouse strains have since been developed, including the widely used severe combined immunodeficient (SCID), which lacks functional T cells and B cells due to a defect in V(D)J recombination⁵. A further step has recently been taken by creating

SCID mice lacking the interleukin-2 receptor, rendering these mice without function B cells, T cells, or natural killer (NK) cells⁶. These immunocompromised mice all are able to accept xenografts of human cancer cells, which in many cases develop into solid tumors at the site of injection into the mouse. Xenografted mice allow many different types of cancer to be studied using *in vivo* hosts which are genetically identical to one another. Today, nearly all cancer therapeutics are tested first in xenografted mice before being tested in humans.

Despite the utility of xenograft mouse models, there remain many difficulties in translating results seen in the context of a mouse xenograft to clinical studies. A recent metastudy of approximately 40 anticancer drugs which were tested in xenograft mice as well as in human clinical trials suggested that less than half of all drugs efficacious in xenograft models were also efficacious in human trials⁷. Xenografted mice are most often used in subcutaneous tumor models in which tumor cells are injected under the skin of the mice. Advantages of this model include a high penetrance rate, accessibility for both tumor cell injection and subsequent measurement of the tumor size, and relatively low technical barrier. However, these models can be crude approximations of clinical tumors (Figure 6.1). They are not clonal in origin, instead originating from thousands to millions of cultured human cell lines, often passaged over tens or hundreds of generations in plastic dishes before being injected. It has been shown that most primary cells are not well propagated *in vitro*, and further that the cells which are successfully propagated and immortalized in tissue culture often lose many of the characteristics of the original host and tumor^{8,9}. Genetically, they are often highly abnormal, and have been shown to change their genetic makeup over time in culture^{10,11}. Finally, these tumor cells are growing in an environment that is in many ways a poor reproduction of a tumor environment. They grow under the skin of a mouse without a properly functioning immune system, and must interact with mouse growth factors, recruit murine vasculature, and in general communicate intercellularly with a murine host. Not surprisingly, xenograft models of cancer have a mixed track record in the context of preclinical drug development.

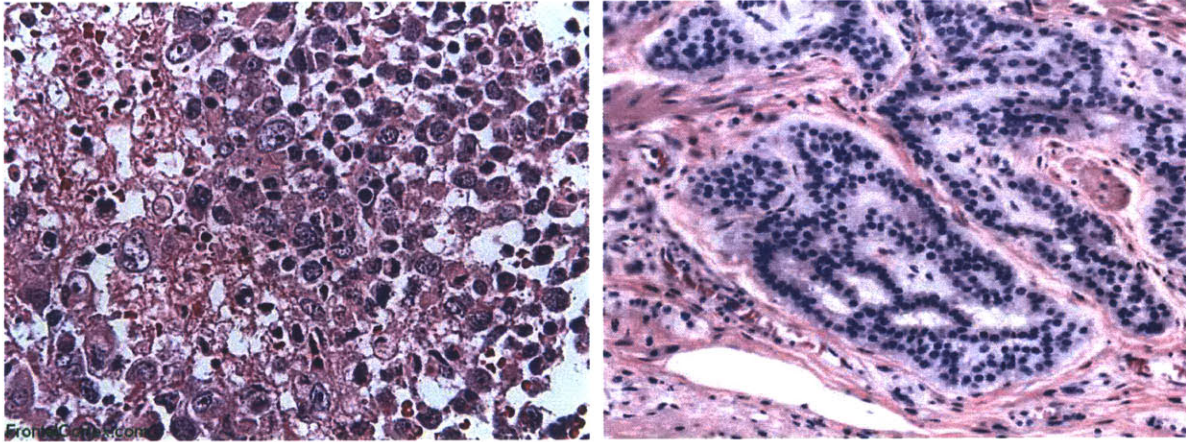


Figure 6.1. At left, an example of a hematoxylin and eosin (H&E) stained xenograft tumor section. Note the homogeneity of the tissue and the lack of secondary structure. At right, an example of a colorectal cancer xenograft. Notice the heterogeneity of the tissue and the distinct presence of secondary structures. Also note that a large fraction of this section is composed on stromal cells, which are often largely absent in xenograft tumors.

There have been many notable failures of drugs which were highly efficacious in mice, but have failed miserably in human trials. The attrition rate of drugs which reach clinical trials is quite high, and various estimates place the attrition rate at 60-95%¹². These drugs were all successful in mouse studies, yet faltered in human studies, raising questions about the ability of xenograft models to capture the fundamental features of the human disease. The high failure rate of clinical compounds which were successful in mouse studies also raises the question of whether promising therapeutics for humans may be overlooked because of poor efficacy in mice. One possible cause of the discrepancy between xenograft mouse models and human trials is the deficient immune system which exists in these mouse models.

In the past several decades, a new generation of mouse models of cancer has been developed, and these models are often fully immunocompetent. These models are genetically engineered to knock out or knock in certain genes which are relevant to the study being conducted¹². For example, knocking out tumor suppressor genes and/or knocking in oncogenes has been shown to lead to tumor formation. Other genes can be tweaked to constitutively activate certain pathways, or to develop mice which lack a certain specific characteristic, for example a particular immune function. Still others can aid in research by activating fluorescence or

inducible markers in response to external stimuli^{13,14}. There has been an explosion in the development of these models in recent years, and they have greatly facilitated the study of the biology and pathology of cancer. Unfortunately, genetically engineered mouse models are often expensive and slow to develop, and this has hindered their development and use in the context of preclinical efficacy evaluation and drug development¹⁵.

In this work, we seek to build upon a previously described genetically engineered mouse model to develop a model which is engineered to express a neoantigen that can be targeted by an antibody^{16,17}. This model of cancer is engineered upon the most common strain of laboratory mouse in the world, the C57BL/6 mouse. The Jacks laboratory has made two modifications to the mouse genome, both of which are activatable upon the administration of the enzyme Cre recombinase. This enzyme can be delivered specifically to certain organs of the mouse by administration of a lentivirus engineered to insert the gene for Cre recombinase into the mouse genome. Upon exposure to Cre recombinase, two events occur. First, the oncogene K-ras with a common mutation (G12D) to confer constitutive activity is activated through the excision of a stop codon preceding it. Second, the tumor suppressor gene p53 is excised from the genome. The mice which possess this genotype are abbreviated KP mice. Constitutive activation of K-ras and loss of p53 function mutations occur commonly in cancer, particularly in the most frequent and most deadly cancer that occurs in humans, lung cancer^{18,19}. The effect of these two mutations is to transform single cells possess a tumorigenic genotype. Over a period of weeks and months, tumors form in the affected organ from a clonal origin, gradually becoming increasingly neoplastic as the tumors develop. The tumors which form are histologically very similar to human tumors and mimic the progression of human tumors. Eventually, all affected mice die of their tumor burden, and to date no therapeutic strategy has been effective in curing a mouse affected by these tumors.

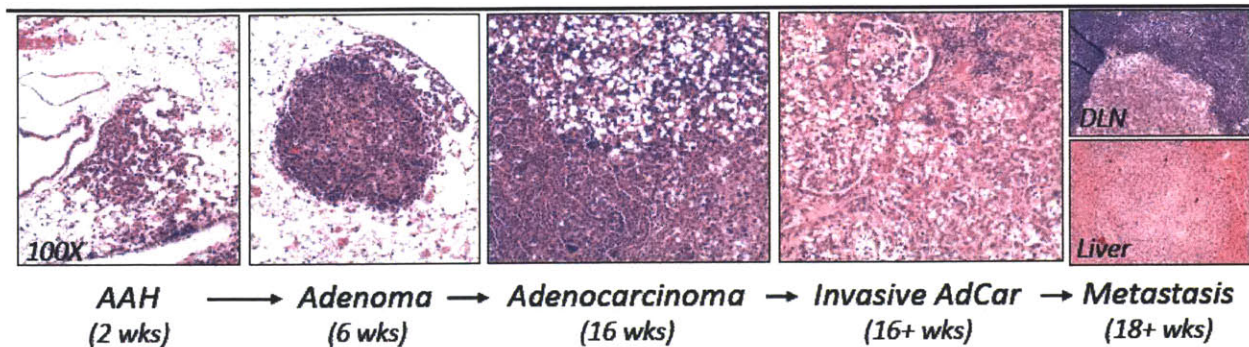


Figure 6.2. H&E staining of lung sections from KP mice at varying time points after viral infection. Tumors form and over time become increasingly aggressive, eventually invading into stromal tissue and even metastasizing. This pathological process is histologically similar to human non-small cell lung cancer. Figure courtesy of Leah Schmidt and adapted from ¹⁶.

The KP mouse model has been used in several studies of cancer biology and tumorigenesis^{17,18,20–25}. It has seen limited use in studies of preclinical anticancer drugs, and KP mice have yet to be cured by any experimental treatment. The tumors which arise lack any known antigen, and so targeted therapies have not been tested on this model because no molecular target is known. We seek to build upon this model by engineering a lentivirus that will induce the expression of Cre recombinase to initiate the tumor, and simultaneously introduce a neoantigen, carcinoembryonic antigen (CEA). The CEA antigen is commonly used in preclinical cancer models and has well-understood biology and structure^{26–33}. It has also been used in numerous preclinical studies, and has been used clinically in settings ranging from use as a biomarker for cancer progression to use as a target antigen for therapeutics in clinical trials^{26,34–37}. We seek to induce CEA-expressing autochthonous tumors in immunocompetent mice to create a next-generation genetically engineered mouse model for use in studying cancer biology and the efficacy of potential targeted therapeutics.

6.2 Materials and methods

Development of lentiviral vectors

Lentiviral transfer vector NLSCre-zsGreen was obtained as a gift from the Jacks laboratory (Cambridge, MA). Using the QuikChange method, full length CEA (2109 bp) and truncated CEA

containing only the sm3e antibody epitope and the GPI linker (~800 bp) were inserted into the transfer vector, replacing the zsGreen sequence³⁸. These constructs were termed lenti-CEA and lenti-CEAfrac, respectively. Two truncated CEA variants were created—the first consisting of the two binding domains making up the sm3e epitope, in addition to the GPI linker, and the second consisting of the same elements joined by a (Gly)₄(Ser) linker to separate the binding site from the cell surface (lenti-CEAfrac and lenti-CEAfrac G4S, respectively). In addition, one other construct was created by excising the woodchuck response element (WRE) from the full-length CEA transfer vector in an attempt to reduce the overall size of the plasmid for enhance virus production. The construct was termed lenti-CEA ΔWRE.

K-ras^{LSL-G12D/+};p53^{fl/fl} mouse preparation and lentivirus injection process

K-ras^{LSL-G12D/+};p53^{fl/fl} (hereafter referred to as KP) mice were obtained as a gift from the Jacks laboratory at M.I.T.(Cambridge, MA). The mice were bred to one another and neonates genotyped to determine the mice possessing the KP genotype. Mice of a similar age with the desired genotype were used in viral administration studies.

Viral administration was conducted as per the protocol described previously by literature published from the Jacks laboratory¹⁶. Briefly, mice were anesthetized by i.p. injection of Avertin (0.4 mg/g). The anesthetized mice were then placed upon an intratracheal delivery platform (Lab Inventions, Newton, MA) and a Fiber-Lite Illuminator (Dolan-Jenner, Boxborough, MA) was positioned against the chest of the mouse to illuminate the chest cavity. Taking care not to scratch or puncture the mouse, a 22 gauge Exel Safelet IV catheter (Fisher Scientific, Pittsburgh, PA) was inserted into the trachea of the mouse. Once inserted, a 50 µl of solution of 25,000 infectious viral particles in serum-free Dulbecco's Modified Eagle Medium (Life Sciences, Grand Island, NY) was administered through the catheter. The catheter was then removed and the mouse allowed to recover under a heat lamp until conscious. Infected mice were returned to their cages and monitored at least twice weekly during the course of the experiment.

Lentivirus production process

Lentivirus was produced in human embryonic kidney 293FT (HEK293FT cells) acquired from Life Sciences (Grand Island, NY). HEK293FT cells were cultured in supplemented Dulbecco's Modified Eagle Medium (DMEM) as per the manufacturer's instructions. Cells were plated onto large diameter 15 cm cell culture plates for virus production and grown to approximately 50% confluency on the day of transfection. On the day of transfection, the cells were transfected using polyethylenimine (PEI), and transfer vector, packaging vector $\Delta 8.9$, envelope vector VSV-G, and pAdvantage translation enhancement vector (all gifts from the Chen or Jacks laboratories at M.I.T.) in a 2:1:1:1 ratio of 10 μg transfer vector and 5 μg of all other vectors. Briefly, 60 μl of 1 mg/mL 25,000 MW PEI (Polysciences, Warrington, PA) was added to 540 μl OptiPro (Life Sciences). Then, DNA in the quantities and ratios above were added to a second tube of 600 μl OptiPro media. The tubes were incubated in a biosafety cabinet for 5-10 minutes at room temperature, then the contents of the DNA tube were added to the PEI tube. The combined mixture was incubated 10 minutes at room temperature, then added dropwise to the 15 cm plate of HEK293FT cells. Cells were incubated 6-12 hours with the transfection reagents, then the media was changed and replaced with supplemented media free of DNA and transfection reagents. At 48 hours following transfection, the supernatant (20 mL of media) was collected, filtered through a 0.45 μm syringe filter, and refrigerated. Fresh media was added to the plate, and at 72 hours this media was also collected, 0.45 μm filtered, and added to the first supernatant. The pooled supernatant contains viral particles, and was spun in an ultracentrifuge at 25,000 rpm for 2 hours at 4°C. The supernatant was aspirated, and the viral pellet resuspended in 400 μl PBS and incubated overnight at 4°C. The virus was next titered for activity on 3TZ reporter cells.

Titration to determine lentivirus activity

To determine the activity of the viral supernatant, the 3TZ reporter cell line was used for titrations of the virus. This cell line contains a lox-conditional LacZ/ β -Gal gene, and if infected by a Cre recombinase-expressing virus undergoes activation of the LacZ gene. The day before the titration, the 3TZ cells (Jacks laboratory, M.I.T., Cambridge, MA) were plated onto 6-well

plates at 1×10^5 cells/well. The next day, dilutions of virus were added to the wells of the 6-well plate in duplicate at 1:100, 1:1000, and 1:10000 ratios. Virus was incubated 24 hours, then the media replaced by fresh media. At 48 hours following infection, the media was aspirated and the cells washed with PBS. The cells were then fixed for 10 min with 3.6% formaldehyde (Sigma Aldrich, St. Louis, MO) in PBS. The wells were then washed 3 times with PBS, and X-Gal solution was added to cells and incubated overnight in a 37°C incubator. X-Gal solution consists of 10 mL PBS, 250 μ L 20x $K_3Fe(CN)_6/K_4Fe(CN)_6$, 400 μ L X-Gal stock solution, and 20 μ L 1M $MgCl_2$. The X-gal stock solution is composed of 25 mg/ml X-gal in N,N-Dimethylformamide, stored at -20°C. The 20x $K_3Fe(CN)_6/K_4Fe(CN)_6$ is composed of 3.292g $K_3Fe(CN)_6$ +4.224g $K_4Fe(CN)_6$ +100ml PBS, stored at 4°C in a foil-wrapped container protected from light

Micro computed tomography for in vivo imaging of lung tumors

Mice were imaged on an eXplore CT120 whole mouse microCT (GE Healthcare, Waukesha, WI) every two weeks beginning at 10 weeks post infection. The imaging protocol used was “soft tissue fast scan”, a protocol balancing image resolution and radiation exposure. Imaging parameters were as follows: 220 views, 0.877° increment angle, 70.0 kV X-ray tube, 50.0 mA X-ray tube current, 2x2 binning, 32 ms exposure time, 130 gain, and 20 offset. Once images were acquired, reconstruction was performed on the region containing the lungs and images saved for analysis with ImageJ software (National Institutes of Health, Bethesda, MD).

Treatment with interleukin 2-Fc + anti-CEA antibody

Beginning at 14 weeks post-infection, one mouse in the lenti-X group and one mouse in the lenti-CEAfrac group was treated with an experimental immunocytokine therapy. This therapy consisted of 25 μ g of interleukin-2 fused to a murine IgG2a Fc domain coadministered with 100 μ g of high affinity sm3e anti-CEA antibody with a murine IgG2a backbone. Both constructs were administered in approximately 50 μ L of PBS weekly into the mouse via retroorbital injection. When possible, injections were conducted at the same time, but spatially separated by injecting each construct into a different eye of the mouse. Weekly injections continued for 14 weeks or until death of the mouse.

Detection of anti-CEA antibodies in serum of KP mice

Biotin binder Dynabeads from Life Sciences (Grand Island, NY) were prepared as per the manufacturer's instructions. Human CEA purified from colon carcinoma was acquired from Fitzgerald Industries (Acton, MA) and biotinylated using Pierce EZ-Link Sulfo-NHS-Biotin reagent (Thermo Fisher Scientific Inc, Rockford, IL) according to the manufacturer's protocol.

Biotinylated CEA was thoroughly desalted by passage twice through 7 kDA MWCO Zeba desalting columns (Thermo Fisher Scientific). Then, 2.5 µg of biotinylated CEA was incubated with 2×10^7 biotin-binder Dynabeads for 1 hour at room temperature on a rotator, then washed twice in PBS and resuspended at a density of 200,000 beads/µl.

To detect anti-CEA antibodies, 200,000 CEA coated beads were incubated with serum dilutions (1:10 or higher) or controls for one hour or more at room temperature on a rotator. Beads were then washed twice with PBS+0.1% albumin (PBSA) and resuspended in 100 µl PBSA. Anti-mouse secondary conjugated to Alexa Fluor 488 (Life Sciences) was added at a 1:200 dilution and incubated 30 minutes at 4°C on a rotator. Beads were washed twice with PBSA, and finally resuspended in 100 µl PBSA and kept on ice until running on an Accuri C6 cytometer (BD Biosciences, San Jose, CA).

Histology and immunodetection of CEA

Mice were sacrificed by CO₂ asphyxiation. Immediately following euthanasia, four of the five lobes of the lungs, draining lymph nodes, spleen, kidneys, liver, and heart were removed, fixed 12-24 hours in 3.6% formaldehyde in PBS, and stored in 70% ethanol until being paraffin embedded by the Koch Institute Histology Core Facility. The fifth lobe of the lungs was removed, embedded in Tissue-Tek optimal cutting temperature (OCT) media (Sakura Finetek, Torrance, USA), and flash frozen in isopentane over liquid nitrogen. Frozen tissue was stored at -80°C until being sectioned by the Koch Institute Histology Core Facility at 6 µm thickness and kept at -80°C until use. Paraffin-embedded sections were sectioned by the facility at 5 µm thickness and kept at room temperature until use. For most tissues, one slide was hematoxylin and eosin stained for analysis of tissue morphology and pathology.

For immunohistochemical detection of CEA, lung sections were dewaxed, rehydrated, and then fixed for 10 minutes in 3.6% formaldehyde in PBS. Sections were washed with water, then boiled for 10 minutes in 10 mM sodium citrate, pH 6.0, for antigen retrieval. Slides were allowed to cool at room temperature for 20 minutes, then washed three times in water. Slides were blocked with 1% hydrogen peroxide in water for remove endogenous peroxide activity. A MaxTag Histo IHC kit (Rockland Immunochemicals, Gilbertsville, PA) was used according to the manufacturer's protocol for IHC staining using the human anti-CEA antibody sm3e as the primary antibody at a 1:2000 dilution. Slides were imaged using a Zeiss upright microscope.

An immunofluorescence protocol was applied to frozen lung samples to detect the presence of human antibody through human Fc and the detection of CEA on the cell surface. Anti-CEA monoclonal antibody M85151a was purchased from Fitzgerald (Acton, MA) and goat anti-rat 546 secondary antibody from Life Sciences. Antibody M85151a was labeled with an Alexa Fluor 647 Protein Labeling kit and has been previously determined to be noncompetitive with sm3e³³. Tissues were fixed for 15 minutes at room temperature in formalin, then washed 3 times with PBS. Blocking was performed with 5% goat serum (Invitrogen) in PBS for 1 hour at room temp. Primary antibody incubation was 5% goat serum in PBS + 1:100 rat anti-mouse CD31 (BD Pharmingen, San Diego, CA) overnight at 4°C. Slides were then washed three times with PBS, then incubated with PBS+0.1% Tween 20 (Sigma-Aldrich, St. Louis, MO) + 1:200 goat anti-rat 546 (Invitrogen, Carlsbad, CA) + 1:100 M85151a-647 anti-CEA antibody (Fitzgerald, Acton, MA) for 1 hour at room temperature. Slides were washed 4 times with PBS, then mounted in Vectashield + DAPI medium (Vector Labs, Burlingame, CA). Slides were allowed to set a minimum of 12 hours and imaged on a DeltaVision fluorescence microscope.

6.3 Results

Production of CEA-inducing lentivirus

Lentivirus production is a strong function of the size of the transfer vector³⁹, and CEA is a large neoantigen to be inserted into the transfer vector at approximately 2100 bases. In comparison, other neoantigens used in the KP mouse model include luciferase^{20,21} (~1700 bp) and green

fluorescent protein (personal communication with Leah Schmidt, Jacks lab) (~800 bp). The smallest KP transfer vector, contained only Cre recombinase and no neoantigen and termed lenti-X, has a high viral titer, but the addition of transgenes drops the viral titer substantially. The first step in the development of a robust CEA-expressing KP mouse model was to determine whether virus encoding both Cre and CEA (lenti-CEA virus) can be produced in sufficiently high titers. To examine this, lenti-X, lenti-GFP (expressing Cre recombinase and GFP) and lenti-CEA viruses were produced as described earlier and titrated on 3TZ reporter cells. The results are shown in Figure 6.3 below.

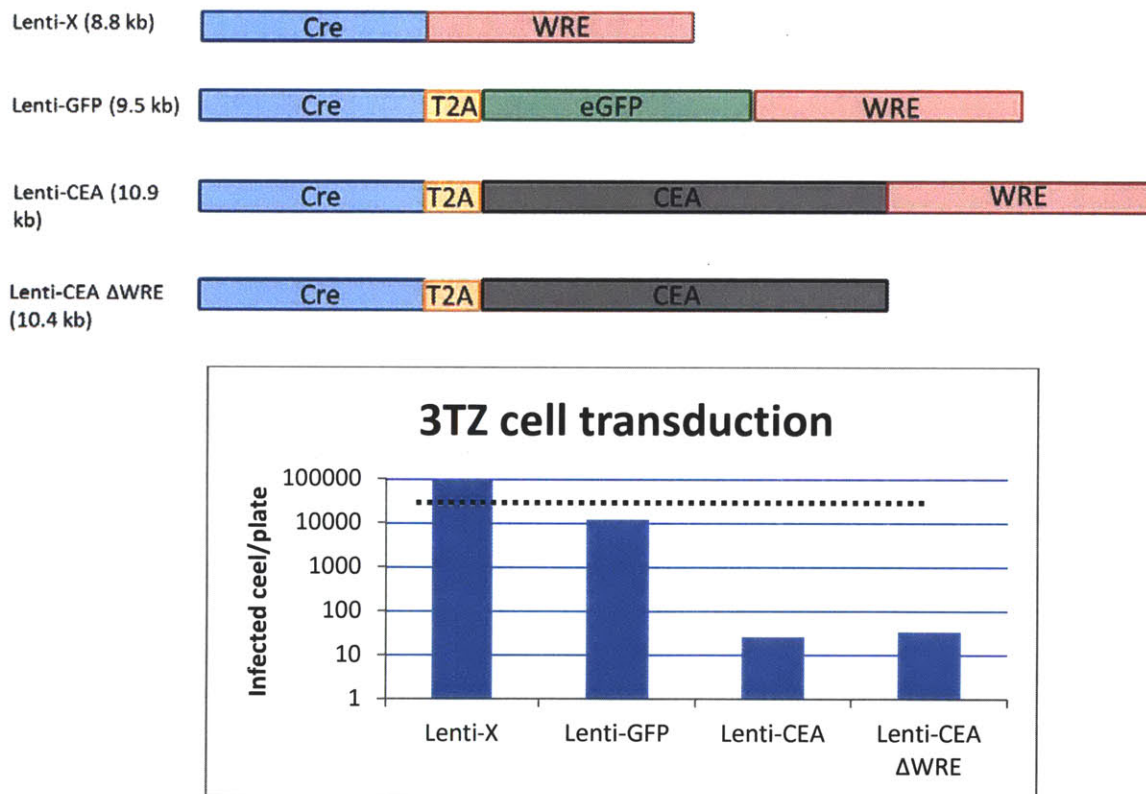


Figure 6.3. At top, schematic illustrations of the various lentiviral transfer vectors used. Lenti-X is the smallest construct and contains only Cre recombinase, while all the others contain Cre in addition to a transgene. Lenti-CEA Δ WRE contains full length CEA but excises the woodchuck response element (WRE) to decrease the total size of the insert. At bottom, titration results with each of the four viral vectors on 3TZ reported cells. Data are shown as number of infected 3TZ cells per plate of virus produced. Dotted line represents the number of infections required to infect a single mouse.

For the smaller constructs, such as the minimalist lenti-X and the relatively small lenti-GFP, transduction efficiency is good and titration results indicate that several plates of virus

production would allow the production of enough virus to infect multiple mice at the recommended dose of 25000 infectious particles per mouse.. However, the lenti-CEA construct is over 2 kb larger than lenti-X, and the result is production of more than three orders of magnitude less infectious virus. Removal of the WRE element had little effect on the viral titer, perhaps because the WRE has been shown to improve viral translation, and so perhaps the decreased vector size was offset by reduced translational efficiency⁴⁰.

To address this issue, additional transfer vectors were created of a reduced size, but containing the sm3e epitope of CEA. The CEA antigen is a long, rod-like protein consisting of a glycosylphosphatidylinositol (GPI) linker and seven immunoglobulin domains^{26,29,41}. The binding site for sm3e has been mapped to a location between the first and second immunoglobulin domains farthest from the GPI linker^{26,42}. Based on this data, a truncated version of CEA was created consisting of the two immunoglobulin domains comprising the antibody binding domain conjugated to the GPI linker domain. An additional vector was created with the addition of 2 (Gly)₄(Ser) spacers between the immunoglobulin domains and the GPI linker to provide a flexible linker to separate the binding domain from the cell surface and reduce the potential for steric hindrance. Both these truncated versions of CEA measure approximately 800 base pairs in length, reducing the size of the transfer vector approximately 1300 base pairs relative to the full length CEA and bringing them into the same size range as lenti-GFP. Complete sequences for these vectors are provided in Appendix B. Once created, these vectors were transfected into HEK293FT cells and virus produced and the transfected HEK cells checked for binding against Alexa Fluor 488 labeled sm3e, then run on an Accuri C6 flow cytometer to determine whether the fractional CEA retained the sm3e epitope while on the cell surface. Results are summarized in Figure 6.4 below.

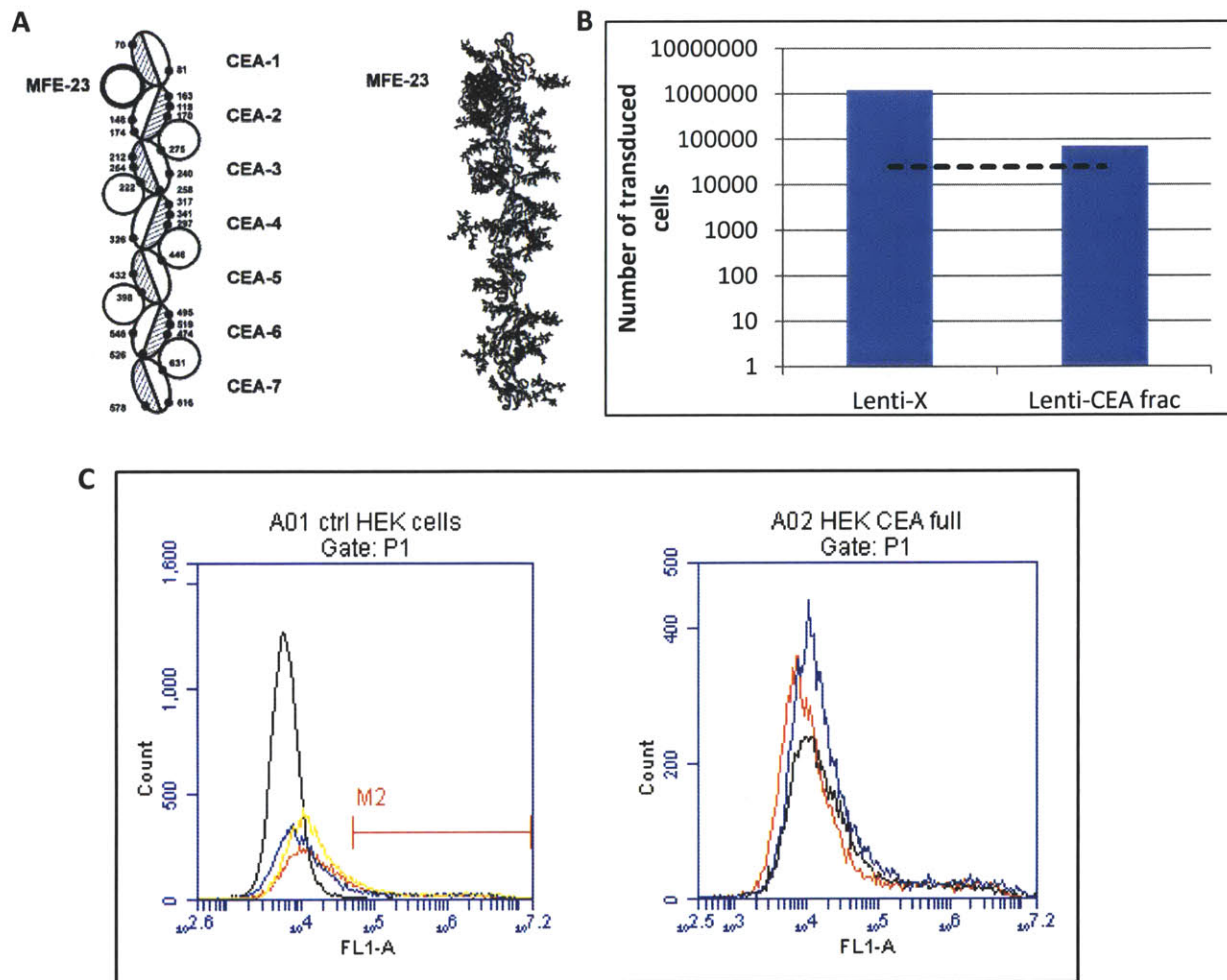


Figure 6.4. Validation of anti-CEA antibody binding to fractional CEA constructs. A, cartoon of CEA structure and sm3e antibody binding pocket from ⁴². B, 3TZ reporter cell titration results demonstrating that fractional CEA is produced by HEK293FT cells at levels sufficient for infecting mice (black dotted line, amount of virus need per mouse). C, flow cytometric analysis of HEK293FT cells for determination of antibody binding to fractional CEA. Transfected HEK cells were incubated with Alexa 488-labeled sm3e and run on flow. Left panel, black is negative control (untransfected HEK cells), red is full length CEA, blue is fractional CEA, and yellow is fractional CEA with G4S linker. Right panel, direct comparison of the three CEA constructs. Note that there is no discernible difference in the antibody binding between the three. In all cases, transfection efficiency was approximately 20%.

The truncated CEA transfer vector results in the production of more than 10 fold less virus than lenti-X, but several orders of magnitude more than lenti-CEA. More importantly, the titer of the truncated CEA is in the range such that a single plate of transfected HEK cells results in enough virus to infect one or more mice, making the production of virus by this method feasible even for relatively large cohorts of mice. The virus produced was used to infect a cohort of five KP

mice, three of which received 25,000 infectious particles of lenti-CEAfrac G4S and two of which received 25,000 infectious particles of control virus lenti-X.

Evaluation of lung tumor development in vivo

The tumors which are induced by viral infection are expected to be localized to the site of viral administration, in this case the lungs. To track lung tumor development and tumor burden, micro computed tomography (μ CT) was utilized beginning 10 weeks post-infection. This technique has proven effective in imaging KP mouse tumors and tracking tumor burden longitudinally²². By this method, tumors of a size of approximately 1 mm in diameter can be detected (Figure 6.5).

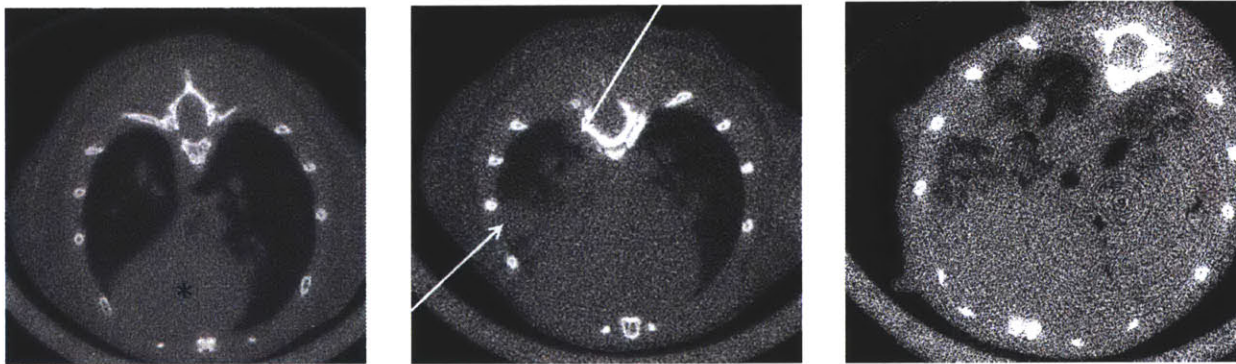


Figure 6.5. Representative μ CT images of KP mouse lungs. At left, a lung with no detectable tumors. The large white object marked with an asterisk (*) is the heart. Center, a lung with several detectable tumors, marked with white arrows. Right, the lungs of a mouse with advanced lung cancer and many tumor nodules. This mouse was euthanized due to morbidity from tumor burden approximately one week following this image.

By tracking the progression of the tumors in the five mice infected with lentivirus, it was possible to track the development of tumors and the tumor burden over time. The first evidence of tumors detectable by μ CT occurred at approximately 12 weeks post-infection. Treatment with Fc-IL2 + murine sm3e began in two mice (one lenti-X and one lenti-CEA) during week 11. The three untreated mice all exhibited evidence of small (~1 mm diameter) tumor nodules evident in μ CT scans by week 16. However, the treated mice failed to show evidence

of tumors until much later—no tumors were evident at the time of the death of the treated lenti-X mouse (week 19), and only very small tumors were apparent at week 26 in the treated lenti-CEA mouse. Fc-IL2 treatment of this mouse continued for 14 consecutive weeks beginning with week 11 before being discontinued.

Tumor size was qualitatively assessed through the biweekly μ CT scans. While only one control mouse was used in this study, this mouse developed tumors visible to μ CT scans first and continued to develop a large tumor burden until being euthanized due to tumor burden at week 24. The two lenti-CEA mice that did not receive Fc-IL2 + murine sm3e treatment both developed visible tumor nodules just a few weeks after the control mouse, but the rate of tumor growth was considerably slower and no mice died until one was euthanized to test for the presence of CEA at week 25. The remaining lenti-CEA mouse exhibited continued tumor growth by μ CT through 32 weeks, at which point the mouse possessed a moderate tumor burden.

The CEA protein is not found endogenously in mice, and so its introduction into an immunocompetent mouse model such as the KP model could cause an immune response against the antigen as has been observed with several canonical immunogens in the past^{20,21,43}. In this case, the CEA protein might fail to be expressed through immunoediting, allowing the tumor to grow out without expressing the desired antigen. To determine whether CEA was expressed in tumors generated in lenti-CEA mice, we first checked whether an immune response was raised against CEA by testing the serum of mice infected with lenti-CEA for the presence of circulating anti-CEA antibodies. Beads coated with full length CEA were incubated in the serum of lenti-CEA mice and controls, and the results are summarized in Figure 6.6. For all lenti-CEA mice, anti-CEA antibodies were detected at levels well above background, while anti-CEA antibodies were absent in all lenti-X mice and uninfected control mice.

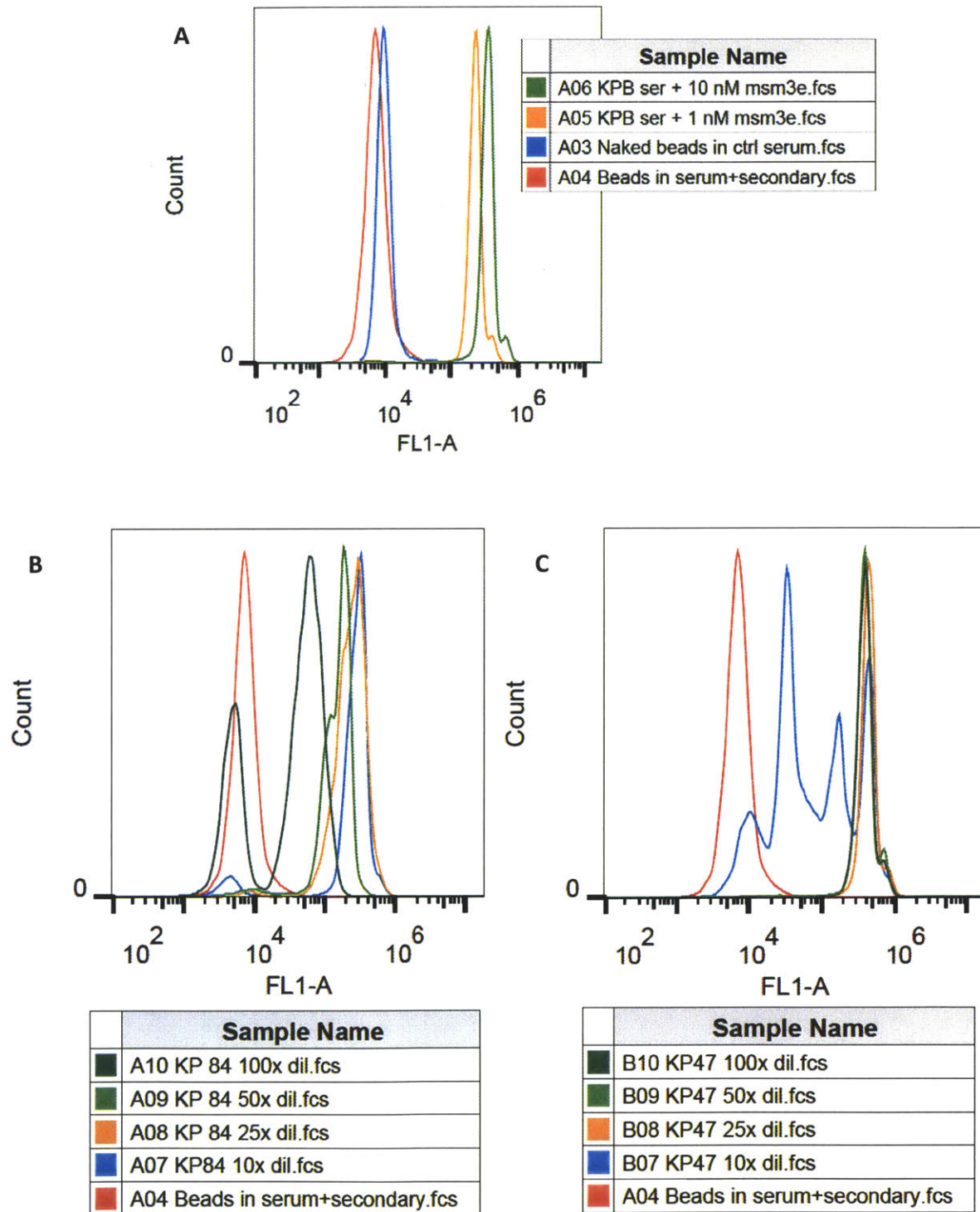


Figure 6.6. Flow cytometric testing for the presence of anti-CEA antibodies in the serum of control and lenti-CEAfrac G4S mice. The presence of antibodies bound to CEA-coated beads was determined using a 488-labeled anti-mouse antibody. A, control mouse showing no antibodies present in the serum and a 2-3 log shift upon spiking anti-CEA antibody (m-sm3e). B and C, two different lenti-CEAfrac G4S mice showing the presence of antibodies even at 1:100 dilutions of the serum.

Following the death due to tumor burden of the lenti-X control mouse, one of the lenti-CEA mice with clear tumor nodules measuring 1-2 mm diameter by μ CT was euthanized and the lungs excised for histological analysis. The lenti-X control mouse was subjected to similar histological analysis following euthanasia. These tumor sections were analyzed with H&E staining to examine and confirm tumor pathological characteristics (Figure 6.7). Examination of the lenti-X and lenti-CEA tumors showed that the tumors had pathological characteristics similar to human non-small cell lung cancers as has previously been observed for KP mice¹⁶. The lenti-CEA tumors showed a much greater degree of lymphocyte infiltration into the tumor, particularly at the tumor periphery, than the lenti-X tumors. By pathological grade, the lenti-X lung tumors were mostly grades 2 and 3, with several tumors potentially grade 4 and showing evidence of invasion into surrounding tissue and potentially metastasizing, although no metastases were observed in the mouse. The lenti-CEA tumors were lower grade, grades 1 and 2 with at least one grade 3 tumor, consistent with the decreased tumor burden at the time of the mouse's euthanasia.

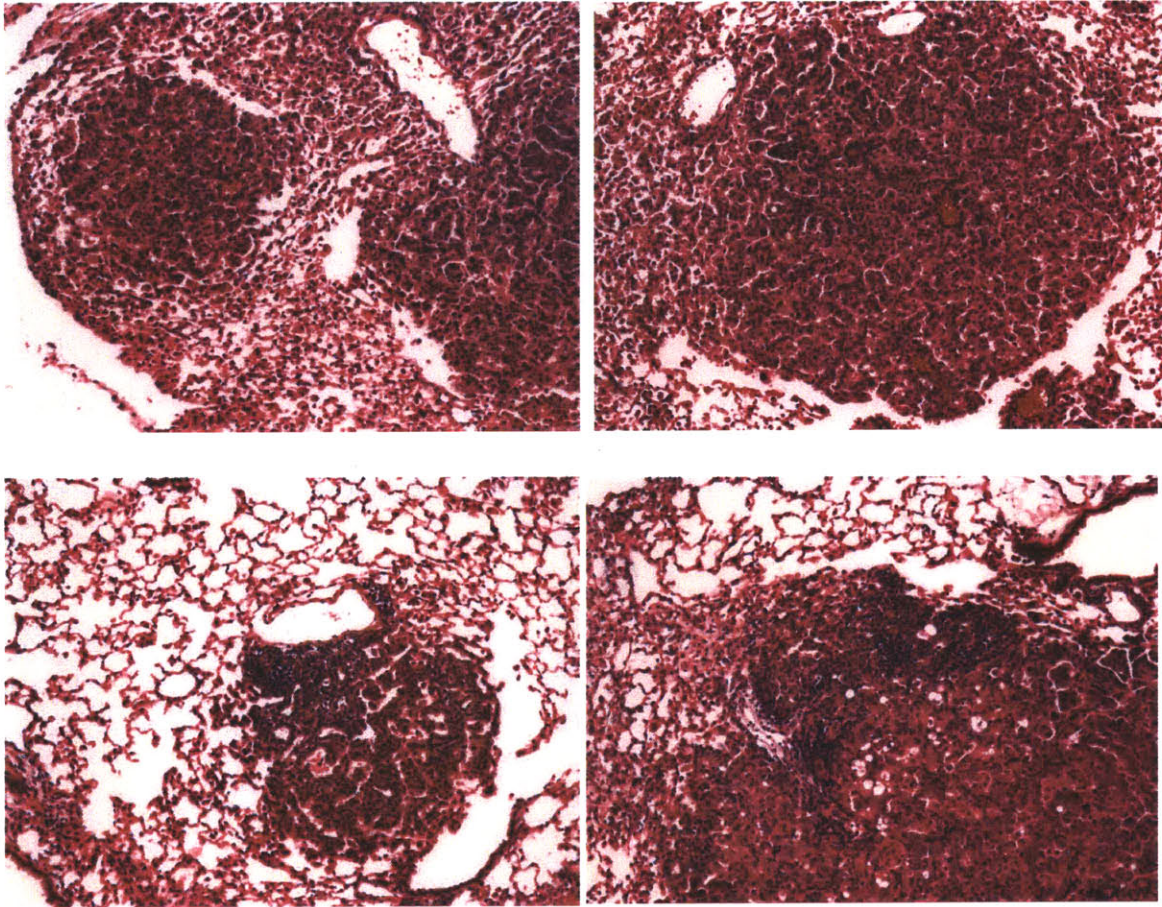


Figure 6.7. H&E stained lung sections from lenti-X (top panels) and lenti-CEAfrac G4S (bottom panels). Several tumors of varying size and grade are shown. Histology is similar to that seen in previous KP tumors and mimics the histology of human non small cell lung cancer. Note the large numbers of tumor infiltrating lymphocytes which are seen in the lenti-CEAfrac G4S tumors (bottom panels) but at a much lower frequency in the lenti-X controls.

Sections of the lenti-X and lenti-CEA lungs, along with sections of xenograft tumors known to express CEA, were subjected to immunohistochemistry in an attempt to detect the presence of cell surface antigen recognized by the sm3e antibody (Figure 6.8). CEA expression was confirmed in the LS174T and HT-CEA tumor sections, which are known to express approximately 4×10^5 and 1×10^6 CEA molecules/cell *in vitro*^{33,44}. However, no evidence of cellular CEA expression was observed on either lenti-X control tissue or lenti-CEA tissue.

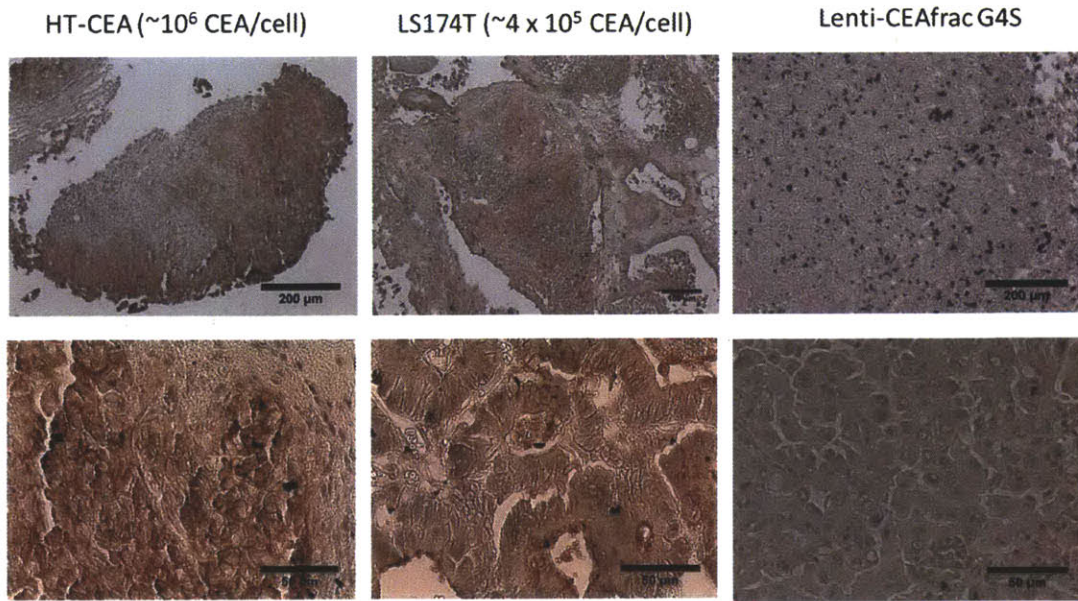


Figure 6.8. Immunohistochemistry to detect the presence of CEA on tissue sections. Images are shown at 10x magnification (top row) and 40x magnification (bottom row). Two positive control tumors, HT-CEA (10⁶ CEA/cell) and LS174T (4x10⁵ CEA/cell), were stained for comparison with tumor-bearing lenti-CEAfrac G4S tissues. The presence of cell –surface CEA is apparent in the positive control tumors, but results are ambiguous in the lenti-CEAfrac G4S tissue.

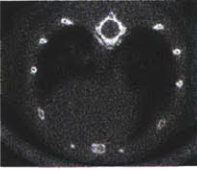
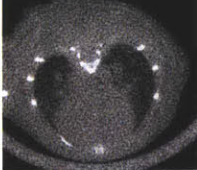
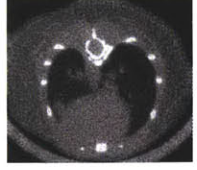
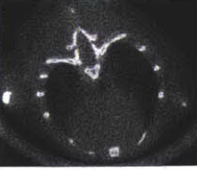
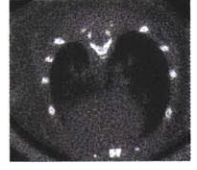
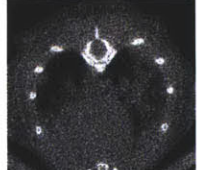
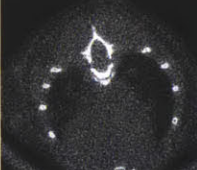
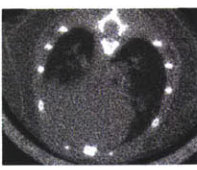
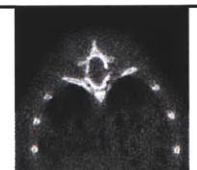
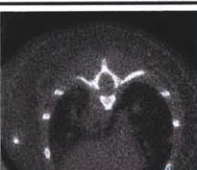
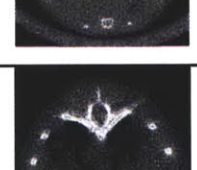
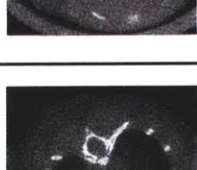
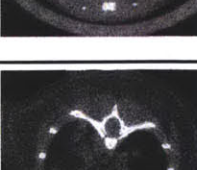
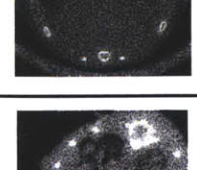
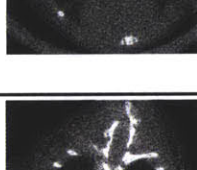
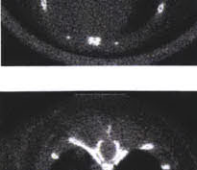
6.4 Discussion

Thus far in the development of an autochthonous CEA-expressing immunocompetent mouse model, only one control mouse and one putative CEA-expressing mouse has been histologically examined. The histological data are inconclusive regarding the presence of CEA in this model (Figure 6.8). Although immunohistochemistry did not demonstrate the presence of the antigen, it is possible that expression is present but low and under the detection limit for this IHC protocol.

However, the presence of anti-CEA antibodies in the serum of mice infected with virus containing CEA (Figure 6.6) is highly suggestive of successful induction of CEA expression at some point during the experiment. Antibodies are present at relatively high titers, as indicated by the relative lack of decreased signal even at high (1:100) dilution of serum. At this point, the possibility that the antibodies might be raised in response to residual CEA protein in the viral supernatant cannot be ruled out. Although the supernatant is centrifuged at 25,000 rpm for 2 hours to pellet virus, it is feasible that small amounts of CEA persist and that the virus acts as a powerful adjuvant to drive an anti-CEA immune response to the dosed CEA. However, the fact that the lung is generally an immunosuppressive environment would argue against such a strong response. In addition, the histological differences between lenti-CEAfrac and lenti-X tumors, in particular the dramatically enhanced lymphocyte infiltration into the putative antigen expressing tissue, suggest that the antigen may be or have been present at some level. Low levels of antigen could be caused by immunoediting as infected cells downregulate their CEA expression in an effort to circumvent the immune response. This phenomenon has recently been observed clinically as a method of resistance in breast cancer patients undergoing treatment with the monoclonal antibody trastuzumab⁴⁵.

Ultimately, with just one control and one lenti-CEAfrac G4S mouse, it is not possible to draw definitive conclusions. However, it can be said that the available data are promising and suggest that antigen expression is achieved during the tumorigenesis process. This also has the effect of slowing the tumor growth rate; all three lenti-CEAfrac tumors outlived the lenti-X controls, several of them by months. Assuming that lenti-CEAfrac mice do express CEA but that the

expression level is low as evidenced by IHC, then several approaches can be taken to try to enhance CEA expression to make antigen targeted therapies more practical. At the molecular level, versions of CEA could be engineered to retain antibody binding but knock out immune epitopes, potentially allowing the CEA to better escape immune surveillance. Ultimately, however, a far superior method would be to engineer a mouse model which expresses CEA endogenously. Such a model would mimic the human condition, and would be tolerized to CEA expression. Mice which express CEA endogenously do exist, and making a KP version of these mice would be a matter of several rounds of breeding between KP and endogenous CEA mice⁴⁶.

Weeks post-infection	Lenti-X	Lenti-CEAfrac G4S mouse 1	Lenti-CEAfrac G4S mouse 2
10			
12			
14			
16			
18			
20			

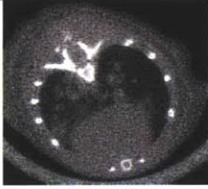
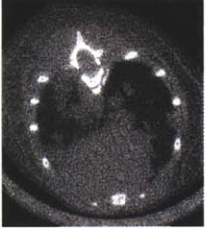
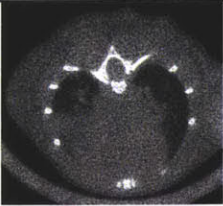
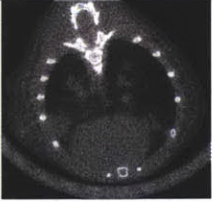
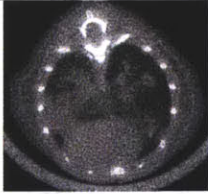
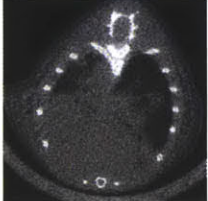
22			
24	Euthanized due to tumor-associated morbidity		Euthanized for CEA detection
26	Euthanized in week 24		Euthanized in week 24
28	Euthanized in week 24		Euthanized in week 24
30	Euthanized in week 24		Euthanized in week 24
32	Euthanized in week 24		Euthanized in week 24

Figure 6.9. Longitudinal μ CT imaging of the lungs of KP mice to track tumor burden and growth rate. Note the difference in the time at which tumors are detected and the rate at which tumors grow and develop between lenti-X and lenti-CEAfrac G4S mice.

Lung models of cancer present a difficulty in determining tumor burden. The KP mouse model is especially problematic because the rate of tumorigenesis can be variable. In this work, μ CT was used as a non-invasive method to semi-quantitatively monitor tumor development and tumor burden in the mice (Figure 6.9). While limited in its resolution to lesions greater than ~ 1 mm in size, μ CT is a relatively rapid, inexpensive, and reproducible method of monitoring these mice. There is the potential of considerably increasing the resolution and contrast of μ CT imaging by using techniques such as respiratory gating or the use of contrast agents.

Respiratory gating synchronizes image acquisition with the breathing of the mouse so that images are acquired at a consistent point in the breathing of the mouse. This reduces the noise associated with the movement of internal organs as the mouse breaths, but increase the time required to image the mice several fold. Alternatively, blood pool contrast agents can dramatically enhance contrast and help to delineate the organs, particularly the heart, which are often in the same field of view as the lung and tumor tissue. Contrast agents do place an additional stress on the animals, and so repeated or frequent use of these agents may not be feasible⁴⁷.

Another option for monitoring tumor burden would be to use a serum marker. These have proven useful in clinical situations, and in many cases serum concentrations of markers are leading indicators of tumor progression^{36,48}. Unfortunately, no such marker is known in the KP mouse model. Potential markers include molecules known to be upregulated in many tumors, such as cytokines and growth factors. A search for such a marker might yield a candidate which could serve as a surrogate marker for tumor burden and might allow the detection and quantitation even for small lesions which are under the detection limit of μ CT technologies.

6.5 References

1. Corbett, T. H., Griswold, D. P., Roberts, B. J., Peckham, J. C. & Schabel, F. M. Tumor Induction Relationships in Development of Transplantable Cancers of the Colon in Mice for Chemotherapy Assays, with a Note on Carcinogen Structure. *Cancer Res* **35**, 2434–2439 (1975).
2. Beck, J. A. *et al.* Genealogies of mouse inbred strains. *Nature Genetics* **24**, 23–25 (2000).
3. Demant, P. Cancer susceptibility in the mouse: genetics, biology and implications for human cancer. *Nat. Rev. Genet.* **4**, 721–734 (2003).
4. Povlsen, C. O. & Rygaard, J. Heterotransplantation of human epidermoid carcinomas to the mouse mutant nude. *Acta Pathol Microbiol Scand A* **80**, 713–717 (1972).
5. Bosma, M. J. & Carroll, A. M. The Scid Mouse Mutant: Definition, Characterization, and Potential Uses. *Annual Review of Immunology* **9**, 323–350 (1991).
6. Shultz, L. D. *et al.* Human lymphoid and myeloid cell development in NOD/LtSz-scid IL2R gamma null mice engrafted with mobilized human hemopoietic stem cells. *J. Immunol.* **174**, 6477–6489 (2005).
7. Kelland, L. R. 'Of mice and men': values and liabilities of the athymic nude mouse model in anticancer drug development. *European Journal of Cancer* **40**, 827–836 (2004).
8. Farrell, T. M., Pettengill, O. S., Longnecker, D. S., Cate, C. C. & Cohn, K. H. Growing colorectal tumors: minimizing microbial and stromal competition and assessing in vitro selection pressures. *Cytotechnology* **34**, 205–211 (2000).
9. Peyton Hughes, Damian Marshall, Yvonne Reid, Helen Parkes & Cohava Gelber The costs of using unauthenticated, over-passaged cell lines: how much more data do we need? *Biotechniques* **43**, 575–586 (2007).
10. Masramon, L. *et al.* Genetic instability and divergence of clonal populations in colon cancer cells in vitro. *J. Cell. Sci.* **119**, 1477–1482 (2006).
11. Gibas, Z., Becher, R., Kawinski, E., Horoszewicz, J. & Sandberg, A. A. A high-resolution study of chromosome changes in a human prostatic carcinoma cell line (LNCaP). *Cancer Genetics and Cytogenetics* **11**, 399–404 (1984).
12. Sharpless, N. E. & DePinho, R. A. The mighty mouse: genetically engineered mouse models in cancer drug development. *Nature Reviews Drug Discovery* **5**, 741–754 (2006).
13. Weissleder, R. & Pittet, M. J. Imaging in the era of molecular oncology. *Nature* **452**, 580–589 (2008).
14. Green, J. E. & Hudson, T. The promise of genetically engineered mice for cancer prevention studies. *Nature Reviews Cancer* **5**, 184–198 (2005).

15. Becher, O. J. & Holland, E. C. Genetically Engineered Models Have Advantages over Xenografts for Preclinical Studies. *Cancer Res* **66**, 3355–3359 (2006).
16. DuPage, M., Dooley, A. L. & Jacks, T. Conditional mouse lung cancer models using adenoviral or lentiviral delivery of Cre recombinase. *Nat Protoc* **4**, 1064–1072 (2009).
17. Jackson, E. L. *et al.* Analysis of lung tumor initiation and progression using conditional expression of oncogenic K-ras. *Genes and Development* **15**, 3243–3248 (2001).
18. Johnson, L. *et al.* Somatic activation of the K-ras oncogene causes early onset lung cancer in mice. *Nature* **410**, 1111–1116 (2001).
19. American Cancer Society *Cancer Facts and Figures 2012*. (2012).
20. DuPage, M., Mazumdar, C., Schmidt, L. M., Cheung, A. F. & Jacks, T. Expression of tumour-specific antigens underlies cancer immunoediting. *Nature* **482**, 405–409 (2012).
21. DuPage, M. *et al.* Endogenous T Cell Responses to Antigens Expressed in Lung Adenocarcinomas Delay Malignant Tumor Progression. *Cancer Cell* **19**, 72–85 (2011).
22. Kirsch, D. G. *et al.* Imaging primary lung cancers in mice to study radiation biology. *Int. J. Radiat. Oncol. Biol. Phys.* **76**, 973–977 (2010).
23. Jackson, E. L. *et al.* The differential effects of mutant p53 alleles on advanced murine lung cancer. *Cancer Research* **65**, 10280–10288 (2005).
24. Kissil, J. L. *et al.* Requirement for Rac1 in a K-ras-induced lung cancer in the mouse. *Cancer Research* **67**, 8089–8094 (2007).
25. Young, N. P. & Jacks, T. Tissue-specific p19Arf regulation dictates the response to oncogenic K-ras. *Proceedings of the National Academy of Sciences* **107**, 10184–10189 (2010).
26. Boehm, M. K. & Perkins, S. J. Structural models for carcinoembryonic antigen and its complex with the single-chain Fv antibody molecule MFE23. *FEBS Letters* **475**, 11–16 (2000).
27. Chan, C. H. F. & Stanners, C. P. Recent advances in the tumour biology of the GPI-anchored carcinoembryonic antigen family members CEACAM5 and CEACAM6. *Current Oncology* **14**, 70–73 (2007).
28. Slayter, H. S. & Coligan, J. E. Electron microscopy and physical characterization of the carcinoembryonic antigen. *Biochemistry* **14**, 2323–2330 (1975).
29. Hammarström, S. The carcinoembryonic antigen (CEA) family: structures, suggested functions and expression in normal and malignant tissues. *Seminars in Cancer Biology* **9**, 67–81 (1999).

30. Egan, M. L., Coligan, J. E., Pritchard, D. G., William C. Schnute, J. & Todd, C. W. Physical characterization and structural studies of the carcinoembryonic antigen. *Cancer Research* **36**, 3482–3485 (1976).
31. Shuster, J., Silverman, M. & Gold, P. Metabolism of human carcinoembryonic antigen in xenogeneic animals. *Cancer Research* **33**, 65–68 (1973).
32. Martin, K. W. & Halpern, S. E. Carcinoembryonic antigen production, secretion, and kinetics in BALB/c mice and a nude mouse-human tumor model. *Cancer Research* **44**, 5475–5481 (1984).
33. Schmidt, M. M., Thurber, G. M. & Wittrup, K. D. Kinetics of anti-carcinoembryonic antigen antibody internalization: effects of affinity, bivalency, and stability. *Cancer Immunology Immunotherapy* **57**, 1879–1890 (2008).
34. Akamatsu, Y. *et al.* A single-chain immunotoxin against carcinoembryonic antigen that suppresses growth of colorectal carcinoma cells. *Clinical Cancer Research* **4**, 2825–2832 (1998).
35. Bronstein, B. R. *et al.* The use and limitations of serial plasma carcinoembryonic antigen (CEA) levels as a monitor of changing metastatic liver tumor volume in patients receiving chemotherapy. *Cancer* **46**, 266–272 (1980).
36. Choi, J. S. & Min, J. S. Significance of postoperative serum level of carcinoembryonic antigen (CEA) and actual half life of CEA in colorectal cancer patients. *Yonsei Medical Journal* **38**, 1–7 (1997).
37. Stein, R., Juweid, M., Mattes, M. J. & Goldenberg, D. M. Carcinoembryonic antigen as a target for radioimmunotherapy of human medullary thyroid carcinoma: Antibody processing, targeting, and experimental therapy with I-131 and Y-90 labeled MAbs. *Cancer biotechnology and radiopharmaceuticals* **14**, 37–47 (1999).
38. Geiser, M., Cebe, R., Drewello, D. & Schmitz, R. Integration of PCR fragments at any specific site within cloning vectors without the use of restriction enzymes and DNA ligase. *Biotechniques* **31**, 88–+ (2001).
39. al Yacoub, N., Romanowska, M., Haritonova, N. & Foerster, J. Optimized production and concentration of lentiviral vectors containing large inserts. *J Gene Med* **9**, 579–584 (2007).
40. Donello, J. E., Loeb, J. E. & Hope, T. J. Woodchuck hepatitis virus contains a tripartite posttranscriptional regulatory element. *J. Virol.* **72**, 5085–5092 (1998).
41. Beauchemin, N., Benchimol, S., Cournoyer, D., Fuks, A. & Stanners, C. P. Isolation and characterization of full-length functional cDNA clones for human carcinoembryonic antigen. *Mol. Cell. Biol* **7**, 3221–3230 (1987).
42. BOEHM M *et al.* Crystal structure of the anti-(carcinoembryonic antigen) single-chain Fv antibody MFE-23 and a model for antigen binding based on intermolecular contacts. (2000).at <<http://www.biochemj.org.libproxy.mit.edu/bj/346/bj3460519.htm>>

43. DuPage, M. Investigation of T cell-mediated immune surveillance against tumor-specific antigens in genetically engineered mouse models of cancer. (2011).at <<http://dspace.mit.edu/handle/1721.1/62620>>
44. Thurber, G. M. Distribution and metabolism of antibodies and macromolecules in tumor tissue. (2008).
45. Mittendorf, E. A. *et al.* Loss of HER2 Amplification Following Trastuzumab-Based Neoadjuvant Systemic Therapy and Survival Outcomes. *Clin Cancer Res* **15**, 7381–7388 (2009).
46. Zhou, H. *et al.* A novel transgenic mouse model for immunological evaluation of carcinoembryonic antigen–based DNA minigene vaccines. *Journal of Clinical Investigation* **113**, 1792–1798 (2004).
47. De Clerck, N. M. *et al.* High-Resolution X-ray Microtomography for the Detection of Lung Tumors in Living Mice. *Neoplasia* **6**, 374–379 (2004).
48. Shively, J. E. *et al.* Serum levels of carcinoembryonic antigen and a tumor-extracted carcinoembryonic antigen-related antigen in cancer patients. *Cancer Research* **42**, 2506–2513 (1982).

Appendix A: Tumor penetration model and parameters

Numerical simulations of antibody microdistribution are based upon a Krogh cylinder geometry¹. The Krogh cylinder assumes that tissue can be modeled as a cylinder of radius R_{krogh} surrounding a perfused blood vessel which supplies the volume in the cylinder with oxygen and nutrients. The model is therefore radially symmetric. For the purposes of antibody transport, numerous analyses and experimental studies have suggested the diffusive transport is the dominant mode of macromolecular transport within the tumor²⁻⁶. Therefore, only diffusive transport is considered in this model.

This model is implemented in Matlab using the method of lines to discretize over distance and solve the resulting system of ODEs using the built-in numerical integrators of Matlab. Further details of a similar implementation can be found at ⁷. The species considered in this model are defined below, followed by the governing equations solved in Matlab. Representative parameter values are also shown; these parameters are valid for the sm3e anti-CEA antibody and for antigen properties measured or found in the literature for LS174T xenograft tumors. These parameters can be adjusted for other tumors, antibodies, or macromolecules. Useful correlations for size effects of molecules on parameters such as void fraction, diffusivity, and permeability can be found at ⁸.

Parameter	Definition
[Ab]	Concentration of free (unbound) antibody in the tumor
[Ag]	Concentration of free (unbound) cell surface antigen in the tumor
[M]	Concentration of monovalently bound antibody-antigen complexes
[B]	Concentration of bivalently bound antibody-antigen complexes

Krogh cylinder model equations

$$\frac{\partial [Ab]}{\partial t} = D \left(\left(\frac{\partial^2 [Ab]}{\partial r^2} \right) + \frac{1}{r} \frac{\partial [Ab]}{\partial r} \right) - \frac{2k_{on} [Ab][Ag]}{\varepsilon} + k_{off} [M]$$

$$\frac{\partial [Ag]}{\partial t} = R_s - \frac{2k_{on} [Ab][Ag]}{\varepsilon} + 2k_{off} [B] + k_{off} [M] - k_e [Ag] - k_{on} [M][Ag_{eff}] \left(\frac{[Ag_{tot}] - 2[B] - [M]}{[Ag_{tot}]} \right)$$

$$\frac{\partial [M]}{\partial t} = \frac{2k_{on} [Ab][Ag]}{\varepsilon} - k_{off} [M] - k_e [M] - k_{on} [M][Ag_{eff}] \left(\frac{[Ag_{tot}] - 2[B] - [M]}{[Ag_{tot}]} \right) + 2k_{off} [B]$$

$$\frac{\partial [B]}{\partial t} = k_{on} [M][Ag_{eff}] \left(\frac{[Ag_{tot}] - 2[B] - [M]}{[Ag_{tot}]} \right) - k_e [B] - 2k_{off} [B]$$

Initial conditions:

$$[Ab] = [M] = [B] = 0$$

$$[Ag] = [Ag]_{tot} = 150 \text{ nM (for CEA in LS174T xenografts)}$$

Boundary conditions:

$$\left. \frac{\partial [Ab]}{\partial r} \right|_{r=R_{Krogh}} = 0$$

$$P \left(\left(\varepsilon [Ab]_{plasma} \right) - [Ab]_{cap} \right) = D \left(\left. \frac{\partial [Ab]}{\partial r} \right|_{r=0} \right)$$

Where $[Ab]_{plasma}$ is given by:

$$[Ab]_{plasma} = [Ab]_{plasma,0} \left(\alpha e^{-k_a t} + \beta e^{-k_b t} \right)$$

For all plots, outputs are at t=24 hours post-injection, corresponding to the time of euthanasia in the experimental data.

Krogh cylinder model parameter values			
Parameter	Definition	Value	Citation
ϵ	Tumor void volume	0.2391	⁸
Mouse blood volume	Volume of blood in ~20 g mouse	2 ml	Assumed
D	Diffusivity	$2.54 \times 10^{-7} \text{ cm}^2/\text{s}$	(⁸)
P	Vascular permeability	$3.87 \times 10^{-7} \text{ cm/s}$	(⁸)
R_{Krogh}	Krogh cylinder radius	60 μm	Measured
R_{cap}	Capillary radius	8 μm	(⁹)
K_d	Monovalent affinity	10 pM	Measured
$[\text{Ag}]_{\text{eff}}$	Effective antigen concentration for free arm of monovalently bound antibody	550 nM	Calculated (¹⁰)
$[\text{Ag}]_{\text{tot}}$	Total antigen concentration (free or bound)	150 nM	^{11,12}
R_s	Steady state antigen synthesis rate	$k_e * [\text{Ag}]_{\text{tot}}$	
k_{on}	On rate	$2 \times 10^5 \text{ M}^{-1}\text{s}^{-1}$	Assumed
k_{off}	Off rate	$K_d * k_{\text{on}}$	
k_e	Antigen endocytosis rate	$1.3\text{e-}5 \text{ s}^{-1}$	¹³
α	Fractional alpha clearance for biexponential plasma clearance	0.204	Measured
β	Fractional beta clearance for biexponential plasma clearance	0.796	Measured
k_a	Time constant for α clearance	4.32 h^{-1}	Measured
k_b	Time constant for β clearance	0.024 h^{-1}	Measured

References

1. Krogh, A. The number and distribution of capillaries in muscles with calculations of the oxygen pressure head necessary for supplying the tissue. *J Physiol* **52**, 409–415 (1919).
2. Baxter, L. T. & Jain, R. K. Transport of Fluid and Macromolecules in Tumors I: Role of Interstitial Pressure and Convection. *Microvascular Research* **37**, 77–104 (1989).
3. Rippe, B. & Haraldsson, B. Fluid and protein fluxes across small and large pores in the microvasculature. Application of two-pore equations. *Acta Physiol. Scand.* **131**, 411–428 (1987).
4. Thurber, G. M., Schmidt, M. & Wittrup, K. D. Antibody tumor penetration: Transport opposed by systemic and antigen-mediated clearance. *Advanced Drug Delivery Reviews* (2008).
5. Boucher, Y., Baxter, L. T. & Jain, R. K. Interstitial pressure gradients in tissue-isolated and subcutaneous tumors: Implications for therapy. *Cancer Research* **50**, 4478–4484 (1990).
6. Lawrence J. Nugent & Rakesh K. Jain Pore and fiber-matrix models for diffusive transport in normal and neoplastic tissues. *Microvasc Res* **28**, 270–274 (1984).
7. Thurber, G. M. Distribution and metabolism of antibodies and macromolecules in tumor tissue. (2008).
8. Michael M. Schmidt & K. Dane Wittrup A modeling analysis of the effects of molecular size and binding affinity on tumor targeting. *Mol Cancer Ther* **8**, 2861–2871 (2009).
9. Duane E. Hilmas & Edward L. Gillette Morphometric analyses of the microvasculature of tumors during growth and after X-irradiation. *Cancer* **33**, 103–110 (1974).
10. K. Dane Wittrup & Bruce Tidor *Biomolecular Kinetics and Cellular Dynamics*. (In preparation).
11. Laurence T. Baxter & Rakesh K. Jain Transport of fluid and macromolecules in tumors: 3. Role of binding and metabolism. *Microvascular Research* **41**, 5–23
12. Thurber, G. M., Zajic, S. C. & Wittrup, K. D. Theoretic Criteria for Antibody Penetration into Solid Tumors and Micrometastases. *Journal of Nuclear Medicine* **48**, 995–999 (2007).
13. Schmidt, M. M., Thurber, G. M. & Wittrup, K. D. Kinetics of anti-carcinoembryonic antigen antibody internalization: effects of affinity, bivalency, and stability. *Cancer Immunology Immunotherapy* **57**, 1879–1890 (2008).

Appendix B: DNA sequence of lentiviral vectors and protein constructs

Full length CEA (from NCBI)

atggagtctccctcggcccctccccacagatggatgcatcccctggcagaggctcctgctcacagcctcacttctaaccttctggaacccgcc
caccactgccaagctcactattgaatccacgccgttcaatgtcgcagaggggaaggagggtgcttctacttgtccacaatctgccccagcat
cttttggctacagctggtacaaagggtgaaagagtggatggcaaccgtcaaattataggatattgaataggaactcaacaagctaccca
ggcccgcatcacagtggtcgagagataatatacccacatgcatccctgctgatccagaacatcatccagaatgacacaggattctacacc
ctacacgcataaagttagatcttgaatgaagaagcaactggccagttccgggtatacccggagctgccaagccctccatctccagc
aacaactccaaacccgtggaggacaaggatgctgtggccttcacctgtgaacctgagactcaggacgcaacctacctgtggtgggtaaa
caatcagagcctccggctcagctccaggctgcagctgtccaatggcaacaggacctcactctattcaatgtcacaagaaatgacacagc
aagctacaaatgtgaaaccagaacccagtgagtgccaggcgagtgattcagtcctgaatgtcctctatggccgggatgccccac
catttcccctctaaacacatcttacagatcaggggaaaatctgaacctctctgccatgcagccttaaccacctgcacagtagcttgggt
ttgtcaatgggactttccagcaatccaccaagagctctttatcccacatcactgtgaataatagtgatcctatactgccaagccat
aactcagacactggcctcaataggaccacagtcacagcgtatgacagagccacccaaaccttcatcaccagcaacaactc
caaccccgaggatgaggatgctgtagccttaacctgtgaacctgagattcagaacacaacctacctgtggtgggtaataatcaga
gcctcccggtcagctccaggctgcagctgtccaatgacaacaggacctcactctactcagtgtcacaaggaatgatgtaggacctatg
agtgtggaatccagaacgaattaagtgtgaccacagcgaccagtcctgaatgtcctctatggccagacgacccaccatttccc
cctcatacactattaccgtccaggggtgaacctcagcctctctgccatgcagccttaaccacctgcacagtagcttgggtgattgat
gggaacatccagcaacacacaagagctctttatctcaacatcactgagaagaacagcggactctataacctgcccaggccaataactc
agccagtgccacagcaggactacagtcagacaatcacagtcctcgcggagctgccaagccctccatctccagcaacaactccaac
ccgtggaggacaaggatgctgtggccttcacctgtgaacctgaggctcagaacacaacctacctgtggtgggtaaatggtcagagcctcc
cagtcagctccaggctgcagctgtccaatggcaacaggacctcactctattcaatgtcacaagaaatgacgcaagagcctatgatgtg
gaatccagaactcagtgagtgcaaaccgagtgaccagtcaccctggatgtcctctatggccggacaccccatcatttccccccag
actcgtcttaccttccggagcgaacctcaacctctctgccactcggccttaaccatccccgagtagcttggcgtatcaatgggata
ccgagcaacacacaagttctttatcgccaaaatcacgcaaaataataacgggacctatgctgtttgtcttaactggctactgg
ccgcaataattccatagtagcaagagcatcacagtcctgcatctggaactctctggctctcagctggggccactgtcggcatcatgattg
gagtgctggtggggtgctctgatatag

Fractional CEA (CEAfrac)

CEA signal peptide + domains 1 and 2:

Signal peptide (AA 1-34)

Domain 1 (AA 35-144)

Domain 2 (AA 146-237)

Propeptide (c terminal) (AA 678-702)

Data from NCBI Blast

ATGGAGTCTCCCTCGGCCCTCCCCACAGATGGTGCATCCCCTGGCAGAGGCTCCTGCTCACAGCCTCAC
TTCTAACCTTCTGGAACCCGCCCAACTGCCAAGCTCACTATTGAATCCACGCCGTTCAATGTCGCAGA
GGGGAAGGAGGTGCTTCTACTTGTCCACAATCTGCCCCAGCATCTTTTTGGCTACAGCTGGTACAAAGGT
GAAAGAGTGGATGGCAACCGTCAAATTATAGGATATGTAATAGGAACTCAACAAGCTACCCCAGGGCC
CGCATAACAGTGGTTCGAGAGATAATATACCCAATGCATCCCTGCTGATCCAGAACATCATCCAGAATGAC
ACAGGATTCTACACCCTACACGTCATAAAGTCAGATCTTGTGAATGAAGAAGCAACTGGCCAGTTCCGG
GTATACCCGGAGCTGCCAAGCCCTCCATCTCCAGCAACAACCTCCAAACCCGTGGAGGACAAGGATGCT
GTGGCCTTCACTGTGAACCTGAGACTCAGGACGCAACCTACCTGTGGTGGGTAAACAATCAGAGCCTC
CCGGTCAGTCCCAGGCTGCAGCTGTCCAATGGCAACAGGACCCTCACTCTATTCAATGTCACAAGAAAT
GACACAGCAAGCTACAAATGTGAAACCCAGAACCAGTGAGTGCCAGGCGCAGTGATTCAGTCATCTG
AATGTCCTCTATGGCCCGACTTCTCCTGGTCTCTCAGCTGGGGCCACTGTCGGCATCATGATTGGAGTGC
TGGTTGGGGTTGCTCTGATATAG

Translation:

MESPSAPPHRW CIPWORLLLTASLLTFWNPPTTAKLTIESTPFNVAEGKEVLLLVHNL PQHLFGYSWYKGER
VDGNRQIIGYVIGTQQATPGPAYSGREIYPNASLLIQNIIQNDTGFYTLHVIKSDLVNEEATGQFRVYELPKF
SISNNSKPVEDKDAVAF TCEPE TQDATYLWVNNOSLPVSPRLQLSNGNRTLTLFNVTRNDTASYKCTC
NPVSARRSDSVILNVLYGFTSPGLSAGATVGIMIGVLVGVALI

Fractional CEA w/(G₄S)₂

ATGGAGTCTCCCTCGGCCCTCCCCACAGATGGTGCATCCCCTGGCAGAGGCTCCTGCTCACAGCCTCAC
TTCTAACCTTCTGGAACCCGCCCAACTGCCAAGCTCACTATTGAATCCACGCCGTTCAATGTCGCAGA
GGGGAAGGAGGTGCTTCTACTTGTCCACAATCTGCCCCAGCATCTTTTTGGCTACAGCTGGTACAAAGGT
GAAAGAGTGGATGGCAACCGTCAAATTATAGGATATGTAATAGGAACTCAACAAGCTACCCCAGGGCC
CGCATAACAGTGGTTCGAGAGATAATATACCCAATGCATCCCTGCTGATCCAGAACATCATCCAGAATGAC
ACAGGATTCTACACCCTACACGTCATAAAGTCAGATCTTGTGAATGAAGAAGCAACTGGCCAGTTCCGG
GTATACCCGGAGCTGCCAAGCCCTCCATCTCCAGCAACAACCTCCAAACCCGTGGAGGACAAGGATGCT
GTGGCCTTCACTGTGAACCTGAGACTCAGGACGCAACCTACCTGTGGTGGGTAAACAATCAGAGCCTC
CCGGTCAGTCCCAGGCTGCAGCTGTCCAATGGCAACAGGACCCTCACTCTATTCAATGTCACAAGAAAT
GACACAGCAAGCTACAAATGTGAAACCCAGAACCAGTGAGTGCCAGGCGCAGTGATTCAGTCATCTG
AATGTCCTCTATGGCCCGGAGGTGGCGGTAGTGCGGAGGTGGTTCTACTTCTCCTGGTCTCTCAGCTG
GGGCCACTGTCGGCATCATGATTGGAGTGTGGTTGGGGTTGCTCTGATATAG

Fractional CEA in transfer vector (NLSCre, from Jacks lab)

Sequencing of plasmid backbone from Monte Winslow of Jacks lab. Highlighted and colored portion represents fractional CEA.

CEA leader + Domains 1 and 2 of CEA
CEA proprotein (processed prior to export)

CATGCTTCATCGTCGGTCCGGGCTGCCACGACCAAGTGACAGCAATGCTGTTTCACTGGTTATGCGGCG
GATCCGAAAAGAAAACGTTGATGCCGGTGAACGTGAAAACAGGCTCTAGCGTTCGAACGCACTGATTT
CGACCAGGTTCTGTTCACTCATGGAAAATAGCGATCGCTGCCAGGATATACGTAATCTGGCATTCTGGG
GATTGCTTATAACACCCTGTTACGTATAGCCGAAATTGCCAGGATCAGGGTTAAAGATATCTCACGTACT
GACGGTGGGAGAATGTTAATCCATATTGGCAGAACGAAAACGCTGGTTAGCACCCGAGGTGTAGAGAA
GGCACTTAGCCTGGGGGTAATAACTGGTCGAGCGATGGATTTCCGTCTCTGGTGTAGCTGATGATCC
GAATAACTACCTGTTTTGCCGGTTCAGAAAAATGGTGTGCCGCGCCATCTGCCACCAGCCAGCTATCA
ACTCGCGCCTGGAAGGGATTTTTGAAGCAACTCATCGATTGATTTACGGCGCTAAGGATGACTCTGGT
CAGAGATACCTGGCCTGGTCTGGACACAGTCCCCTGTCCGAGCCGCGCAGATATGGCCCCGCTGG
AGTTTCAATACCGGAGATCATGCAAGCTGGTGGCTGGACCAATGTAATATTGTCATGAACTATATCCGT
AACCTGGATAGTAAACAGGGGCAATGGTGCCTGCTGGAAGATGGCGATgggcccggcggctccggcgag
ggcaggggaagtcttctaactgcggggacgtggaggaaaatcccggcccagaattcATGGAGTCTCCCTCGGCCCCCTCCCC
ACAGATGGTGCATCCCCTGGCAGAGGCTCCTGCTCACAGCCTCACTTCTAACCTTCTGGAACCCGCCCAG
CACTGCCAAGCTCACTATTGAATCCACGCCGTTCAATGTCCGAGAGGGGAAGGAGGTGCTTCTACTTGT
CCACAATCTGCCCAAGCATCTTTTTGGCTACAGCTGGTACAAAGGTGAAAGAGTGGATGGCAACCGTCA
AATTATAGGATATGTAATAGGAACTCAACAAGCTACCCCAAGGGCCCCGCATACAGTGGTCGAGAGATAAT
ATACCCCAATGCATCCCTGCTGATCCAGAACATCATCCAGAATGACACAGGATTCTACACCCTACACGT
ATAAAGTCAGATCTTGTGAATGAAGAAGCAACTGGCCAGTTCGGGTATACCCGGAGCTGCCAAGCCC
TCCATCTCCAGCAACAACCTCCAAACCCGTGGAGGACAAGGATGCTGTGGCCTTCACCTGTGAACCTGAG
ACTCAGGACGCAACCTACCTGTGGTGGTAAACAATCAGAGCCTCCCGGTCACTCCCAGGCTGCAGCTG
TCCAATGGCAACAGGACCCTCACTCTATTCAATGTCCACAAGAAATGACACAGCAAGCTACAAATGTGA
ACCCAGAACCCAGTGAGTGCCAGGCGCAGTGATTGAGTCATCCTGAATGTCTCTATGGCCCCACTTCTC
CTGGTCTCTCAGCTGGGGCCACTGTCGGCATCATGATTGGAGTGCTGGTTGGGGTTGCTCTGATATAGtt
aattaagctagcgatatcgtattctaactatgttgctcctttacgctatgtggatacgtgctttaatgcctttgatcatgctattgcttcc
cgtatggcttccatttctcctcctgtataaatcctggttgctgctctttatgaggagttgtggcccgttgcaggcaactggcgtgggtg
cactgtgttgctgacgaacccccactggtggggcattgccaccactgtcagctccttccgggactttcgttccccctccctattgcc
acggcggaactcatcgcgctgcttcccgtgctggacaggggctcggctgtgggactgacaattcctggtgtgtcggggaag
ctgacgtccttccatggctgctgcctgtgtgccacctggattctgcgcgggacgtccttctgctacgtccctcggcctcaatccagcg
gacctcctcccggcctgctccggctctgcggccttccgctcttgcctcgcctcagacgagtcggatctcctttgggccc
tccccgctgtttgcctcggcgtcggctagaggtaaccttaagaccaatgactacaaggcagctgtagatcttagccacttttaaaa
gaaaaggggggactggaagggttaattcactccaacgaagacaagatctgcttttctgtactgggtctctggttagaccagatct
gagcctgggagctcttggttaactaggaacccactgcttaagcctcaataaagctgccttgagtcttaagtagtgtgtgccgtct
ggtgtgactctggttaactagagatccctcagacccttttagtcagtggtgaaaatcttagcagtagtagttcatgtcatcttattatca
gtattataactgcaaagaaatgaatatcagagagtgagaggaactgtttattgcagcttataatggttacaataaagcaatagcatc
acaaattcacaaataaagcatttttctactgattctagttgtggtttgccaactcatcaatgatcttatcatgtctggctctagctatc
ccgccctaactccgccatcccgccctaactccgccagtccgccattctccgccatggctgactaatttttttattatgcagag
gccgaggccgctcggcctctgactattccagaagtagtgaggaggctttttggaggcctagggacgtaccaatcgcctatagtg
gtcgtattacgcgctcactggcctgcttttacaacgtcgtgactgggaaaaccctggcgttaccctaactaatcgccttgagcacatc
ccccttcgacgctggcgtaatagcgaagaggcccgcaccgatcgccttccaacagttgcgcagcctgaatggcgaatgggacg
ccctgtagggcgcatgaagcgcggcgggtgtggtggttacgcgcagcgtgaccgctacactgccagcgcctagcggcctcctttc
cttcttccctccttctcgcacgttcgcccgttccccgtaagctctaaatcgggggctcccttagggtccgatttagtctttacg
cacctcgaccccaaaaacttgattagggtaggttcacgtagtgggccatcgccctgatagacggttttcgcctttgacgttgagtc
cacgttcttaatagtgactctgttccaaactggaacaactcaaccctatctcggctattctttgattataagggattttgccgatt
tcggcctattggttaaaaaatgagctgatttaaaaaatgaacgcaatttaacaaaatattaacgcttacaatttaggtggcactttt

cggggaaatgtgCGCGgaaccctatttgtttattttctaaatacattcaaataatgtatccgctcatgagacaataaccctgataaatgct
tcaataatattgaaaaaggaagagtatgagtattcaacatttccgtgCGCCctattccctttttgCGGCattttgccttctgttttgc
accagaaacgctggtgaaagtaaaagatgctgaagatcagttgggtgCACgagtgggttacatCGaaactggatctcaacagCGgtaa
gatccttgagagttttcGCCCCgaagaacgtttccaatgatgagcacttttaaagttctgctatgtggCGCGgtattatcccgtattgacGC
cgggcaagacaaactCGTcGCGcatacactattctcagaatgacttgggtgagtaactaccagtcacagaaaagcatcttacggatgg
catgacagtaagagaattatgcagtgtGCCataacatgagtataactgCGGCCaacttacttctgacaacgatcggaggaccga
aggagctaacgctttttgcaacaacatgggggatcatgtaactgccttgatcgttgggaaccggagctgaatgaagccataccaaacg
acgagcgtgacaccacgatgcctgtagcaatggcaacaacgttgcGcaactattaactggCGaaacttacttacttagcttcccggcaac
aattaatagactggatggaggCGgataaagttgcaggaccattctgcgctCGGCCcttccggctggctggtttattgctgataaatctgg
agccggtgagcgtgggtctcGCGgtatcattgcagcactggggccagatgtaagccctcccgtatcgtagttatctacacgacggggag
tcaggcaactatggatgaacgaaatagacagatcGctgagataggtgcctcactgattaagcattgtaactgtcagaccaagttactc
atatatacttttagattgattaaaacttatttttaattaaaaggatctaggtgaagatcctttttgataatctcatgacccaaatccctaa
cgtgagtttctgtccactgagcgtcagaccccgtagaaaagatcaaaggatcttcttgagatccttttttctgCGCGtaactgctgcttg
caacaaaaaaaccacgctaccagCGgtggtttgttgcCGgatacaagagctaccaactcttttccgaaggtaactggcttcagcaga
gCGcagataccaaatactgttcttagttagcctgagttaggccaccactcaagaactctgtagcaccgctacatacctcGctctgct
aatcctgttaccagtgGctgctGCCagtgGCgataagtcgtgtcttaccgggttgactcaagacgatagttaccggataaggCGcagCG
gtcgggctgaacggggggtctgTcacacagcccagcttgagCGaacgacctacaccgaactgagatacctacagcgtgagctatga
gaaagCGccacgcttcccgaagggagaaaaggCGgacaggtatccggtaaagCGgagggctCGgaacaggagagCGcagcaggggagct
tccaggggaaacgctggtatctttatagctcgtCGggttCGCCacctctgacttgagcgtcgattttgtgatgctcgtcaggggggc
ggagcctatggaaaaacgCCagcaacgCGccttttaccggtcctggccttttctggccttttctcacatgttcttctcGcttatccc
tgattctgtggataaccgtattaccgctttgagtgagctgataaccgctcGCGcagccgaacgaccgagCGcagCGagtcagtgagCGa
ggaagCGgaagagCGccaatacGcaaacgctctccccGCGgttggCGgattcattaatgCagctggcagcagagtttcccgact
ggaaagCGggcagtgagCGcaacGcaattaatgtgagttagctcactcattaggcaccacaggctttacactttatgcttccggctcgtat
gttgtgtggaattgtgagCGgataacaatttcacacaggaacacgctatgaccatgattacGccaagCGcGcaattaaccctcactaaag
ggaacaaaagctggagctgcaagcttaatgtagtcttatgcaatactctgtagtcttGcaacatggtaacgatgagttagcaacatgcct
tacaaggagagaaaaagcaccgtgcatGCCgattggtggaagtaaggtggtagatcgtGCcttattaggaaggcaacagacgggtct
gacatggattggacgaaccactgaattGCCcattgcagagatattgtatttaagtcctagctcGatacataaacg

Full length CEA in transfer vector

Sequencing from Monte Winslow of Jacks lab. Highlighted and colored portion represents CEA, which has been ~80% sequenced and appears to be okay. Total length of plasmid 10934 bp, of which 2109 is CEA.

ggtctctctggttagaccagatctgagcctgggagctctctggctaactaggaaccactgcttaagcctcaataaagcttgccttgagt
gcttcaagtagtgtgtgccgtctgttgtgactctgtaactagagatccctcagacccttttagtcagtgtggaatctctagcagtg
gCGcccgaacagggacttgaaagCGaaagggaaccagaggagctctctcGacgCaggactcggcttgctgaagCGcGcagCGcaag
aggCGaggggCGgactggtgagtagcGcaaaaaatttgactagCGgaggctagaaggagagagatgggtgCGagagcgtcagttat
aagCGgggggagaattagatcGcgatgggaaaaaattCGgttaaggccaggggaaagaaaaatataaataaaacatatagtatgg
gcaagcaggagctagaacgattcGcagttaatcctggcctgttagaaacatcagaaggctgtagacaaatactgggacagctacaac
catccctcagacaggatcagaagaacttagatcattatataatacagtagcaacccttattgtgtgcatcaaaggatagagataaaag

ACTCGCGCCTGGAAGGGATTTTTGAAGCAACTCATCGATTGATTTACGGCGCTAAGGATGACTCTGGT
CAGAGATACCTGGCCTGGTCTGGACACAGTGCCCGTGTGGAGCCGCGGAGATATGGCCCGCGCTGG
AGTTTCAATACCGGAGATCATGCAAGCTGGTGGCTGGACCAATGTAAATATTGTCATGAACTATATCCGT
AACCTGGATAGTGAACAGGGGCAATGGTGCCTGCTGGAAGATGGCGATgggcccggcggctccggcgag
ggcaggggaagtcttctaacatgccccgacgtggaggaaaatccccggcccagaattc**atggagctccctcgccctcccccagatg**
gtgcatcccctggcagaggctcctgctcacagcctcacttctaaccttctggaacccgccaccactgccaagctcactattgaatccacg
ccgttcaatgtcgagaggggaaggaggtgcttctactgtccacaatctccccagcatcttttgctacagctggtacaaaggatgaaa
gagtgatggcaaccgtcaaattataggatgtaataggaactcaacaagctaccccagggccgcatacagtggtcgagagataata
tacccaatgcatccctgctgatccagaacatcatccagaatgacacaggattctacacctacacgtcataaagtcagatcttgaatg
aagaagcaactggccagttccgggtataccccggagctgccaagccctccatctccagcaacaactccaaaccgtggaggacaagga
tgctgtggccttcacctgtgaacctgagactcaggacgcaacctacctgtggggtaacaatcagagcctccggctcagctccaggct
gcagctgtccaatggcaacaggacctcactcttcaatgtcacaagaaatgacacagcaagctacaaatgtgaaaccagaacca
gtgagtgccaggcagtgattcagtcacctgaatgtcctctatggccggatgccccaccatttccccttaaacacatcttacagatc
aggggaaaatctgaacctctctgccacgcagccttaaccacctgcacagtactcttggttgtaatgggactttccagcaatccacc
caagagctctttatccccaacatcactgtgaataatagtgatcctatacgtgccaagccataactcagacactggcctcaataggacc
acagtcacgacgatcacagtctatgcagagccacccaaaccttcatcaccagcaacaactccaacccgtggaggatgaggatgctgt
agccttaacctgtgaacctgagattcagaacacaacctacctgtggggtaataatcagagcctccggctcagctccaggctgcagct
gtccaatgacaacaggacctcactctactcagtgtcacaaggaatgatgtaggacctatgagtggtgaatccagaacgaattaagtg
tgaccacagcagccagtcactctgaatgtcctctatggcccagacgccccaccatttcccctcatacacctattaccgtccaggggtg
aacctcagcctctctgcatgagccttaaccacctgcacagtattctggctgattgatgggaacatccagcaacacacacaagag
ctctttatctccaacatcactgagaagaacagcggactctatacctgccaggccaataactcagccagtgccacagcaggactacagtc
aagacaatcacagtctctgaggagctgccaagccctccatctccagcaacaactccaaaccgtggaggacaaggatgctgtggcctt
cacctgtgaacctgaggctcagaacacaacctacctgtggggtaaatgggtcagagcctccagtcagctccaggctgcagctgtcaa
tggaacaggacctcactctattcaatgtcacaagaaatgacgcaagagcctatgtatgtggaatccagaactcagtgagtgcaaac
gcagtgaccagtcaccctggatgtcctctatggccggacacccccatcatttccccccagactcttaccttccgggagcgaacctc
aacctctctgccactcggccttaaccatccccgcagtattctggcgtatcaatgggataccgcagcaacacacacaagttctctttat
cgccaaaatcacgcaaaataataacgggacctatgcctgtttgtcttaactggctactggccgcaataattccatagtaagagcctc
acagctctctgcatctggaacttctctggctctcagctggggccactgtcgcatcatgattggagtgctggtggggttctctgatatag
ttaattaagctagcgatatcgtattcttaactatggtgctctttacgctatgtggatacgtgctttaatgcctttgatcatgctattgctc
ccgtatggctttcattttctcctctgtataaatcctggtgtgtctctttatgaggagtgtggcccgtgtcaggcaacgtggcgtggtgt
gcactgtgttctgacgcaacccccactgggtggggcattgccaccacctgcagctccttccgggactttcgctttccccctcctattgc
cacggcggaactcatcggcctgcctgcccgtgctggacaggggctcggtgtgggactgacaattccgtggtgtgtcggggaa
gctgacgtcctttcatggctgctgcctgtgtgcccactggattctgcgaggacgtccttctgctacgtccctcggccctcaatccagc
ggaccttcttcccggcctgctgcccgtctgcccctctccgctctcgcctcgcctcagacgagtcggatcctcttgggcccgc
ctccccgctgttctgcctcggcgtccggtctagaggtacctttaagaccaatgacttacaaggcagctgtagatcttagccacttttaa
agaaaaggggggactggaagggttaattcactcccaacgaagacaagatcgtcttttgctgtactgggtctctctggttagaccagat
ctgagcctgggagctctctggtaactagggaaacctgcttaagcctcaataaagcttgcttgagtgctcaagtagtggtgcccgt
ctgtgtgtgactctggtaactagagatccctcagaccctttagtcagtggtgaaaatctctagcagtagtagtcatgtcatcttattatc
agtatttataactgcaaagaaatgaatatcagagagtgagaggaactgtttattgcagcttataatggttacaataaagcaatagca
tcacaaatccacaaataaagcatttttactgcattctagtgtggtttgccaactcatcaatgtatcttcatgtctggcttagcta
tccgcccctaactccgccatccgcccctaactccgccagtccgccattctccgcccagtggtgactaattttttttttatgaga
ggccgagggcctcgccctgagctattccagaagtagtgaggaggctttttggaggcctaggacgtaccaattcgcctatagtg
agtcgtattacgcgctcactggcctcgttttacaacgtcgtgactgggaaaacctggcgttaccacactaatcgccttgacgaca
tcccccttccagcagtggtgtaatagcgaagggcccgcaccgatgccttcccaacagttgcgagcctgaatggcgaatgggacgc

gccctgtagcggcgcatlaagcgcggcggtgtggtggttacgcgcagcgtgaccgctacacttgccagcgcctagcggcctcctttc
gctttctcccttctttctgccacgttcgccggctttccccgcaagctctaaatcgggggctcccttaggggtccgatttagtgccttac
gcacctcgaccccaaaaaacttgattagggatgaggttacgtagtgggcatcgcctgatagacggttttcggccttgacgttgag
ccacgttcttaatagtgactctgttccaaactggaacaactcaaccctatctcggctattctttgattataagggatttgcgat
ttcggcctattggttaaaaaatgagctgatttaaaaaatlaacgcgaatttaacaaaatattaacgcttacaatttagtgacatt
tcggggaaatgtgcgcggaaccctattgtttattttctaaatacattcaaatatgtatccgctcatgagacaataaccctgataaatgc
ttcaataatattgaaaaaggaagatgagattcaacatttccgtgctgccttattccctttttgcggcattttgcttctgttttgc
caccgaaacgctggtgaaagtaaaagatgctgaagatcagttgggtgcacgagtggttacatcgaactggatctcaacagcggta
agatccttgagagtttgcggcgaagaacgtttccaatgatgagcacttttaaaagtctgctatgtggcgcggtattatcccgtattgac
ccgggcaagacactcgtgcgcacatacactattctcagaatgacttggtgagtactaccagtcacagaaaagcatcttacggatg
gcatgacagtaagagaattatgcagtgctgccataacctgagtgataaactgcggccaacttactctgacaacgatcggaggaccg
aaggagtaaccgctttttgcacaacatgggggatcatgtaactgccttgatcgttgggaaccggagctgaatgaaccatacacaac
gacgagcgtgacaccacgatgcctgtagcaatggcaacaacgttgcgcaactattaactggcgaactacttacttagcttccggcaa
caataatagactggatggaggcgataaagttgcaggaccacttctgcgctcggccttccggctgggtgtttattgctgataaatctg
gagccggtgagcgtgggtctcgcggtatcattgcagcactggggccagatggtaagccctccgctatcgtagttatctacacgacgggga
gtcaggcaactatggatgaacgaaatagacagatcgtgagataggtgcctcactgattaagcattggtaactgtcagaccaagttact
catatatactttagattgatttaaaacttattttaatttaaaaggatctaggtgaagatccttttgataatctcatgacaaaatccctta
acgtgagtttctgtccactgagcgtcagacccctagaaaagatcaaaggatcttctgagatcctttttctgcgtaatctgctgctt
gcaaaacaaaaaaccaccgctaccagcgggtgtttgttgcggatcaagagctaccaactcttttccgaagtaactggcttcagcag
agcgcagatacacaactgttcttctagtgtagccgtaggtaggccaccactcaagaactctgtagcaccgcctacatacctcgtctgc
taatcctgttaccagtggtgctgccaagtggcgataagtcgtgtcttaccgggtggactcaagacgatgttaccggataaggcgcagc
ggtcgggctgaacggggggtcgtgcacacagcccagcttggagcgaacgacctacaccgaactgagatacctacagcgtgagctatg
agaaagcggcagcttcccgaaggagaaaggcggacaggtatccgtaagcggcagggtcggaaacaggagagcgcacgaggggagc
ttcagggggaaacgcctggtatctttatagtcctgtcgggttccgacactctgacttgagcgtcgattttgtgatgctcgtcagggggc
ggagcctatggaaaaacgcccagcaacgccccttttacggcttctggccttttgcggcctttgctcacaatgttcttctgcgttatcccc
tgattctgtggataaccgtattaccgctttgagtgcctgataaccgctcggcagccgaacgaccgagcgcagcagtgctgagcga
ggaagcgggaagagcggcaatacgcacaaccgcttccccgcgcttggccgattcattaatgcagctggcacgacaggttcccgact
ggaaagcgggcagtgagcgaacgcaattaatgtgagttagctcactcattaggcaccaggctttacactttatgcttccggctgctat
gttgtgtggaattgtgagcggataacaattcacacaggaaacagctatgacctgattacgccaagcgcgcaattaaccctcactaaag
ggaacaaaagctggagctgcaagcttaatgtagtcttatgcaatacctttagtcttgaacatggtaacgatgagttagcaaatgcct
tacaaggagagaaaaagcaccgtgcatgccgattggtggaagtaagtggtacgatcgtgccttattaggaaggcaacagacgggtct
gacatggattggacgaaccactgaattgccgattgcagagatattgtatttaagtgcttagctcgatacataaacg

Murine sm3e LC in gWiz plasmid

PstI
Stop codons
Sm3e Variable light domain
FLAG epitope tag
Leader Sequence
TA99 (mIgG2a) Ck
GTCGAC =SalI

Gwiz backbone shown in this sequence as unaltered text

TCGCGCGTTTCGGTGATGACGGTGAAAACCTCTGACACATGCAGCTCCCGGAGACGGTCACAGCTTGTC
TGTAAGCGGATGCCGGGAGCAGACAAGCCCGTCAGGGCGCGTCAGCGGGTGTGGCGGGTGTGGGG
CTGGCTTAACTATGCGGCATCAGAGCAGATTGACTGAGAGTGCACCATATGCGGTGTGAAATACCGCA
CAGATGCGTAAGGAGAAAATACCGCATCAGATTGGCTATTGGCCATTGCATACGTTGTATCCATATCATA
ATATGTACATTTATATTGGCTCATGTCCAACATTACCGCCATGTTGACATTGATTATTGACTAGTTATTAAT
AGTAATCAATTACGGGGTCATTAGTTCATAGCCCATATATGGAGTCCGCGTTACATAACTTACGGTAAA
TGGCCCGCCTGGCTGACCGCCAACGACCCCGCCATTGACGTCAATAATGACGTATGTTCCCATAGTA
ACGCCAATAGGGACTTTCCATTGACGTCAATGGGTGGAGTATTTACGGTAAACTGCCACTTGGCAGTA
CATCAAGTGTATCATATGCCAAGTACGCCCCCTATTGACGTCAATGACGGTAAATGGCCCGCCTGGCATT
ATGCCCAGTACATGACCTTATGGGACTTTCCTACTTGGCAGTACATCTACGTATTAGTCATCGCTATTACC
ATGGTGATGCGGTTTTGGCAGTACATCAATGGGCGTGGATAGCGGTTTGACTCACGGGGATTCCAAGT
CTCCACCCCATGACGTCAATGGGAGTTTGTGGTGGCACAAAATCAACGGGACTTTCAAAATGTCGTA
ACAACCTCCGCCCCATTGACGCAAATGGGCGGTAGGCGTGTACGGTGGGAGGTCTATATAAGCAGAGCT
CGTTTAGTGAACCGTCAGATCGCCTGGAGACGCCATCCACGCTGTTTTGACCTCCATAGAAGACACCGG
GACCGATCCAGCCTCCGCGGCCGGGAACGGTGCATTGGAACGCGGATTCCCCGTGCCAAGAGTGACGT
AAGTACCGCCTATAGACTCTATAGGCACACCCCTTGGCTCTTATGCATGCTATACTGTTTTGGCTGGG
GCCTATACACCCCGCTTCTTATGCTATAGGTGATGGTATAGCTTAGCCTATAGGTGTGGGTTATTGAC
CATTATTGACCACTCCCCTATTGGTGACGATACTTCCATTACTAATCCATAACATGGCTCTTGCCACAAC
TATCTCTATTGGCTATATGCCAATACTCTGTCCTTCAGAGACTGACACGGACTCTGTATTTTTACAGGATG
GGGTCCCATTATTATTTACAAATCACATATAACAACGCCGTCCCCCGTGCCCGCAGTTTTTATTA
CATAGCGTGGGATCTCCACGCGAATCTCGGGTACGTGTTCCGGACATGGGCTCTTCTCCGGTAGCGGCG
GAGCTTCCACATCCGAGCCCTGGTCCCATGCCTCCAGCGGCTCATGGTCGCTCGGCAGCTCCTTGCTCCT
AACAGTGGAGGCCAGACTTAGGCACAGACAATGCCACCACCACAGTGTGCCGCACAAGGCCGTGG
CGGTAGGGTATGTGTCTGAAAATGAGCGTGGAGATTGGGCTCGCACGGCTGACGCAGATGGAAGACTT
AAGGCAGCGGCAGAAGAAGATGCAGGCAGCTGAGTTGTTGTATTCTGATAAGAGTCAGAGGTA
ACTCCGTTGCGGTGCTGTTAACGGTGGAGGGCAGTGTAGTCTGAGCAGTACTCGTTGCTGCCGCGCGCCA
CCAGACATAATAGCTGACAGACTAACAGACTGTTCTTTCCATGGGTCTTTCTGCAGATGAGGGTCCCC
GCTCAGCTCCTGGGGCTCCTGCTGCTCTGGCTCCCAGGTGCACGATGTCTCTTTGACTACAAGGACGACG
ATGACAAGCCTAGGGAAAATGTGCTGACCCAATCTCCAAGCTCCATGTCTGTTTCTGTTGGCGATAGAGT
AACCATCGCTTGTAGCGCATCCTCTAGTGTCCCATATATGCACTGGCTTCAACAGAAGCCAGGTA
AAAAGCCAAAGTTGTTGATTTATTTGACATCCAACCTGGCTTCTGGAGTGCCTTCAAGGTTTTCTGGT
TCCGGCTCAGGAACCGATTATAGTTTACTATTAGCTCAGTGCAGCCAGAGGATGCTGCAACCTACTATT
GCCAGCAAAGGTCCTCATATCCACTGACTTTCGGGGGTGGAACGAAGTTGAAAATCAAGCGGGCTGATGCT
GCACGAACTGTATCCATCTTCCCACCATCCAGTGAAGCAGTTAACATCTGGAGGTGCCTCAGTCGTGTGCTT
CTTG
AACAACCTTACCCCCAAAGACATCAATGTCAAGTGGAAAGATTGATGGCAGTGAACGACAAAATGGCGT
CTGAACAGTTGGACTGATCAGGACAGCAAAGACAGCACCTACAGCATGAGCAGCACCCCTCACGTTGAC
AAGGACGAGTATGAACGACATAACAGCTATACCTGTGAGGCCACTCACAAGACATCAACTTCACCCATT
GTCAAGAGCTTCAACAGGAATGAGTGTAAATAGSTCGACACGTGTGATCAGATATCGCGGCCGCTCTAG
ACCAGGCGCCTGGATCCAGATCACTTCTGGCTAATAAAAAGATCAGAGCTCTAGAGATCTGTGTGTTGGT
TTTTTGTGGATCTGCTGTGCCTTCTAGTTGCCAGCCATCTGTTGTTGCCCTCCCCCGTGCCTTCTTGAC
CCTGGAAGGTGCCACTCCACTGTCCTTCTAATAAAAATGAGGAAATTGCATCGCATTGTCTGAGTAGG
TGTCATTCTATTCTGGGGGGTGGGGTGGGGCAGCACAGCAAGGGGGAGGATTGGGAAGACAATAGCA

Murine sm3e HC insert

Sm3e Vh

Mouse IgG2a Ch1

```
AGATGGGTTGGAGCCTCATCTTGCTCTTCCTTGTCGCTGTTGCTACGACGCGTCAAGTTAAACTGGAACA  
GTCCGGTGCTGAAGTTGTCAAACCAGGTGCTTCCGTGAAGTTGCCTGTAAAGCCTCTGGTTTTAACATC  
AAGGATTCGTATATGCATTGGTTGAGACAAGGGCCAGGACAAAGATTGGAATGGATTGGCGGGATTGA  
TCCAGAGAATGGTGATACCGAGTACGCTCCTAAATTTAGGGAAAGGCTACTTTTACTACCGACTTCC  
GCTAATACCGCATACTTGGGCTTATCTTCCTGAGACCAGAGGACACTGCCGTATACTACTGCAACGAAG  
GGACACCAACTGGTCTTACTATTTGACTACTGGGGACAAGGTACCTTAGTTACTGTCTCTAGCGCTAG  
CGCCAAAACAACAGCCCCATCGGTCTATCCACTGGCCCCCTGTGTGTGGAGGTACAACCTGGCTCCTCGGT  
GACTCTAGGATGCCTGGTCAAGGGTTATTTCCCTGAGCCAGTGACCTTGAACCTGGAACCTCTGGCTCACTG  
TCCAGTGGTGTGCACACCTTCCCAGCTCTCCTCCAATCTGGCCTCTACACCCTCAGCAGCTCAGTGACTGT  
AACCTCGAACACCTGGCCAGCCAGACCATCACCTGCAATGTGGCCACCCGGCAAGCAGCACCAAAGT  
GGACAAGAAAATTGAGCCCAGAGTGCCATAACACAGAACCCCTGTCTCCACTCAAAGAGTGTCCCCC  
ATGCGCAGCTCCAGACCTCTTGGGTGGACCATCCGTCTTCATCTTCCCTCCAAGATCAAGGATGTACTC  
ATGATCTCCCTGAGCCCCATGGTCACATGTGTGGTGGTGGATGTGAGCGAGGATGACCCAGACGTCCAG  
ATCAGCTGGTTTGTGAACAACGTGGAGTACACACAGCTCAGACACNAACCCATAGAGAGGATTACACA  
GTACTCTCGGTGTCAGTGCCTCCCATCCAGCACAGNCTGNTGAGTGCAGGAGTTCAATGCAAGNCAACN  
ACNAGTCCCTCCATCCCCATCGAGAAAACNTTCTCAACCCNNAGGNNGTANANCTCCCANNNNTATGGT  
CNTGG
```

Lenti-GFP transfer vector

This vector was a generous gift from Tyler Jacks' lab, and the sequence has been published online at <http://www.addgene.org/20781/>

The lenti-X vector was also obtained from the Jacks lab, although sequencing information for this vector was not readily available